



AFRL-OSR-VA-TR-2015-0159

Control of Boundary Layers for Aero-optical Applications

Stanislav Gordeyev
UNIVERSITY OF NOTRE DAME DU LAC

06/23/2015
Final Report

DISTRIBUTION A: Distribution approved for public release.

Air Force Research Laboratory
AF Office Of Scientific Research (AFOSR)/ RTA
Arlington, Virginia 22203
Air Force Materiel Command

**Characterization, Manipulation and Control of The Turbulent Boundary
Layer For Aero-Optical Applications**

Final Report

**AFOSR Grant FA9550-12-1-0060
Program manager: Dr. Douglas Smith**

Principal Investigator: Stanislav Gordeyev
Department of Aerospace and Mechanical Engineering
University of Notre Dame, IN 46556
(574) 631-4338
E-mail: sgordeye@nd.edu

Co-Principal Investigator: Beverley McKeon
Graduate Aerospace Laboratories
Division of Engineering & Applied Science
California Institute of Technology
Pasadena, California, 91125, USA
(626) 395-4460
E-mail: mckeon@caltech.edu

Period Covered: 15 March 2012 – 14 March 2015

REPORT DOCUMENTATION PAGE					Form Approved OMB No. 0704-0188	
<p>The public reporting burden for this collection of information is estimated to average 1 hour per response, including the time for reviewing instructions, searching existing data sources, gathering and maintaining the data needed, and completing and reviewing the collection of information. Send comments regarding this burden estimate or any other aspect of this collection of information, including suggestions for reducing this burden, to Department of Defense, Washington Headquarters Services, Directorate for Information Operations and Reports (0704-0188), 1215 Jefferson Davis Highway, Suite 1204, Arlington, VA 22202-4302. Respondents should be aware that notwithstanding any other provision of law, no person shall be subject to any penalty for failing to comply with a collection of information if it does not display a currently valid OMB control number. PLEASE DO NOT RETURN YOUR FORM TO THE ABOVE ADDRESS.</p>						
1. REPORT DATE (DD-MM-YY) 12-06-15		2. REPORT TYPE Final		3. DATES COVERED (From - To) 15 March 2012 – 14 March 2015		
4. TITLE AND SUBTITLE Characterization, Manipulation and Control of The Turbulent Boundary Layer For Aero-Optical Applications				5a. CONTRACT NUMBER		
				5b. GRANT NUMBER FA9550-12-1-0060		
				5c. PROGRAM ELEMENT NUMBER		
6. AUTHOR(S) Stanislav Gordeyev (University of Notre Dame) and Beverley McKeon (California Institute of Technology)				5d. PROJECT NUMBER		
				5e. TASK NUMBER		
				5f. WORK UNIT NUMBER		
7. PERFORMING ORGANIZATION NAME(S) AND ADDRESS(ES) Department of Aerospace and Mechanical Engineering University of Notre Dame, Notre Dame, IN 46556				8. PERFORMING ORGANIZATION REPORT NUMBER		
9. SPONSORING/MONITORING AGENCY NAME(S) AND ADDRESS(ES) Air Force Office of Scientific Research 875 N Randolph St, Suite 325, Room 3112 Arlington, VA 22203				10. SPONSORING/MONITORING AGENCY ACRONYM(S) AFOSR		
				11. SPONSORING/MONITORING AGENCY REPORT NUMBER(S)		
12. DISTRIBUTION/AVAILABILITY STATEMENT Approved for public release; distribution unlimited.						
13. SUPPLEMENTARY NOTES Report contains color.						
14. ABSTRACT This report presents results of systematic experimental studies of various passive mitigation techniques to reduce aero-optical effects caused by turbulent boundary layers. Parametric studies of Large-Eddy Break-Up devices showed that aero-optical distortions can be suppressed by 45% for several boundary layer thicknesses. It was shown that moderate cooling of the wall also reduces aero-optical distortions by 60%. A model to predict effects of non-adiabatic walls, both full and partial, over a range of subsonic and supersonic Mach numbers was developed and shown to correctly predict experimentally-observed reductions. Heating the wall allows extending the use of wavefront sensors into low subsonic speeds. Using this technique, aero-optical effects of boundary layers at low (1,700-8,000) Reynolds numbers, were investigated. Simultaneous velocity-optical measurements revealed that large-scale vortical structures are mostly responsible for aero-optical distortions and also indicated that the pressure fluctuations inside these vortical structures might be significant.						
15. SUBJECT TERMS Aero-optics, free-space communication, boundary layer, modeling, control						
16. SECURITY CLASSIFICATION OF:			17. LIMITATION OF ABSTRACT:	18. NUMBER OF PAGES 83	19a. NAME OF RESPONSIBLE PERSON (Monitor) Dr. Douglas R. Smith	
a. REPORT Unclassified	b. ABSTRACT Unclassified	c. THIS PAGE Unclassified			19b. TELEPHONE NUMBER (Include Area Code) (703) 696-6219	

Table of Contents

Section	Page
Table of Contents	iii
Summary	1
1. Aero-Optics of Boundary Layers	3
2. Aero-Optical Mitigation Using Large-Eddy Break Up Devices	6
2.1 Motivation	6
2.2 Experimental Details	7
2.3 Results and Discussion	9
2.3.1 Single LEBU Configuration	9
2.3.2 Streamwise Wavefront Correlations	17
2.3.3 Single LEBU Parametric Study	18
2.3.4 Multiple-Element LEBU Devices	23
2.4 Conclusions and Discussion	30
3. Wall Cooling Effects	33
3.1 Original Aero-Optic Model for Wall Temperature Effects	33
3.2 Updated model for non-adiabatic boundary-layer aero-optical distortions	34
3.2.1 Cooled Wall Results	37
3.2.2 Convective speeds	40
3.3 Extension to supersonic speeds	41
3.4 Results for Partial Wall Cooling	41
3.5 Partial Wall Cooling Model	45
3.6 Conclusions and Discussion	51
4. Aero-Optics of Boundary Layers at Low Reynolds Numbers	55
4.1 Motivation	55
4.2 Results	55
4.3 Conclusions and Discussion	58
5. Simultaneous Optical/Velocity Measurements	60
5.1 Motivation	60
5.2 Approach	60
5.3 Experimental Setup: Caltech	61
5.4 Results: Caltech	62
5.4.1 Statistics	62
5.4.2 Convection Velocities	64
5.4.3 Conditional Averaging	65
5.4.4 Correlation	67
5.5 Discussion	69
5.6 Conclusions: Caltech	70
5.7 Experiments: Notre Dame	70
5.8 Results: Notre Dame	71
5.8.1 Local OPD-minima	71
5.8.2 Local OPD-Maxima	73
5.9 Conclusions: Notre Dame	74
References	75
Appendix: List of Publications Based in Whole or in Part on Results from the Current Program	79

Acknowledgements

This work was supported by AFOSR, Grant FA9550-12-1-0060. The U.S. Government is authorized to reproduce and distribute reprints for government purposes notwithstanding any copyright notation thereon.

Summary

Even in the absence of point-and-tracking turrets, airborne lasers still need to propagate through turbulent boundary layers present on a skin of an aircraft. Previous AFOSR-funded work (Grant FA9550-09-1-0449) performed systematic studies of the optical character of attached turbulent boundary layers. These studies also included non-adiabatic, primarily heated walls.

This prior experimental work exploring the aero-optics of boundary layers has shown strong evidence for the dominance of large-scale turbulent structures as a main source for boundary layer induced aberrations. So, one way to mitigate aero-optical effects is to reduce the size of the large-scale structures. One of the devices successfully used to passively manipulate the large-scale structure is a Large-Eddy Break-Up (LEBU) device. LEBU devices were shown to be effective at reducing streamwise and spanwise integral length scales, boundary layer intermittency, and the strength of bulges and sweeps without introducing a strong shear layer or other optically un-desirable flow features, making them an attractive candidate for use as an aero-optic mitigation application for TBLs. While the potential for using LEBUs for aero-optic mitigation was recognized over three decades ago these suggestions have not been seriously investigated.

Another approach to mitigate aero-optical effects is to reduce the density fluctuations. In the previous work it was also shown that by heating/cooling the wall the density structure can be manipulated without any significant effects on the velocity structure.

In the present work, the effect of two passive boundary layer flow control techniques, LEBU devices and wall heating/cooling, on turbulent boundary-layer-induced aero-optical aberrations is experimentally investigated. Extensive parametric studies are performed investigating the effect of LEBU geometry on levels of optical aberrations in the turbulent boundary layer. The results of these experiments are analyzed to determine the physical mechanisms responsible for the experimentally observed changes. It was demonstrated that long LEBUs, both single and multi-element ones, are effective passive means to reduce aero-optical distortions by as much as 45% immediately downstream of the device, with the effect lasting for several boundary layer thicknesses.

The effect of moderate levels of boundary layer wall cooling, both for full and partial wall cooling, on aero-optic aberrations is also experimentally investigated. The results are favorably compared to a statistical model derived using the temperature-velocity relation from the Extended Strong Reynolds Analogy. For the optimal cooling the aero-optical effects were demonstrated to be reduced by 60%. It was shown that the cooling might be also effective in reducing aero-optical distortions of the boundary layers at supersonic speeds. Comparing the model prediction to the experimental results, it was speculated that while the pressure effects can be neglected in adiabatic boundary layers, they might play an important role in moderately-cooled boundary layers.

As moderate heating simply introduces passive temperature markers in the boundary layer and effectively amplify aero-optical levels, by introducing moderate-temperature mismatch between the wall and the boundary layer, it is possible to thermally tag and measure three-dimensional large-scale structures in incompressible boundary layers. This important result allows using non-intrusive wavefront sensors as alternative complimentary

diagnostic tool and in the present work it was used to study aero-optical properties of turbulent boundary layers with low Reynolds numbers.

Finally, simultaneous velocity/wavefront measurements were performed in both incompressible/heated and compressible boundary layers in order to demonstrate that optical sensors, combined with traditional measurement techniques, can be useful in studying fundamental aspects of physics and dynamics of large-scale structures in boundary layers. Analysis of instantaneous velocity and density fields leads to a better understanding of the connection between aero-optical distortion in turbulent flows and turbulent velocity structure. By comparing the velocity and optical data and using an instantaneous version of Strong Reynolds Analogy, plausible relations between different large-scale structures in the boundary layer and the corresponding wavefronts, as well as the effect of the local pressure field inside the vortical structures, are presented and discussed.

1. Aero-Optics of Boundary Layers

Within the aerospace community, there is substantial interest in developing aircraft-based directed energy systems for a variety of applications, including air-to-air and air-to-ground, line-of-sight optical telecommunications systems. This type of system would use laser beams to relay data directly between optical transmitters and receivers on aircraft, ground stations, and satellites, and would allow for much greater communication bandwidth than is currently available on state-of-the-art aviation communication technologies.

One of the many challenges that must be overcome before line-of-sight optical communications systems can become a robust and reliable method of communication for airborne vehicles is the effect that the Earth's atmosphere has on the propagation of light. This fluid-optic interaction occurs when wavefronts propagating through the Earth's atmosphere encounter regions of air that have non-uniform and/or unsteady distributions of density. Since density and index-of-refraction are proportional to one another, these regions of fluctuating density cause initially planar optical wavefronts passing through them to be distorted (Gladstone & Dale, 1863; Liepmann, 1952; Tatarski, 1961, 1971). These distortions can cause wavefronts to destructively interfere with themselves, leading to significant reductions in the average on-target beam intensity that reduce the overall performance of directed energy systems (Gilbert, 2013; Born & Wolf, 1999; Jumper & Fitzgerald, 2001). Unsteadiness in the density field has also been linked to instantaneous reductions in beam intensity, which can cause disastrous signal drop-outs for free-space communications applications (Gordeyev, Cress, and Jumper, 2013). Wavefront distortions that are the result of density fluctuations found in regions of turbulent flow surrounding aircraft are identified as the aero-optic problem (Gilbert & Otten, 1980; Jumper & Fitzgerald, 2001; Wang, Mani & Gordeyev, 2012).

The levels of optical wavefront distortions can be quantified by the Optical-Path-Difference, $OPD(x, z, t)$, (Wang et al, 2012)

$$OPL(x, y, t) = K_{GD} \int_a^b \rho'(x, y, z, t) dy \quad (1.1)$$

$$OPD(x, y, t) = OPL(x, y, t) - \langle OPL(x, y, t) \rangle$$

where K_{GD} is the Gladstone-Dale constant, the integration is performed along the beam propagation axis, y , and the angled brackets denote spatial averaging. The extent to which wavefronts are distorted from their initially planar state is typically characterized by taking the time-averaged root-mean-square (RMS) of the OPD , or OPD_{rms} .

The performance of free space optical systems can be meaningfully quantified by defining the Strehl ratio, $SR = I/I_0$, where I is the on-target beam intensity in the far field, and I_0 is the diffraction-limited performance in the far field. In the presence of optical distortions $SR < 1$, and, for small levels of OPD_{rms} for a given laser wavelength, λ , can be estimated as,

$$SR = \exp \left[- \left(\frac{2\pi OPD_{rms}}{\lambda} \right)^2 \right],$$

so-called Large-Aperture Approximation (Ross, 2009; Porter, et al. 2013)

Sutton (1969) introduced the most widely cited theoretical formulation for calculating the effect of turbulent boundary layers on optical wavefronts from turbulence statistics. The equation derived by Sutton, referred to as the aero-optic 'linking equation,' was based heavily on Tatarski's (1961) work describing the distortions of electromagnetic waves propagated through

the Earth's atmosphere. It related the time-averaged levels of OPD_{rms} to turbulence density statistics. A simplified version of the linking equation is

$$OPD_{rms}^2 = 2K_{GD}^2 \int \rho_{rms}^2(y) \Lambda_\rho(y) dy, \quad (1.2)$$

where ρ_{rms}^2 is the variance of the density fluctuations, and Λ_ρ is the local density correlation length. The linking equation (1.2) has been validated both experimentally (Hugo & Jumper, 2000; Gordeyev et al, 2014) and numerically (Wang & Wang, 2013; Wang & Wang, 2013) and establishes a relation between the level of aero-optical distortions and properties of the density structure, ρ_{rms} and Λ_ρ . So, aero-optical data can provide important information about the density fields in turbulent flows.

In order to achieve a large field of regard, airborne directed energy systems have gravitated towards the use of hemisphere or hemisphere-on-cylinder turrets in order to send and receive laser beams. While these devices are mechanically simple, the complex three-dimensional flow that develops around turrets includes elements of turbulent boundary layers, flow separation, shear layers, wakes, and unsteady shocks (Gordeyev & Jumper, 2010).

For applications in which a large field of regard is not an essential requirement, the flow-field over the optical aperture can be vastly simplified by eliminating the turret completely. Instead, the beam could be propagated through an aperture or phased array that is flush-mounted to the skin of the aircraft (Serati & Stockley, 2003; Whiteley & Gordeyev, 2013). In this configuration, the only aero-optically active flow field that must be traversed by the beam is the compressible, turbulent boundary layer (TBL). At present, aero-optic aberrations caused by the boundary layer have been studied analytically, experimentally and computationally for over six decades (Gordeyev et al. 2014 and references therein), and much has been learned about the physics of TBL fluid-optic interactions. Important findings from research on the aero-optical characteristics of TBLs can be summarized via a few main conclusions. First, aero-optic aberrations have been strongly correlated with the large-scale turbulent motions convecting in the outer part of the TBL (Gordeyev et al. 2014, and the references therein). Secondly, analysis of time-resolved TBL wavefront measurements has revealed that even in cases where on-average target intensity is found to be high, large intermittent drop-outs in far-field signal intensity that lasted on the order of one millisecond were found (Gordeyev, Cress & Jumper, 2013), which would be crippling to the performance of any potential airborne laser-based high-bandwidth free-space communications systems.

These results clearly demonstrated that although the TBL is vastly simpler than the flow environment around a turret body, boundary layers are not guaranteed to be entirely benign with respect to aero-optics. As a result, there is substantial interest in developing and testing flow control schemes that would modify the boundary layer flow in such a way that would permit airborne directed energy and free-space communications systems to achieve high on-target intensity in both a time-averaged and instantaneous sense.

The linking equation (1.2) implies that in order to reduce overall aero-optical distortions of a boundary layer, we should investigate flow-control approaches that:

1. Reduce density fluctuations inside the boundary layer, primarily in its outer region,
2. Reduce the size of aero-optical structure,
3. Reduce the integration region.

Jumper (1980) first suggested the use of parallel plate manipulators for aero-optic flow control. These devices, which are also commonly referred to as Large-Eddy Break-Up (LEBU) devices, were originally proposed as a method of flow control for achieving viscous drag reduction (Corke, et al. 1979). LEBUs were found to achieve this end by altering the turbulence structure in the outer part of the TBL, and they significantly reduced integral length scales for long distances downstream of the devices (Corke, 1981; Savill & Mumford, 1988; Anders, 1990, and others). These effects, especially the suppression of large-scale turbulent structures in the outer part of the boundary layer, are very much aligned with the mechanisms identified as the dominant source of TBL aero-optic aberrations. Prior to this work however, no experimental or computational evaluation of LEBUs for aero-optic mitigation has been performed. Chapter 2 of this report will cover main results of this study.

In fact, very few studies of flow control methods for mitigating TBL aero-optics have been performed to date (Cress, 2010; White & Visbal, 2011). One illuminating investigation was performed by Cress (2010) under AFORS-funded Grant FA9550-09-1-0449, in which the effect of wall-temperature on TBL wavefront aberrations was experimentally investigated. Experiments were particularly focused on wall-heating, but both preliminary experimental measurements and a simplified theoretical model for wall temperature effects indicated that wavefront aberrations could be reduced by as much as 80 % through the use of wall cooling (Cress, 2010). Additional data are still required, however, to validate and improve Cress' model over a wide range of temperatures and Mach numbers, but these findings already suggested that wall cooling is also a promising technique for aero-optic mitigation. Extensive work, including a development of the theoretical model extended to supersonic regime was done during this grant and overview of major results is presented in Chapter 3.

Also, there is a pressing need to develop techniques to 'close the gap' in Reynolds number between experiments and computations of the aero-optic effects of TBLs. Due to both computational constraints and wavefront sensor limitations, experimental measurements of TBL aero-optic effects are performed at Reynolds numbers that are about an order of magnitude higher than results from high-fidelity simulations, making one-to-one validation of the computational methods used difficult to date. Wall heating experiments, presented in details in Chapter 4, showed that it is possible to passively amplify TBL wavefront aberrations, thus raising the possibility of using wall heating as a means of increasing the signal-to-noise ratio in low-speed experiments where aero-optic aberrations are otherwise very weak.

Finally, non-intrusive feature of optical measurements, as well as sensitivity to density field only, makes them very attractive complimentary diagnostic tools. When combined with traditional measurement techniques like hot-wires, PIV, pressure sensors etc, they provide valuable additional information about physical mechanisms inside the boundary layers. To demonstrate that, simultaneous velocity/optical measurements were performed in both low subsonic and transonic boundary layers. By analyzing corresponding velocity and density fields and assuming different relations between these quantities, a better understanding of the physics and dynamics of the large-scale vortical structures and their role in aero-optical distortions can be obtained. In particular, preliminary results indicate that the pressure field might not be negligible inside these structures. A summary of these results are provided and discussed in Chapter 5.

2. Aero-Optical Mitigation Using Large-Eddy Break Up Devices

2.1 Motivation

A great deal of effort in the field of fluid mechanics has been dedicated to identifying and evaluating different methods of passive flow control for turbulent boundary layers, including riblets (Walsh 1990), vortex generators (Zaman, Hirt, & Bencic, 2012), honeycombs and screens (Yajnik & Ancharya, 1977), and large-eddy break-up (LEBU) devices (Corke, Guezennec, & Nagib, 1979). Studies of LEBU devices for reducing viscous drag in turbulent boundary layers has confirmed that C_f could be reduced for distances $\sim O(100\delta)$ downstream (Corke, 1981; Anders, 1990) by substantially altering the turbulence structure in the outer part of the boundary layer (Anders, 1990). The effectiveness of the LEBU device for modifying large-scale turbulent structures in the outer part of the TBL has caused it to be identified as a potential method of passive flow control that could be used to achieve aero-optic mitigation in the TBL (Jumper, 1980; Anders, 1985).

In general, LEBU devices consist of one or more thin flat plates or airfoils placed parallel to the wall within the turbulent boundary layer, as shown in Figure 2.1. These devices were designed to act as screens with sparse elements, significantly reducing blockage effects while retaining the ability to directly manipulate turbulent structures in the outer part of the boundary layer (Corke, 1981). The significant reduction in blockage compared to screen-type devices was expected to result in a net viscous drag reduction compared to the un-manipulated TBL (Corke, Guezennec, & Nagib, 1979). Some experiments have investigated LEBU devices with as many as four flat plate elements (Corke, 1981), however this work is limited to investigating LEBU devices with at most two flat plates.

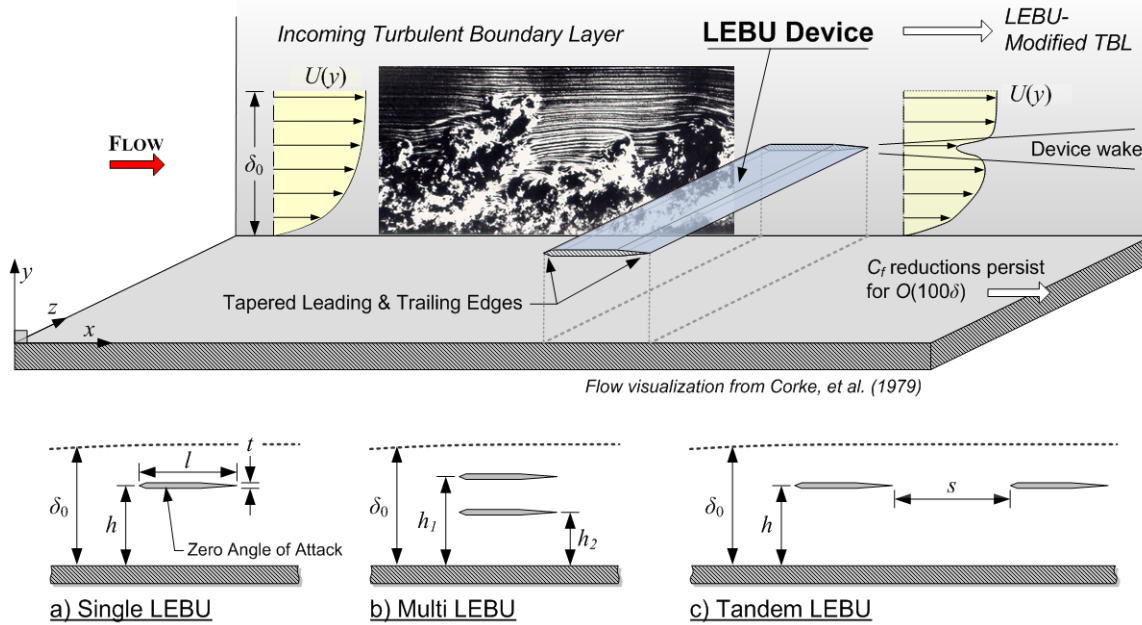


Figure 2.1. Top: Schematic of the effect of a single LEBU device on the TBL. Bottom: schematics of the a) Single LEBU, b) Multi-LEBU, and c) Tandem-LEBU configurations. [flow visualization image from Corke, et al. (1979)].

Single LEBU devices, shown in Figure 2.1a, consist of a single thin plates or airfoils of thickness t and length l arranged parallel to the wall (i.e. at zero angle of attack), offset by some height $h \leq \delta_0$. LEBU configurations with more than one parallel plate, sometimes referred to as multiple element LEBUs, are shown in Figure 2.1b and Figure 2.1c. Arrangements of vertically stacked parallel plates of identical length and thickness, later referred to as Multi LEBU devices, are shown in Figure 2.1b, along with the notation used to identify the height of each plate. For multi-LEBU devices, the heights of each plate, starting with the outermost and proceeding towards the wall, are denoted as h_1 , and h_2 . LEBU plates arranged in series in the streamwise direction are later referred to as Tandem LEBU devices, as shown in Figure 2.1c. Each individual plate is identical in length l , and is mounted at the same height off the wall h , but plates are separated by some gap distance s in the streamwise direction.

Effect of LEBU Devices on TBL Characteristics

The characteristics of LEBU modified boundary layers have been well documented using an array of diagnostic methods in order to quantify and maximize viscous drag reductions, and to investigate the mechanisms that were responsible for LEBU effects (Anders, 1990, and the references therein). Smoke-wire flow visualization records (Corke, 1981; Savill & Mumford, 1988) showed a significant change in turbulence structure in the outer part of the LEBU modified TBL. In particular, the flow visualization images indicate that the size of turbulent structures in the outer layer are substantially reduced (inspiring the LEBU moniker), and showed an obvious reduction in intermittency in the TBL edge, which would reduce the entrainment of irrotational, high momentum freestream fluid (Corke, 1981).

Potential for Aero-Optic Mitigation

Prior experimental work exploring the aero-optics of boundary layers has shown strong evidence for the dominance of large-scale (i.e. outer-region) turbulent structures as a source for boundary layer induced aberrations. It is also suspected that large instantaneous drop-outs in far-field beam intensity caused by TBLs are related to large-scale motions (LSMs) in the outer part of the TBL (Gordeyev, Cress, & Jumper, 2013) such as turbulent bulges and hairpin vortex (Cress, 2010). Conveniently, LEBU devices are effective at reducing streamwise and spanwise integral length scales, boundary layer intermittency, and the strength of bulges and sweeps without introducing a strong shear layer or other optically un-desirable flow features, making them an attractive candidate for use as an aero-optic mitigation application for TBLs.

While the potential for using LEBUs for aero-optic mitigation was recognized over three decades ago by Jumper (1980), and again several years later by Anders (1985), these suggestions have not been seriously investigated. It is important to recall that prior studies of mechanisms and optimization of LEBU devices have been focused on reducing skin friction, which is related to the condition of the TBL locally near the wall. Also, the condition of having a small amount of LEBU device drag, which was an important factor for LEBUs drag reduction optimization, is not necessarily a restrictive factor for aero-optic mitigation. In real directed energy applications, it may be desirable to accept a small additional localized drag penalty in exchange for improved aero-optic performance over a finite aperture.

2.2 Experimental Details

Experimental results presented in this report were performed in the Transonic Wind Tunnel (TWT) facility located in Hessert Laboratory for Aerospace Research at the University of

Notre Dame. The TWT is composed of an inlet contraction, with an area ratio of 150:1 and screens and honeycombs to reduce freestream turbulence intensities (measured w/ hot-wires to be on the order of 2%). Following the inlet contraction is a modular smooth wall boundary layer development section $10.0 \text{ cm} \times 9.9 \text{ cm}$ (or about $4'' \times 4''$), an optical measurement section, and a diffuser section that leads to the vacuum pump plenum.

In the present study, the boundary layer development length to the optical measurement location varied between 100 cm and 170 cm. In the optical measurement section, the upper and lower Plexiglas walls were replaced with optical quality glass in order to ensure good optical access for aero-optic wavefront measurements. Freestream Mach number spanned the range from approximately 0.2 to 0.5. The boundary layer thickness, δ , was found to be 1.9 cm, and the integral displacement and momentum thicknesses were 2.6 mm and 1.9 mm, respectively. At 170 cm, δ was found to be approximately 2.4 cm, δ^* was 3.6 mm, and the momentum thickness Θ was 2.75 mm. The shape factors for both of these cases ranged from $H = 1.31 - 1.33$, which is consistent with other TBLs at these Reynolds numbers (Nagib, et al. 2007).

The two-beam Malley probe used in this work used a 20 to 30 mW continuous wave (CW) HeNe ($\lambda = 633 \text{ nm}$) laser source that was spatially filtered to generate a collimated small diameter beam with high, near uniform intensity across the beam profile. The spatial filter was also used to control the diameter of the source beam, which was approximately 1 mm. The source beam was then split into two parallel beams of equal intensity using a 50/50 beam splitter plate and a steering mirror. The spacing between these beams, Δ , is typically on the order of 5 – 10 mm. This pair of parallel beams then passes straight through a beam cube (losing 50% of its intensity) and through the measurement region (typically a wind tunnel test section) to the return mirror. The return mirror is aligned so that the Malley beams are reflected back to the beam cube along the same path. If the deflection angles are small (which they are for aero-optic measurements) then this is effectively an analog doubling of the signal intensity for the Malley probe.

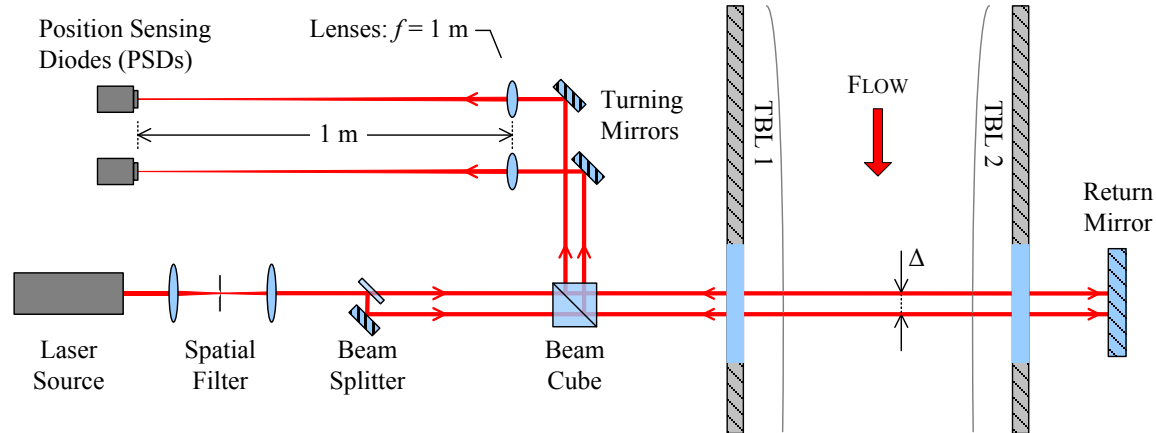


Figure 2.2: Schematic of a typical two-beam Malley probe sensor in a double-pass, double boundary layer (DBL) wavefront measurement configuration.

The beam cube reflects the return beams onto a configuration of turning mirrors that isolate each of the two parallel Malley beams. Each beam is then passed through a final focusing lens, which in this case has a focal length of 1 m, onto an analog position sensing device (PSD) placed in the focal plane of the final focusing lens. The PSD measures the displacement of the beam spot location on its surface. Since the PSD is located one focal length away from the final

focusing lens, a ray incident on the lens that is deflected at some angle θ will can be calculated from the beam displacement on the PSD.

2.3 Results and Discussion

Three different LEBU geometries were tested: a single LEBU, Figure 2.1a) and multiple element LEBU devices called Multi LEBU, Figure 2.1b) and Tandem LEBU, Figure 2.1c). All relevant LEBU parameters are also defined in Figure 2.1. One goal of this investigation is to verify that the LEBUs used in this work modify the velocity field in a manner that is consistent with the results of prior studies. The present work also study seeks to study the relationship between the characteristics of the LEBU-modified TBLs and their corresponding effect on wavefront statistics. It also presents the results of parametric studies of single and multiple element LEBU devices in order to determine the optimal LEBU configuration for aero-optic mitigation.

2.3.1 Single LEBU Configuration

A full record of the LEBU configurations that were investigated in this work is presented in Table 2.1. During all experimental measurements, free-stream velocity was held constant for all tests at approximately $M = 0.4$.

Table 2.1. Single LEBU Device Configurations

Length, l/δ		0.8	1.0	1.6	4.0
Height h/δ	0.3	◆	◆	◆	◆
	0.5	◆	◆	◆	◆
	0.6	◆	◆	❖	◆
	0.8	◆	◆	◆	◆
Legend					
◆		Malley probe wavefront measurements single modified TBL			
❖		Single and double modified TBL cases for wavefront measurements			

Velocity Measurements

To investigate the effect of the devices on the turbulent boundary layer, hot-wire velocity measurements were obtained at three streamwise locations ($x/\delta = 1.5, 3.5$ and 5.4) downstream of the single LEBU devices using the hot-wire anemometer. From these data, mean and fluctuating velocity profiles were computed, along with power spectral densities of fluctuating velocity, and compared to results of the baseline TBL in order to evaluate the effect of LEBU devices on the boundary layer. These data were also compared to prior LEBU studies in order to confirm that the LEBU devices used in this experiment behave similarly to what previous authors have reported.

Mean velocity profiles are plotted in Figure 2.3 for hot-wire velocity measurements obtained at three streamwise locations ($x/\delta = 1.5, 3.5$, and 5.4) downstream of the LEBU trailing edge for of the $l = 1.6\delta$, $h = 0.6\delta$ LEBU device. The wall-normal coordinate y is normalized by the incoming TBL thickness measured at the LEBU location, $\delta_0 = 2.4$ cm. The velocity profile for the un-perturbed boundary layer is plotted for reference, and a horizontal dashed line marks the LEBU height. Downstream of the LEBU devices, a well-defined wake deficit is observed imprinted on the TBL mean velocity profiles; this wake region is centered about the LEBU height, and as x/δ increases the maximum velocity deficit decreases and the wake spreads in the

spanwise direction. Outside of the LEBU wake region, there is no significant change observed in the mean velocity profile.

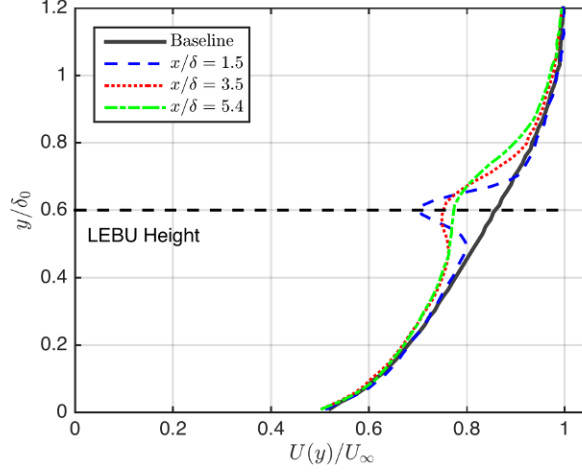


Figure 2.3. Mean velocity profiles of the LEBU-modified TBL at several locations downstream of a Single LEBU, $l = 1.6\delta$, $h = 0.6\delta$.

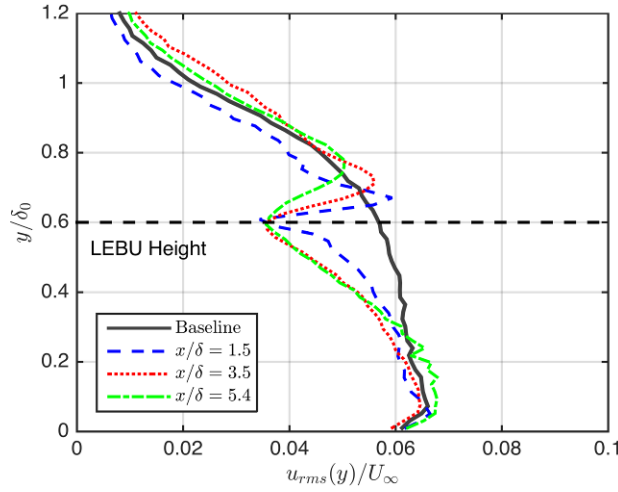


Figure 2.4. Root-mean-square velocity profiles of the LEBU-modified TBL at several locations downstream of a Single LEBU, $l = 1.6\delta$, $h = 0.6\delta$.

Profiles of the root-mean-square of the fluctuating velocity component for the same LEBU device, which are plotted in Figure 2.4 along with the baseline case, showed a significant reduction in u_{rms} in the LEBU modified boundary layer, with the maximum reduction being located at the LEBU height. Unlike the mean velocity profiles, the magnitude of the reduction did not change significantly with increasing x , but rather remained constant around $u_{rms} \approx 0.04U_\infty$. Velocity fluctuations in the region of the boundary layer below the LEBU height also showed a reduction in magnitude with respect to the baseline, with the reductions extending further towards the wall with increased distance downstream of the LEBU trailing edge. Above the LEBU device, small peaks were found in the u_{rms} profiles at all streamwise locations that exceeded the baseline u_{rms} locally. The magnitude of these spikes in RMS decreased further downstream from the LEBU and the peak location migrated away from the wall slightly.

Upon inspection, it was found that these velocity data are consistent with typical mean velocity profiles obtained in previous studies (Corke, et al., 1979; Hefner, et al., 1979; Lemay, et al., 1990), which showed a similar velocity deficit in the region just downstream of LEBU devices.

Wake-Deficit Velocity Profiles

In the mean velocity profiles shown, the maximum velocity deficit in the wake region is shown to diminish as downstream distance increases, indicating that the modified boundary layer is recovering from the disturbance caused by the LEBU device, at least in the mean velocity profiles. The spanwise extent of the wake imprint spreads in the wall-normal direction with increasing distance downstream. Both of these characteristics are consistent with the behavior of planar self-similar wakes in constant mean flow like those investigated by Moser, et al. (1998). They found that for planar wakes, the wake velocity deficit, U_0 , and the wake half-width, b , evolved in the streamwise direction as $b \sim x^{1/2}$ and $U_0 \sim x^{-1/2}$. The non-dimensional growth rate of the wake, defined as $\alpha = \Theta^{-1} d(b^2)/dx$, where Θ is the wake momentum thickness, was found to be 0.29 – 0.41 for canonical self-similar plane wakes.

To determine if the LEBU wake evolves in a self-similar manner within the TBL, a modified form of the wake deficit velocity profile, $U_{Deficit}(y)$, is computed by subtracting the LEBU-modified boundary layer profiles from the baseline velocity profiles (Moser, et al., 1998):

$$U_{Deficit}(y) = U_{LEBU}(y) - U_{Baseline}(y) \quad (2.1)$$

The maximum wake deficit velocity, U_0 , is the maximum of the absolute value of the wake deficit profile, $U_0 = \max[|U_{Deficit}(y)|]$. Note that where the baseline velocity is greater than the mean velocity of the LEBU profile, $U_{Deficit}$ will be negative. The wake half-width, b , is defined as the distance between the two points where $-U_{Deficit}(y) = 0.5U_0$ (Moser, et al., 1998).

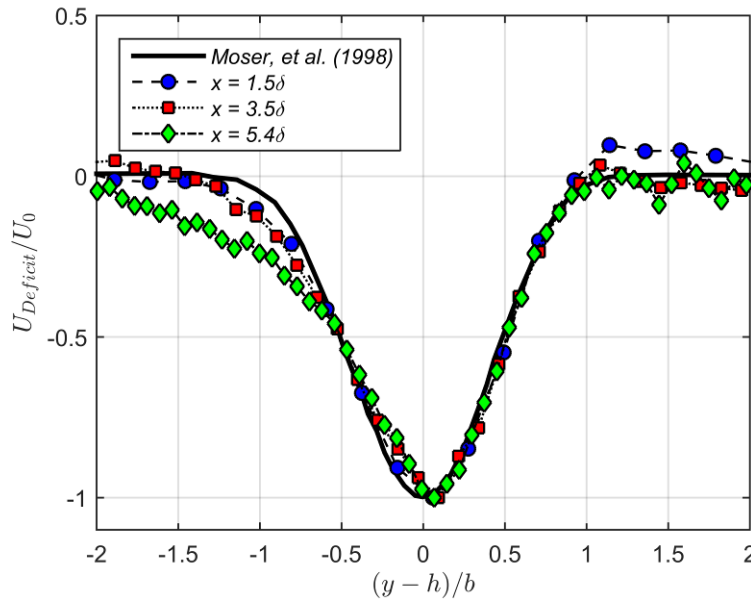


Figure 2.5. Mean wake velocity deficit profiles downstream of the $l = 1.6\delta$, $h = 0.6\delta$ single LEBU device.

Mean velocity deficit profiles for the LEBU modified boundary layer data were computed, and the results are shown in Figure 2.5 for the $l = 1.6\delta$, $h = 0.6\delta$ LEBU device, along with the mean deficit profile from Moser, et al. (1998) for canonical plane wakes. The LEBU wake deficit profiles presented exhibit self-similarity that is consistent with canonical plane wake data on the outer part of the boundary layer (i.e. $(y - h)/b > 0$) for all streamwise locations. For the inner part of the wake (i.e. $(y - h)/b < 0$), the wake profiles deviate slightly from the self-similarity scaling, with the deviation becoming larger for locations further downstream. From these data, the non-dimensional growth rate was found to be approximately 0.15 for the LEBU modified TBL wake profiles. This was much less than the range of growth rates, 0.29 – 0.41, found for canonical self-similar plane wakes (Moser et al, 1998).

The deficit profile for the RMS velocity fluctuations can be computed in a similar fashion to the mean velocity in equation (2.1):

$$u_{rms, Deficit}^2(y) = u_{rms, LEBU}^2(y) - u_{rms, Baseline}^2(y) \quad (2.2)$$

RMS velocity deficit profiles computed via equation (2.2), however, were not found to scale well with self-similar planar wake data, due to the large reductions in u_{rms} below the LEBU device. The location of the ‘spike’ in u_{rms} that occurs on the upper side of the LEBU in Figure 2.4 is found to be constant at about $(y-h)/\delta \approx 0.6$. This is an indication that the local increase in u_{rms} above the LEBU is closely related to the wake deficit profile in the modified TBL.

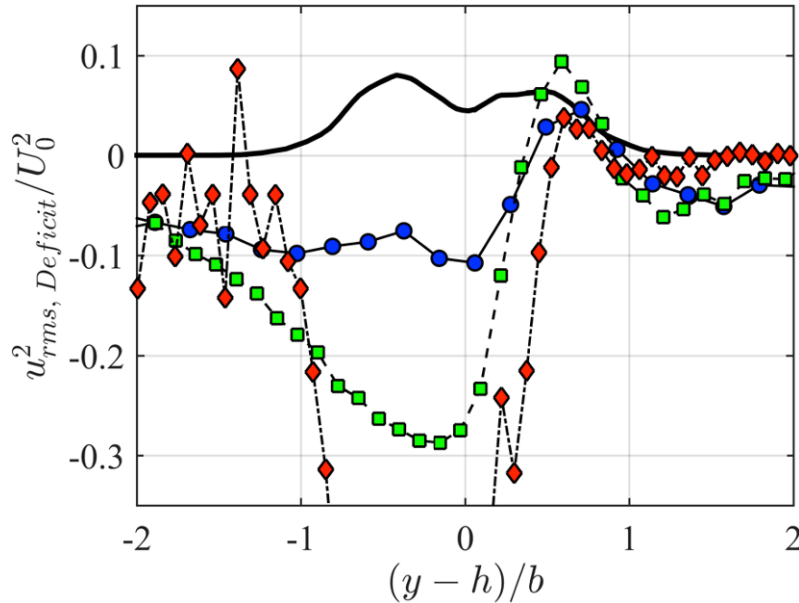


Figure 2.6. Wake root-mean-square velocity profiles downstream of the $l = 1.6\delta$, $h = 0.6\delta$ single LEBU device. Legend is the same as Figure 2.5.

Corke (1981) recognized that local changes in the mean velocity profile could have a significant impact on velocity fluctuations in the LEBU-modified boundary layer, since the dominant turbulence production term, $\overline{u'v'}(dU/dy)$, is directly proportional to the local mean velocity gradient. Since the wake deficit mean profile induced on the LEBU within a sheared mean flow, the local velocity gradient below the LEBU device is decreased and the velocity gradient above the LEBU is increased. This is illustrated in Figure 2.7, where dU/dy and the

fluctuating velocity component in the LEBU-modified boundary layer are plotted for easy comparison. Here, dU/dy was computed from experimental data using a first order central difference method. It is evident from Figure 2.7 that there is some correlation between the velocity gradient and u_{rms} , especially in the neighborhood of the LEBU height, however changes in dU/dy for the LEBU-modified boundary layer does not fully account for reductions in velocity fluctuations below the LEBU device. Rather it is likely that both the changes in velocity gradient *and* the limitation of vertical velocity fluctuations (i.e. the plate effect), that suppressed u_{rms} over such a wide range of the area below the LEBU device. Additional support for this notion was shown in Lemay, et al. (1990), where measurements showed suppressed production for $y < h$ in the LEBU-modified boundary layer up through the location where the mean profile (and therefore the velocity gradient) is *nearly* recovered to baseline state.

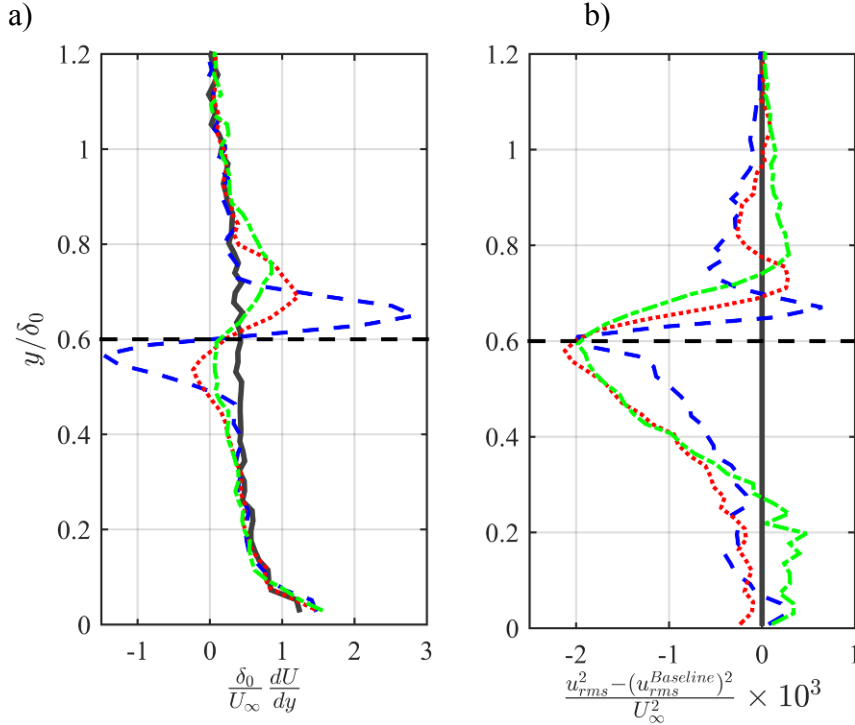


Figure 2.7. a) Normalized mean velocity gradient and b) baseline-normalized u_{rms} profiles for LEBU modified boundary layer ($l/\delta = 1.6$, $h/\delta = 0.6$). Legend is the same as Figure 2.4.

Deflection Angle Spectra

Amplitude spectra of Malley probe deflection angle measurements were computed for measurements downstream of the single LEBU devices at a number of locations up to 10δ downstream of the device trailing edge. The results are presented for several streamwise locations in Figure 2.8 where frequency is non-dimensionalized as Strouhal number based on freestream velocity, V_∞ , and the canonical TBL thickness at the LEBU mounting location, δ . Note that for $St_\delta < 0.2$, deflection angle spectra are contaminated by mechanical vibration from the wind tunnel motors. Also, in the high frequency range of the spectra the sharp peaks near $St_\delta = 6, 7$, and 10 were found to be the result of electronic interference from sources within the laboratory environment.

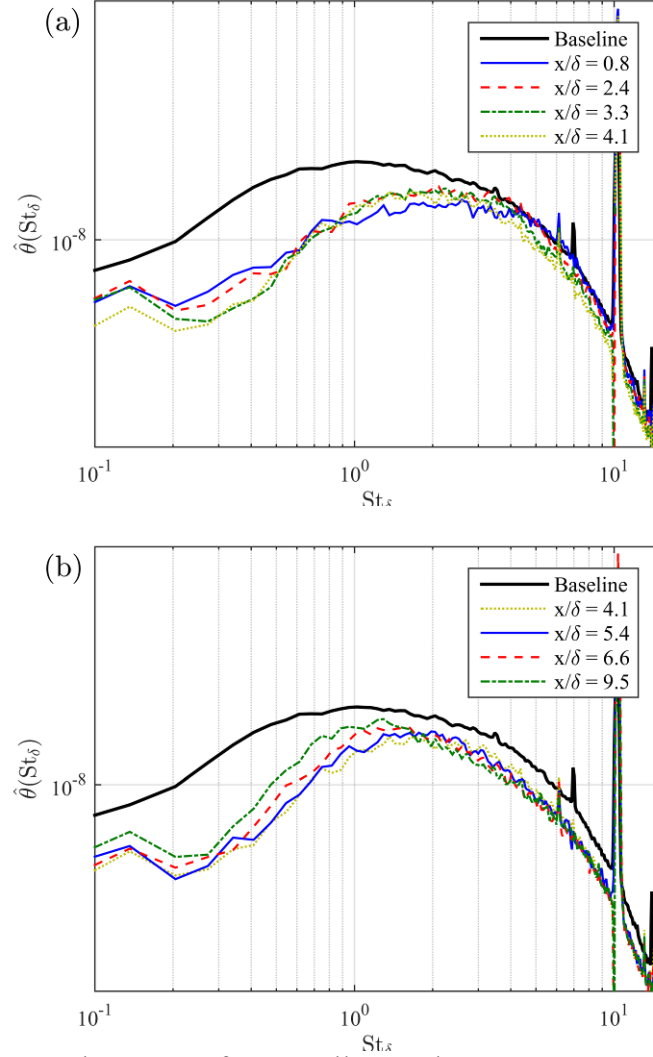


Figure 2.8. Deflection angle spectra from Malley probe measurements of the modified TBL for the $l = 1.6\delta$, $h = 0.6\delta$ single LEBU device at streamwise locations a) from $x = 0.8\delta$ to $x = 4.1\delta$ and b) from $x = 4.1\delta$ to $x = 9.5\delta$.

Figure 2.8 presents deflection angle spectra obtained from Malley probe measurements downstream of the $l = 1.6\delta$, $h = 0.6\delta$ single LEBU device at several streamwise locations. Just downstream of the device ($x \sim 1\delta$), the spectra presented in Figure 2.8a showed significant reductions over the range of low frequencies, $0.2 < St_\delta < 4$. Spectra at streamwise locations $x < 4\delta$ did not show any significant increase over the baseline deflection angle spectrum; by $x = 2.4\delta$ the peak of the LEBU-modified TBL spectrum, which is around $St_\delta = 2$, increased slightly. The peak amplitude then remained relatively constant through approximately $x = 4\delta$. Portions of the high-frequency range of the spectra ($St_\delta > 4$) and the low-frequency end of the spectra ($St_\delta < 0.5$) were found to decrease with increasing x between $3 - 4\delta$ downstream. Overall, for this LEBU configuration, the reductions in the deflection angle spectra were found to be the largest compared to other tested single LEBU devices.

Deflection angle spectra collected further downstream between $x/\delta = 4 - 10$ for the $h = 0.6\delta$ single LEBU are shown in Figure 2.8b. In general, spectra from these distances downstream

of the LEBU trailing edge were found to result in broadband reductions that were notably larger than what was found for other single LEBU devices. The peak amplitude of the deflection angle was shown to be increasing for measurements further downstream of the LEBU, and the peak location was found to be shifting slightly back towards $St_\delta = 1$, the peak location for the unperturbed TBL wavefront spectra. As x/δ approached 10, there were notable increases in the low-frequency range of the spectra that were caused by the shift in peak frequency and increase in peak amplitude of the LEBU-modified TBL.

In summary, inspection of deflection angle spectra for the single LEBUs presented in Figure 2.8 and other tested ones demonstrated that the devices yielded *immediate and significant reductions* in the low-frequency range of the spectra. Note that assuming frozen flow (which has been shown to be a good assumption for Malley probe wavefront measurements in the TBL), the range of frequencies over which reductions were observed corresponds to turbulent structures that are up to 5δ in length. For Malley probe spectra for the LEBU modified TBLs, the peak location was found to initially shift to higher Strouhal numbers (~ 2), indicating that the characteristic length scales in the modified TBL are reduced via the LEBU devices and their effect on large-scale motions.

The behavior of the high-frequency portion of the deflection angle spectra gave some evidence that the energy formerly contained in the large scale turbulent structures was redistributed by the LEBU wake into smaller scale turbulent structures. The turbulent kinetic energy (TKE) contained in these small scale structures was quickly dissipated through the energy cascade. After the excess TKE is shed through the mechanism of dissipation, the high-frequency range of spectra is also reduced. These observations are consistent with measurements of the TKE balance in a LEBU modified TBL performed by Lemay, et al. (1990), which showed both a significant increase in the production term and an increase in the dissipation term in the LEBU wake in the neighborhood of the $y = h$ just downstream of the LEBU device (approx. $x/\delta \approx 2.5$). Within 10δ downstream of the LEBU trailing edge, however, Lemay, et al. (1990) found that the dissipation term is nearly recovered to the baseline canonical TBL levels. This is consistent with the downstream distances found in the present study at which wavefront spectra were found to show reductions in the high-frequency end of the spectra.

To better visualize the evolution of deflection angle spectrum in the streamwise position as compared to the baseline deflection angle spectrum, the ratio of deflection angle spectrum for LEBU-modified TBLs to baseline TBL spectrum can be defined as

$$C_\theta(x/\delta, St_\delta) = \frac{|\hat{\theta}_{\text{LEBU}}(x/\delta, St_\delta)|}{|\hat{\theta}_{\text{Baseline}}(x/\delta, St_\delta)|} - 1 \quad (2.3)$$

where $C_\theta(x/\delta, St_\delta)$ will be equal to zero where the LEBU-modified spectrum is equal to the baseline spectrum, positive where the LEBU-modified spectrum is increased compared to the baseline, and negative where the LEBU-modified spectrum is less than the baseline spectrum. Contour plots of $C_\theta(x/\delta, St_\delta)$ are presented in Figure 2.9 for both single LEBU devices. For both cases, Figure 2.9 shows a significant reduction in large-scale structures below $St_\delta = 3$ that diminishes as distance from the LEBU trailing edge increases. Additionally, a decrease in high-frequency content of the deflection angle spectrum is also shown as the downstream distance increases, which is consistent with the results previously shown in Figure 2.8.

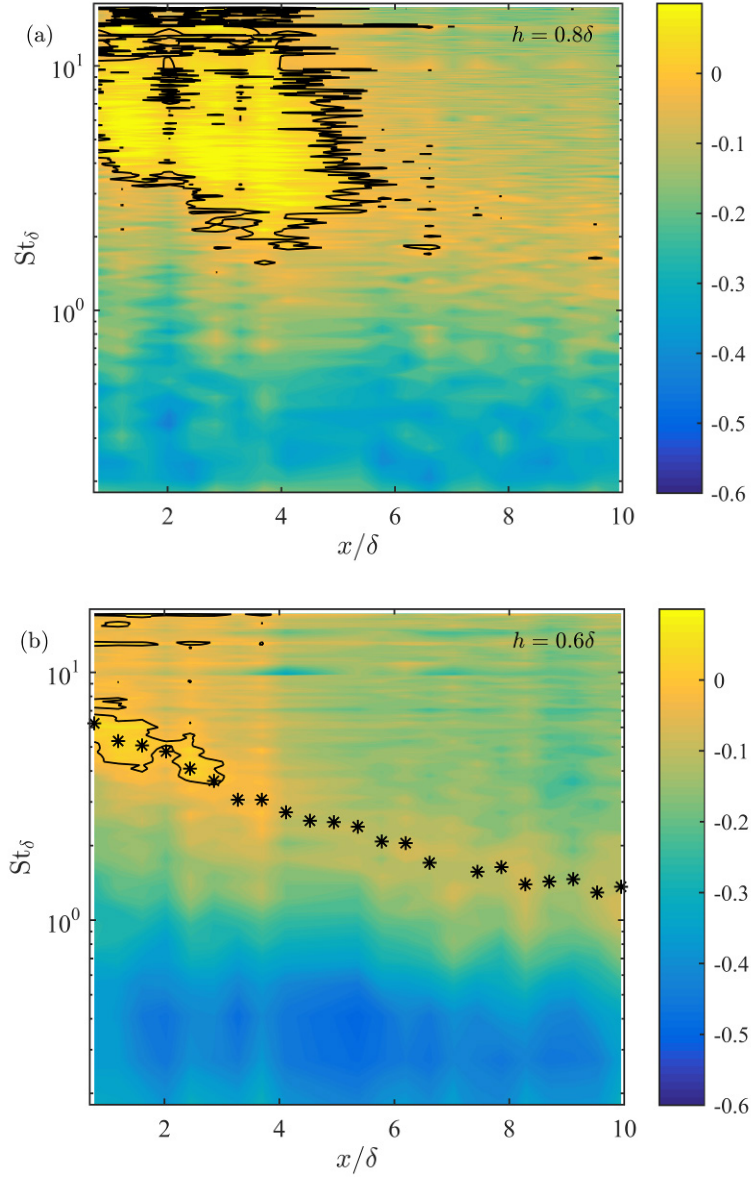


Figure 2.9. Baseline-normalized spectrum surfaces $C_\theta(x/\delta, St_\delta)$ for single LEBU devices of height a) $h/\delta = 0.8$ and b) $h/\delta = 0.6$. Note that * denotes the peak location of C_θ at each value of x .

One feature that is readily apparent in the LEBU-modified deflection angle spectrum plotted in Figure 2.9 is the evolution of the peak of $C_\theta(x/\delta, St_\delta)$ with the downstream distance from the LEBU device, which likely corresponds to the development of the LEBU device wake. The shift of the peak in C_θ to the lower frequencies occurs as the downstream distance increases, eventually approaching a value of $St_\delta = 1$. Several authors (Corke, 1981; Lemay, et al. 1990, and others) found that just downstream of the LEBU there is a momentum-deficit wake that begins at the LEBU trailing edge, and grows with the increasing downstream distance, x , to a point where it is on the order of the TBL thickness δ and interacts with the near-wall layer. If it is assumed that the peak in C_θ corresponds to a coherent structure of some size, γ , then the relationship between

the structure size γ and the frequency f_{Peak} at which the maximum in C_θ occurs can be expressed via the frozen flow assumption,

$$\gamma \cong \frac{U_\infty}{f_{Peak}} = \frac{\delta}{St_\delta^{Peak}}, \quad (2.4)$$

where St_δ^{Peak} is the Strouhal number that corresponds to f_{Peak} . If it is assumed that the shift of St_δ^{Peak} toward lower frequencies corresponds to the growth in the size of the LEBU wake, then the half-width, b , of the LEBU wake can be estimated as a function of x from the peak of the normalized spectrum;

$$b(x) \cong \frac{\gamma}{2} = \frac{1}{2} \frac{\delta}{St_\delta^{Peak}}. \quad (2.5)$$

The result of this estimation for the single LEBU, $h = 0.6\delta$ device is presented in Figure 2.10 along with measurements of the wake half-width computed from hot-wire velocity profiles. The comparison shows that the estimate of the wake half-width, b , from the normalized spectrum peaks is in good agreement with direct measurements obtained previously for the same case, and verifies that the evolution of the peak of the normalized spectrum C_θ is a result of the growth of the LEBU wake within the modified TBL.

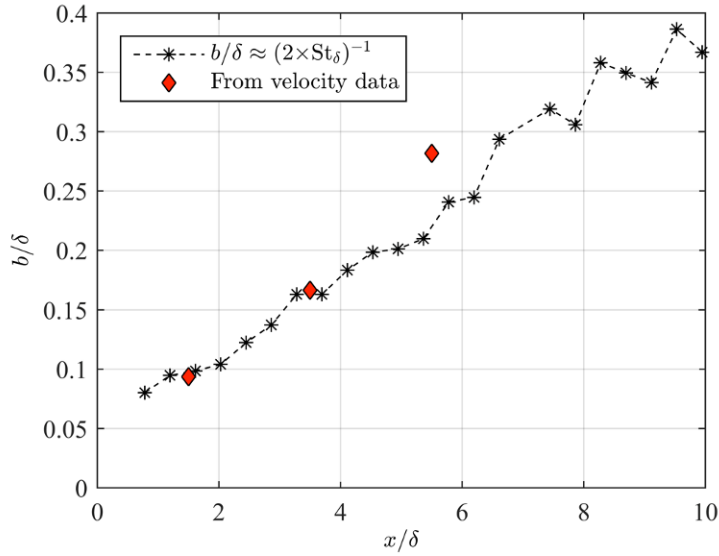


Figure 2.10. Comparison of wake half-width b estimated from $C_\theta(x/\delta, St_\delta)$ and from hot-wire velocity measurements downstream of the $l = 1.6\delta$, $h = 0.6\delta$ from section 6.2.1.

2.3.2 Streamwise Wavefront Correlations

The streamwise wavefront correlation functions of Malley probe wavefront data were computed by taking the inverse Fourier transform (F^{-1}) of the single-boundary layer wavefront frequency spectra to obtain the autocorrelation in time at each streamwise measurement location:

$$R_W(\tau) = F^{-1} \left\{ |\hat{W}(f)|^2 \right\}. \quad (2.6)$$

The frozen-flow approximation, $\Delta x = U_C \tau$, was then applied to estimate the streamwise wavefront correlation function, $R_W(\Delta x)$. The correlation coefficient was then defined by normalizing R_W by the peak value:

$$\rho_w(\Delta x) = \frac{R_w(\Delta x)}{R_w(0)}. \quad (2.7)$$

To calculate the integral correlation length, the correlation coefficient $\rho_w(x, \Delta x)$ was integrated along the Δx coordinate to the location of the first zero crossing, Δx_{zero} :

$$\Lambda_w(x/\delta) = \int_0^{\Delta x_{\text{zero}}} \rho_w(x, \Delta x) d(\Delta x) \quad (2.8)$$

This choice was made because the negative correlation values past the first zero crossing are not large in magnitude; it has also been shown previously that this region of the correlation function is highly sensitive to finite aperture effects (Smith, et al., 2012; Gordeyev, et al. 2014).

The integral correlation length was computed for the baseline TBL wavefront data and for both single LEBU cases. The results for both single LEBU devices are shown in Figure 2.14, normalized by the baseline correlation lengths, in order to determine the relative reduction in streamwise correlation length for the modified TBLs. For both devices these results show definite reductions of 15 – 34% in correlation length for the LEBU modified TBLs, depending on the LEBU configuration and streamwise location. LEBU with $h = 0.6\delta$ gives the largest reduction in streamwise correlation length over the whole of the optical measurement section, with a maximum reduction of approximately 34% at $x = 4 - 5\delta$.

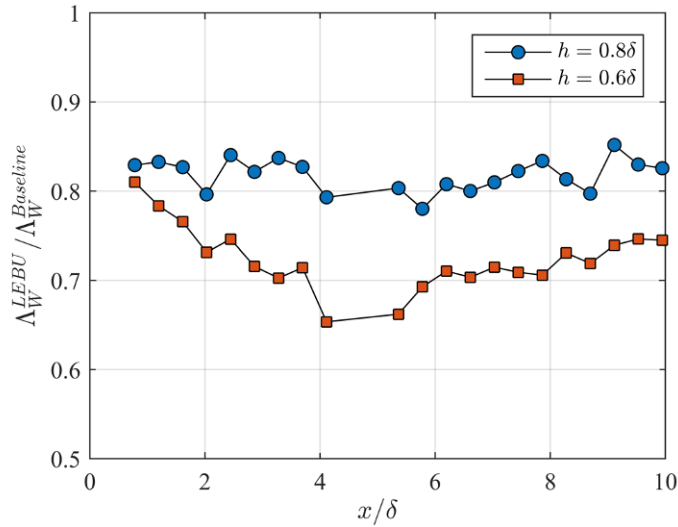


Figure 2.11. Integral correlation length computed from equation (2.8) as a function of streamwise location.

2.3.3 Single LEBU Parametric Study

In order to identify the optimal single LEBU device parameters that yield the largest sustained reductions in OPD_{rms} across the optical measurement section in the present study, a parametric investigation of LEBU chord length, l , and height, h , was performed. For this investigation, the LEBU length was varied between $l = 0.8\delta$ and 4δ , and the height was varied between $h = 0.3\delta$ and either 0.8δ or 1.0δ .

Effect of Device Length and Height

To investigate the effect of LEBU device length on OPD_{rms} in the manipulated turbulent boundary layer, Figure 2.12 presents the results of wavefront measurements obtained at fixed

height $h = 0.6\delta$ for several different chord lengths. This particular height was chosen because it gave the best results for the preliminary single LEBU investigation presented in the previous chapter. Note that these data are normalized by the baseline OPD_{rms} , which was measured for the un-modified TBL.

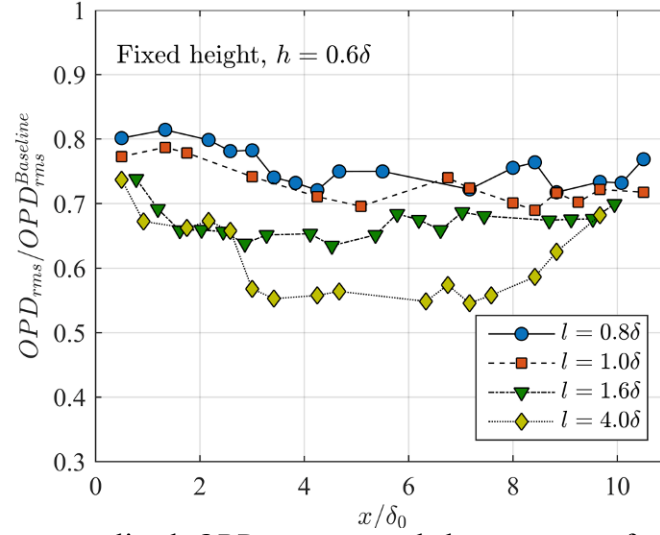


Figure 2.12. Baseline-normalized OPD_{rms} measured downstream of single LEBU devices with fixed height ($h = 0.6\delta$) for different chord lengths, l .

It is evident from the data presented in Figure 2.12 that device chord length, l , had a significant impact on the level of aero-optic mitigation that was achieved. In general, longer devices yield larger reductions than shorter devices; the longest LEBU device tested was 4δ in length, and gave reductions in OPD_{rms} on the order of 40 - 45% over a significant portion of the measurement section. Based on these results, it is possible that longer LEBUs could be even more effective at suppressing aero-optic aberrations in the TBL. This result is consistent with experimental findings from Plesniak (1984) and Savill & Mumford (1988) for C_f reductions in LEBU manipulated TBLs, who tested LEBUs up to 5δ in length and found no global optimum value for l/δ .

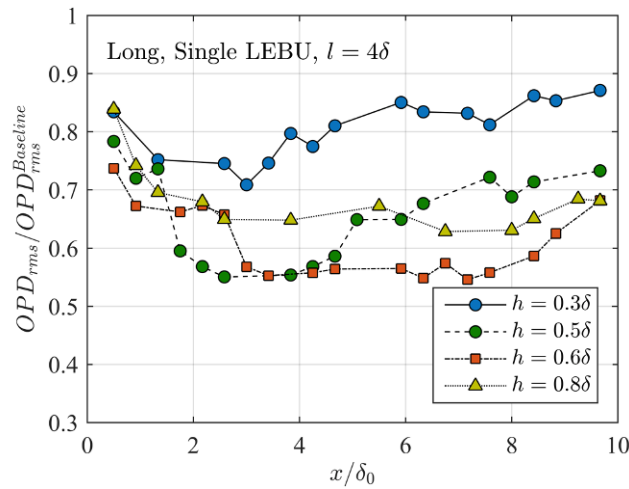


Figure 2.13. Baseline-normalized OPD_{rms} measured downstream of a long single LEBU ($l = 4\delta$) at different plate heights, h .

Baseline-normalized OPD_{rms} obtained for the long, single LEBU, $l = 4\delta$ device at several different heights are presented in Figure 2.13 in order to demonstrate the effect of LEBU height on the aero-optic characteristics of the manipulated TBL. For the case where the LEBU was the closest to the wall, $h = 0.3\delta$, there was about a 15% reduction in OPD_{rms} just downstream of the device trailing edge. Between $x = 3 - 4\delta$, OPD_{rms} reached a minimum value between $0.7 - 0.75$ of the baseline value, $OPD_{rms}^{BASELINE}$. Downstream of this location, OPD_{rms} increased to about $0.85 OPD_{rms}^{BASELINE}$ by $x = 6\delta$, and to nearly $0.9 OPD_{rms}^{BASELINE}$ as x approached 10δ . For the LEBU placed at the next-to-lowest height in this study, $h = 0.5\delta$, OPD_{rms} was initially reduced by greater than 20%, and by 2δ downstream of the device trailing edge it rapidly dropped to below $0.6 OPD_{rms}^{BASELINE}$ (i.e. >40% reduction). OPD_{rms} remained below $0.55 - 0.6 OPD_{rms}^{BASELINE}$ for the region $x \approx 2 - 5\delta$. Between $x = 5 - 7\delta$, however, it increased to $0.7 OPD_{rms}^{BASELINE}$ and remained between $0.7 - 0.75 OPD_{rms}^{BASELINE}$ until the end of the measurement section around 10δ .

For the case in which the LEBU was placed slightly higher up in the boundary layer at $h = 0.6\delta$, OPD_{rms} reduced to approximately $0.56 OPD_{rms}^{BASELINE}$ by 3δ downstream, and OPD_{rms} remained between $0.55 - 0.6 OPD_{rms}^{BASELINE}$ (i.e. a 40 – 45% reduction in aberrations) up to $x \approx 8.5\delta$. Beyond this point, OPD_{rms} increased from 0.6 to almost 0.7 as x approached 10δ , indicating that the aero-optic environment in the manipulated TBL might have been beginning to recover back towards the canonical state. The final tested LEBU height, $h = 0.8\delta$, showed similar reductions in OPD_{rms} greater than 30% were sustained for the remainder of the measurement section, with a local minimum of $0.63 OPD_{rms}^{BASELINE}$ around $x = 7\delta$.

From these data, it appears that near the wall the manipulated flow produces only moderate, short lived reductions in OPD_{rms} , while devices placed near the center of the TBL ($h = 0.5 - 0.6\delta$) yield the largest reductions in TBL induced wavefront aberrations. The LEBU placed slightly above the middle of the TBL at $h = 0.6\delta$ yielded the largest sustained streamwise length of reduction in OPD_{rms} . In this case reductions in OPD_{rms} were on the order of 45% over nearly 6δ , and were greater than 30% for about 9δ . For the device closest to the TBL edge ($h = 0.8\delta$), OPD_{rms} was reduced by more than 30% for about 8δ in the streamwise direction, but the maximum level of reductions was less than that observed for the $h = 0.6\delta$ case.

Optimal Single LEBU Configuration

The results of the parametric study of LEBU length and height and their effect on aero-optic aberrations in the TBL were summarized concisely by analyzing a few key criteria for evaluating the performance of each configuration:

- the minimum value of $OPD_{rms}^{LEBU} / OPD_{rms}^{BASELINE}$ obtained for each configuration, and
- the continuous length L over which OPD_{rms} is reduced below some threshold value.

The threshold values of 20% and 30% reductions in OPD_{rms} were chosen based on the observations from experiments, thus the lengths for each are denoted $L_{(20\%)}$ and $L_{(30\%)}$, respectively.

The first measure of LEBU effectiveness is plotted in Figure 2.14 as a function of LEBU device height for devices of different length. The results clearly show that for all chord lengths, the maximum reduction in OPD_{rms} occurs where the LEBUs are placed around the center of the TBL near $h = 0.5 - 0.6\delta$. It is also evident from this data that the magnitude of reductions in

OPD_{rms} monotonically increases with device chord length regardless of LEBU height, with the exception of $l/\delta = 0.8$ and 1.0 at $h = 0.8\delta$. This behavior is consistent the findings of parametric studies from previous authors (Plesniak, 1984; Savill & Mumford, 1988) investigating local C_f reductions in LEBU manipulated TBLs, who tested LEBUs up to 5δ in length and found no global optimum value for l/δ with regard to the maximum reduction in C_f . Recall that the best value often cited for LEBU drag-reduction devices, $l = 0.8 - 1.6\delta$ (Anders, 1990), was found from optimizations seeking the minimum *net* drag; in these works long chord lengths were found to add too much device drag to be effective.

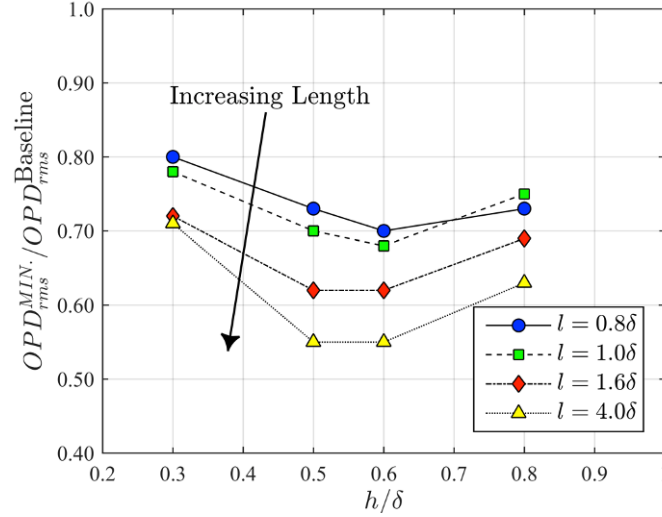


Figure 2.14. Minimum values of $OPD_{rms}^{LEBU} / OPD_{rms}^{BASELINE}$ as a function of device height for single LEBU devices of different chord lengths.

Figure 2.15 presents the streamwise lengths $L_{(20\%)}$ and $L_{(30\%)}$, over which OPD_{rms} is reduced by 20% and 30% in the modified TBL. It should be noted here that streamwise extent of the study is limited to 10δ , so the maximum value of any L obtained from this experiment is 10δ . It is possible that for some single LEBU configurations where L was found to be 10δ that in reality L is greater than 10δ . The present study refrains from speculation as to which cases this may or may not occur in, but an extension of the optical measurement section beyond 10δ in future work can be used to investigate this further if it is deemed necessary. In Figure 2.15a it was found that the continuous length over which OPD_{rms} was reduced by 20% or more is maximized for $h = 0.6\delta$ for all LEBU devices. LEBU length was also shown have a notable effect, with the value of $L_{(20\%)}$ increasing with l/δ .

The results for $L_{(30\%)}$ are plotted in Figure 2.15b as a function of LEBU height, for devices of different length. Note that increasing the threshold to reductions greater than or equal to 30% in OPD_{rms} only preserves cases in which $l = 1.6 - 4\delta$ and $h = 0.5 - 0.8\delta$. Again for these data, $h = 0.6\delta$ is the optimal height for producing long regions of aero-optic mitigation. The $l = 4\delta$, $h = 0.6\delta$ Long LEBU device gives the largest region of reduction over 30% $L_{(30\%)} \approx 9\delta$. Note that this configuration also provides the largest local reduction in OPD_{rms} , as shown in Figure 2.14.

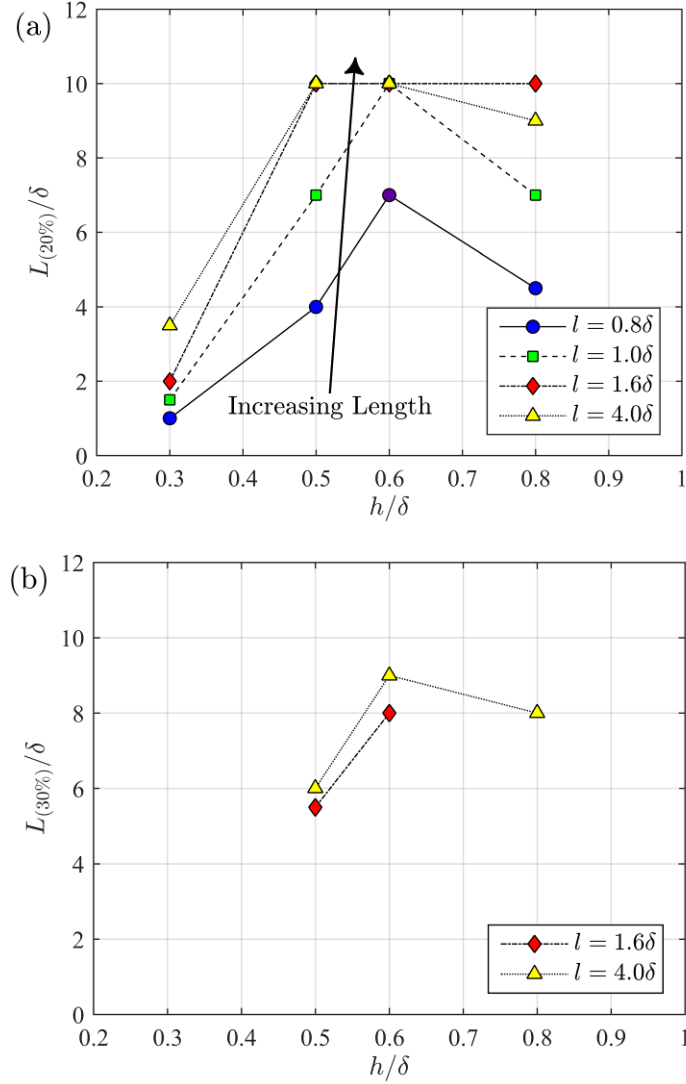


Figure 2.15. The streamwise distance over which OPD_{rms} was reduced by a) more than 20% and b) more than 30% with respect to the value measured for the un-manipulated TBL.

Table 2.2. Multiple Element LEBU Device Configurations

Multiple Element LEBU Devices ($l/\delta = 1.6$)

	h_1/δ	h_2/δ	s/δ	Measurement Type(s)
Multi-LEBU	0.9	0.6	-	◆
	0.8	0.5	-	◆
	0.6	0.3	-	◆
Tandem LEBU	0.6	-	4.0	◆
	0.6	-	8.0	◆◆

Legend



Malley probe wavefront measurements single modified TBL



Single and double modified TBL cases for wavefront measurements

2.3.4 Multiple-Element LEBU Devices

While single LEBUs have been shown to give sustained reductions in OPD_{rms} on the order of 30%, the effectiveness of multiple-element LEBU devices, including multi-LEBU (vertically stacked, see Figure 2.1b) and tandem LEBU (horizontally spaced, see Figure 2.1c) devices, should be assessed to investigate whether or not the additional elements result in any further reduction in levels of OPD_{rms} .

Multi-LEBU Devices

Overall levels of OPD_{rms} were computed and normalized by the baseline OPD_{rms} ; these results are presented in Figure 2.16. For the $h_1/\delta = 0.9, h_2/\delta = 0.6$ and $h_1/\delta = 0.8, h_2/\delta = 0.5$ multi LEBU configurations, aero-optic distortions were reduced by about 20% immediately downstream of the devices, which compares well with the reductions observed for the single LEBU device with $l/\delta = h/\delta = 0.6$. Further downstream of the LEBU device, the levels of OPD_{rms} for both of these multi LEBU devices continue to decrease with respect to the baseline measurements, reaching a maximum reduction of approximately 30% around the streamwise position of 7δ . Compared to the single LEBU result, this location of the maximum reduction is approximately 2δ further downstream, and is approximately the same strength as the reductions from the single LEBU device. Beyond the location of the maximum reduction for both of these multi LEBUs, the levels of OPD_{rms} for $h_1/\delta = 0.8, h_2/\delta = 0.5$ appear to begin recovery towards the un-modified boundary layer state, while OPD_{rms} for $h_1/\delta = 0.9, h_2/\delta = 0.6$ is shown to be leveling out around 70% of the baseline value. These results appear to indicate that the effect for multi LEBUs do not seem to be additive, as the results for the $h_1/\delta = 0.9, h_2/\delta = 0.6$ multi LEBU do not show a simple increase in the reductions detected for the $h/\delta = 0.6$ single LEBU device.

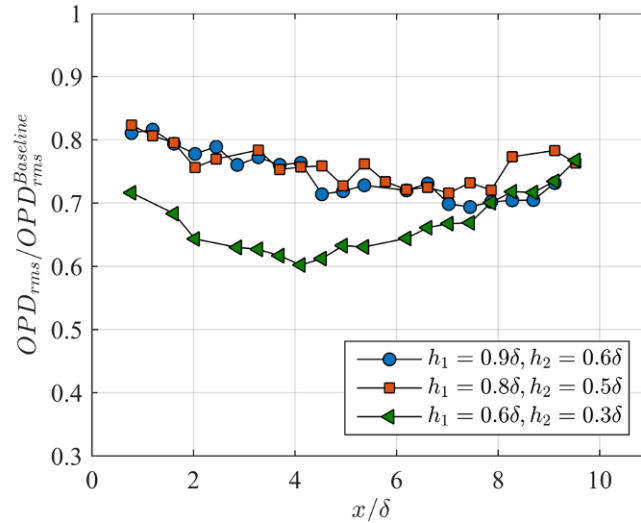


Figure 2.16. Streamwise development of OPD_{rms} for multi LEBU devices of different heights.

For the $h_1/\delta = 0.6, h_2/\delta = 0.3$ multi LEBU configuration OPD_{rms} was reduced by about 30% immediately downstream of the device trailing edge, and OPD_{rms} continued to decrease, resulted in a large, relatively flat range of reduction between 2δ and 6δ where levels are about 40% less than those of the baseline OPD_{rms} . Beyond 6δ downstream of this multi LEBU device, levels of OPD_{rms} begin to recover toward the un-modified TBL levels, reaching about 80 % of the baseline value by 10δ .

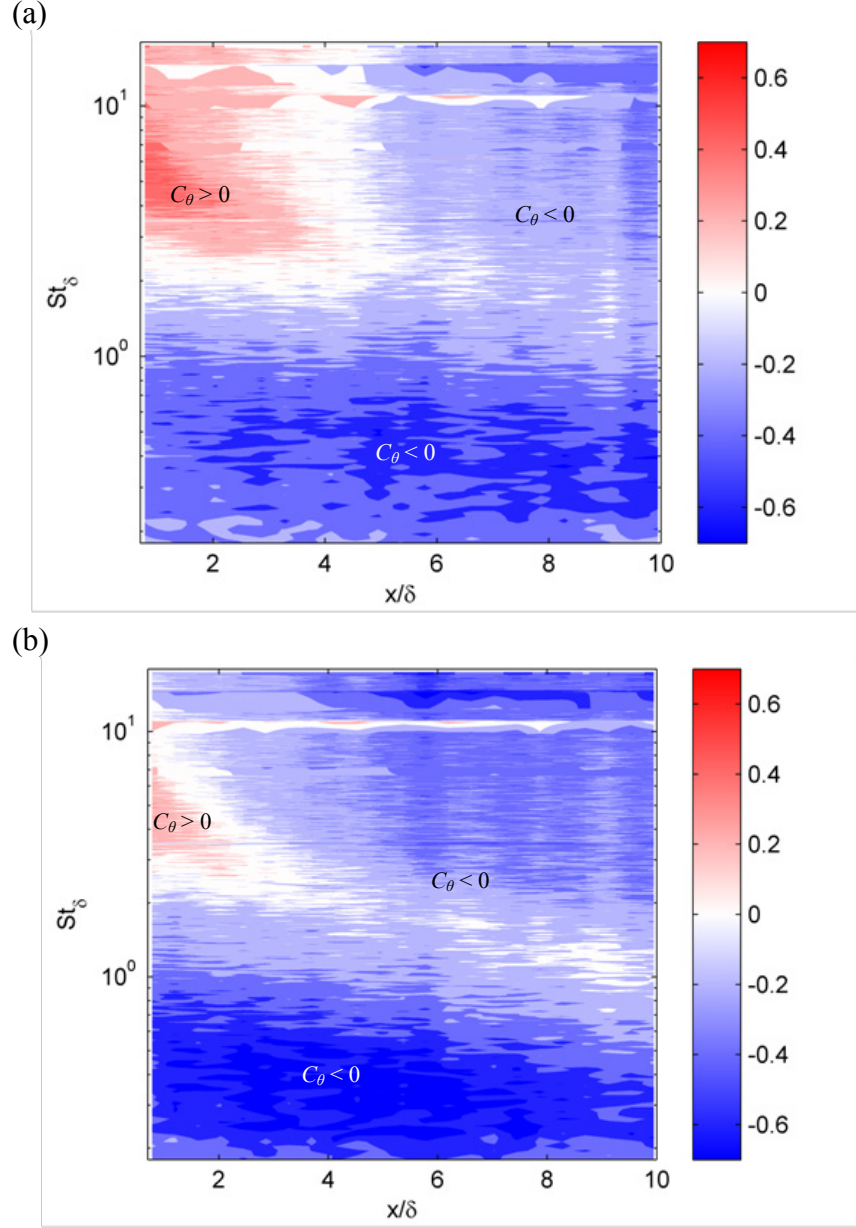


Figure 2.17. Baseline-normalized spectrum surfaces $C_\theta(x/\delta, St_\delta)$ for two Multi-LEBU devices; a) $h_1 = 0.9\delta, h_2 = 0.6\delta$, and b) $h_1 = 0.6\delta, h_2 = 0.3\delta$.

Contour plots of $C_\theta(x/\delta, St_\delta)$, which was defined previously in equation (2.3), are presented in Figure 2.17 for two multi LEBU device configurations. For the $h_1/\delta = 0.9, h_2/\delta = 0.6$ device, shown in Figure 2.17a, in the region immediately downstream of the LEBU ($x = 1-4\delta$) there is a significant reduction in the deflection angle spectrum over the baseline values below $St_\delta \approx 2$, and an increase above the baseline values in the high-frequency, $St_\delta > 3$, end of the spectrum. This increase over the baseline value is reduced with increasing downstream distance, until after $x \sim 4\delta$, where the high-frequency end of the spectrum ($St_\delta > 2$) is reduced below the baseline values. For the low-frequency portion of the deflection angle amplitude spectrum ($St_\delta < 2$), the strength of the reduction of the multi-LEBU modified spectrum increases, especially around a value of $St_\delta = 0.4$. In addition, as the measurement location increases from 4 to 10δ , the region of low-frequency

suppression achieved by this particular LEBU device is reduced slightly in Strouhal number space as the peak of the LEBU-modified deflection angle spectrum approaches the baseline level and baseline location around $St_\delta \approx 1$.

The normalized spectrum surface, shown in Figure 2.17b, for the $h_1/\delta = 0.6, h_2/\delta = 0.3$ multi LEBU device bears some qualitative similarities to the spectrum shown in Figure 2.17a, but quantitatively the effect of this LEBU is shown to be much more significant. Immediately downstream of the LEBU trailing edge, the LEBU modified deflection angle spectrum is reduced by approximately 60% compared to the baseline deflection angle spectrum below $St_\delta = 2$. This strong low-frequency reduction is sustained up to approximately 6δ , where the low-frequency ($St_\delta < 2$) end of the deflection angle spectrum begins to recover towards the baseline spectrum. Also just downstream of the LEBU device, there is a slight 20% increase in a portion of the high-frequency ($2 - 7\delta$) end of the deflection angle spectrum. This increase disappears entirely beyond 3δ downstream of the LEBU device. Beyond $3 - 4\delta$, the entire high-frequency range of the deflection angle spectrum shows a reduction over the baseline of approximately 40 % above $St_\delta = 3$, indicating a decrease in dissipation relative to the baseline flow. This effect is likely the result of the suppression of low-frequency ($St_\delta < 2$) structures beginning immediately downstream of the LEBU trailing edge which yields an overall reduction in the amount of energy cascading into small scales. At $x = 10\delta$, the peak of the LEBU modified spectrum is approaching $St_\delta = 1$, which is another indication (along with the recovery of overall levels of OPD_{rms} towards the baseline value) that the aero-optic reduction effects of this LEBU configuration are starting to wear off by 10δ .

Tandem-LEBU Devices

Malley probe wavefront measurements were also performed for the tandem LEBU devices and overall levels of OPD_{rms} for each tandem LEBU device were computed for streamwise locations $x = 0.8\delta$ to 10δ , and the results, normalized by the baseline OPD_{rms} , are shown in Figure 2.18. For both tandem LEBU configurations, the level of aero-optic distortions just downstream of the LEBU is reduced by approximately 30%. Further downstream, levels of OPD_{rms} for the $s = 4\delta$ tandem LEBU device remain relatively constant around 70% of the baseline value until $x \approx 10\delta$. Downstream of it, the aero-optical distortions appear to be increasing slightly towards the baseline value. For the $s = 8\delta$ tandem LEBU device, OPD_{rms} continues to decrease further downstream until reaching a region of maximum reduction between $4-6\delta$, where the levels of LEBU-modified OPD_{rms} are reduced by about 42% compared to the baseline. Downstream of the streamwise location of 6δ , the levels of OPD_{rms} begin to recover slightly towards the baseline levels, but the rate of recovery is more gradual than what was observed for the $h_1 = 0.6\delta, h_2 = 0.3\delta$ multi LEBU device (which had the largest maximum reduction in OPD_{rms}), with the OPD_{rms} at $9-10\delta$ being approximately 35% lower than the baseline measurement. This result indicates that the tandem LEBU device results in the most significant reduction in OPD_{rms} over a longer streamwise extent than any of the other tested LEBU configurations.

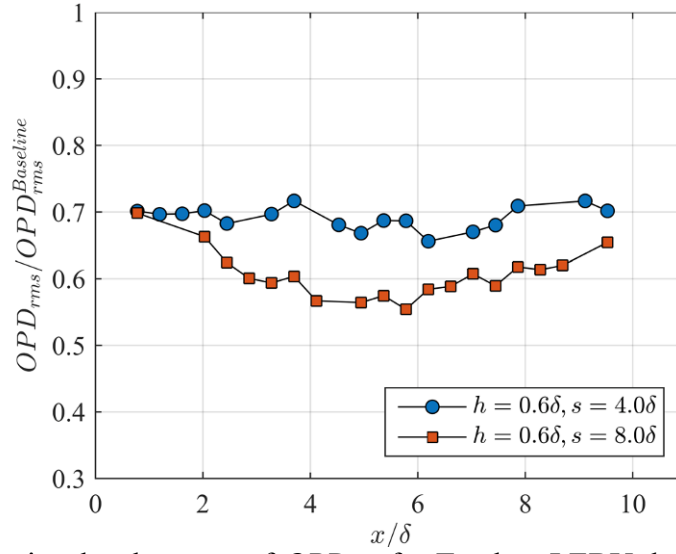


Figure 2.18. Streamwise development of OPD_{rms} for Tandem LEBU devices with separations $s = 4\delta$ and 8δ , compared to the best-performing single and multi-LEBU results.

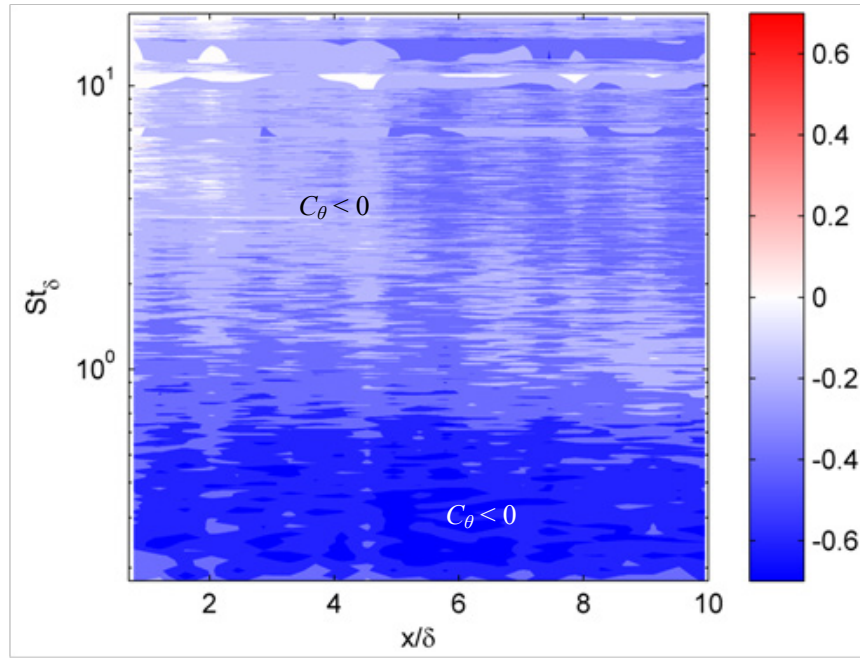


Figure 2.19. Baseline-normalized spectrum surfaces $C_\theta (x/\delta, St_\delta)$ for $h = 0.6 \delta$, $s = 8\delta$ tandem LEBU devices.

The streamwise evolution of the baseline-normalized deflection angle spectra are presented in Figure 2.19 for $h = 0.6 \delta$, $s = 8\delta$ tandem LEBU device. The region of suppression in the low-frequency end of the spectrum ($St_\delta < 1$) shows an overall stronger suppression of aerodynamic spectrum compared to the 4δ tandem LEBU at the same frequency range (not shown). Additionally, for streamwise locations $x > 4\delta$ there is an increasingly strong reduction in the high-frequency end of the deflection angle spectrum. This is likely a result a reduction in the amount of energy cascading into smaller-scales at which turbulence dissipation occurs. For this tandem

LEBU, the baseline-normalized spectrum peak is also observed to shift to lower-frequencies as the streamwise location increases, moving from a value around $St_\delta = 6$ to about $St_\delta = 1$. At 10δ , however, the suppression of large-scale structures ($St_\delta < 1$) is still rather strong, so it is possible that levels of optical aberrations will remain low for several more TBL thicknesses before beginning to relax to the baseline values.

Velocity Measurements

Earlier in this report (Section 2.3.1), velocity measurements at several streamwise locations in the LEBU-modified TBL were presented along with aero-optic wavefront measurements for limited number of Single LEBU devices. The effects of LEBUs on velocity and wavefront statistics were then compared, and the results from both measurement techniques indicated that frequencies associated with large-scale turbulent structures in the TBL were suppressed by the devices. Both measurements also able to identify LEBU-induced changes to the TBL turbulence structure in the modified boundary layer. Additional comparisons of velocity and wavefront statistics in the LEBU modified TBL are presented in this section for selected LEBU configurations at a single streamwise location: $x = 6\delta$. This streamwise location was chosen as it is roughly in the middle of the optical measurement section, and it has been shown from the data presented in previous sections that substantial reductions in OPD_{rms} were achieved at this location for several different LEBU devices. The particular manipulators that will be examined in this section are as follows:

- Long single LEBU: $l = 4\delta$, $h = 0.6\delta$,
- Multi LEBU: $l = 1.6\delta$, $h_1 = 0.6\delta$, $h_2 = 0.3\delta$, and
- Tandem LEBU: $l = 1.6\delta$, $h = 0.6\delta$, $s = 8\delta$.

Recall that the model for calculating OPD_{rms} for compressible TBLs have been derived using Sutton's linking equation (1.2) and the Strong Reynolds Analogy, Gordeyev et al, 2014. The terms in the SRA are easily arranged to show that at a particular y -value ρ_{rms} in the TBL is proportional to the product $U(y) u_{rms}(y)$:

$$\frac{\rho_{rms}(y)}{\rho_\infty} = r(\gamma - 1)M_\infty^2 \frac{U(y)u_{rms}(y)}{U_\infty^2}. \quad (2.9)$$

One possible modification of the form of the SRA given in equation (2.9) can be arrived at by substituting the energy spectral density for the root-mean-square terms on both sides of the equation. Since the energy spectral density of any arbitrary variable $\xi(t)$ describes how its total variance, ξ_{rms}^2 , is distributed over the component frequencies that ξ may be decomposed into. In other words, $\xi_{rms}^2(f) = S_\xi(f)$, where $S_\xi(f) = F\{\xi^2(t)\}$ is the one-sided energy spectral density of ξ , and F denotes the Fourier transform. Therefore, equation (2.9) can be re-written in the form

$$\rho_{rms}^2(y, f) = S_{SRA}(y, f) \times \left(\frac{r(\gamma - 1)\rho_\infty M_\infty^2}{U_\infty^2} \right)^2 \quad (2.10)$$

where

$$S_{SRA}(y, f) = F\{[U(y)u(y, t)]^2\}. \quad (2.11)$$

This decomposes the first term of the integrand in the linking equation (1.2) into a function of frequency and wall-normal location. Assuming that the SRA is valid in the LEBU modified TBL, this approach can be used to identify where in both frequency and wall-normal space the LEBU

devices are causing reductions in ρ_{rms} . To easily visualize this, the ratio of the LEBU-modified to baseline energy spectra was computed:

$$C_{SRA}\left(\frac{y}{\delta}, St_{\delta}\right) = \frac{S_{SRA}^{LEBU}(y/\delta, St_{\delta})}{S_{SRA}^{BASELINE}(y/\delta, St_{\delta})}. \quad (2.12)$$

Here it is emphasized that $C_{SRA} < 1$ indicates a reduction in density fluctuations in the LEBU-modified boundary layer, while $C_{SRA} > 1$ implies an increase in density fluctuations. Filled contour plots of equation (2.12) are shown in Figure 2.20 for selected LEBU devices at $x/\delta = 6$.

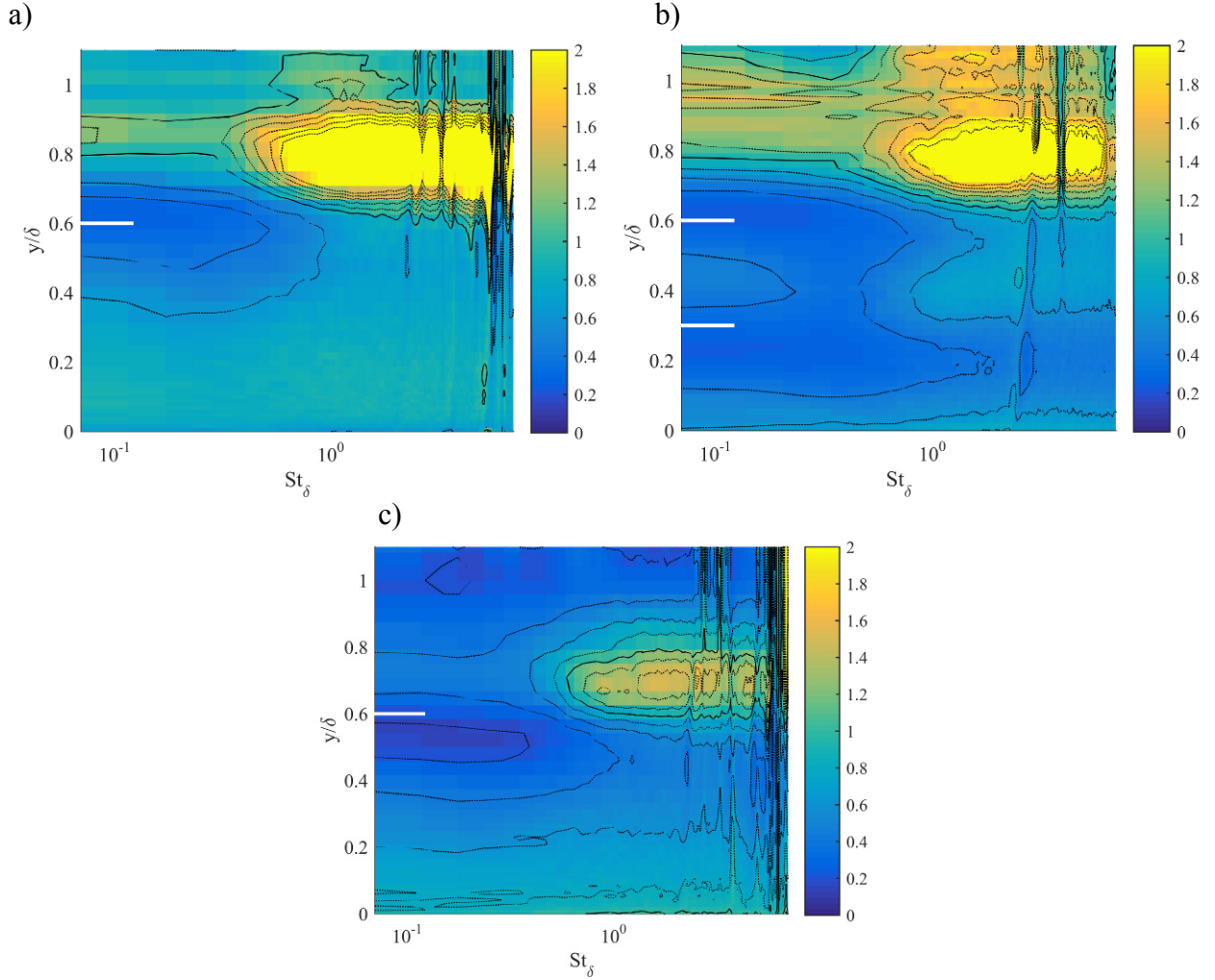


Figure 2.20. Contour plot of $C_{SRA}(y/\delta, St_{\delta})$ at $x = 6\delta$ for a) $l = 4\delta, h = 0.6\delta$ Long Single LEBU, b) $h_1 = 0.6\delta, h_2 = 0.3\delta$ Multi-LEBU and c) $s = 8\delta$ tandem LEBU devices. LEBU element height is marked by white lines, and the solid black contour indicates where $C_{SRA}(y/\delta, St_{\delta}) = 1.0$.

The characteristics of the spectra surfaces presented in Figure 2.20 are consistent with other velocity and wavefront spectra presented in this and the previous chapters. The SRA-estimated fluctuating density spectra show that the LEBU devices all produce reductions in low frequencies, $St_{\delta} < 1$ (i.e. large scales) below the LEBH height. Note that for Multi-LEBU device in Figure 2.20b, there is a ‘pocket’ of low-frequency turbulence suppression below *both* LEBU elements. These spectra also show that LEBUs cause an increase in high-frequencies, $St_{\delta} > 1$

(corresponding to small scale structures) at wall-normal locations $y > h$, which corresponds to turbulence production due to the increased mean velocity gradient at this location. The magnitude of these increases is especially large for long single LEBU and multi-LEBU devices.

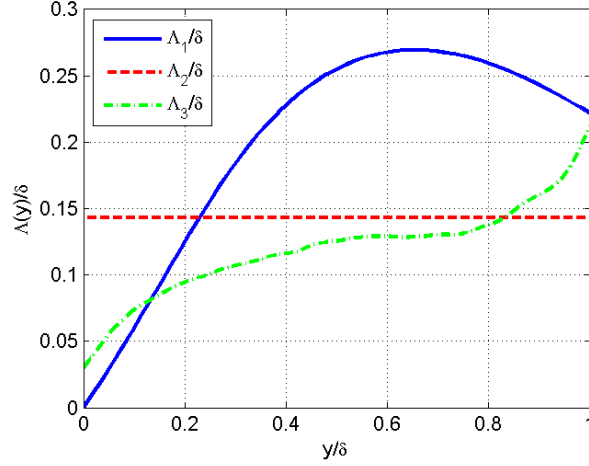


Figure 2.21. Wall-normal density correlation length functions for the canonical turbulent boundary layer; Λ_1 presented by Gilbert (1982), Λ_2 measured by Rose & Johnson (1982), and Λ_3 computed from DNS of a $Re_\theta = 3550$ TBL by Wang & Wang (2012).

The SRA-estimated $\rho_{rms}(y)$ profile for the LEBU-modified TBL is easily obtained from the energy spectrum S_{SRA} by integrating in the frequency domain:

$$\rho_{rms}(y) = \frac{r(\gamma-1)\rho_\infty M_\infty^2}{U_\infty^2} \left(\int_0^\infty S_{SRA}(y, f) df \right)^{1/2}. \quad (2.13)$$

Note that it can easily be shown that equation (2.13) is equivalent to equation (2.9); however, computing ρ_{rms} from equation (2.13) allows for the possibility of spectral filtering if there is significant noise in the velocity measurements.

It follows from equation (2.13) that the simplified form of Sutton's linking equation (1.2) can be re-written as:

$$OPD_{rms} = \sqrt{2} K_{GD} (\gamma-1) \rho_\infty \delta M_\infty^2 \left[\int_0^\infty r^2 \left(\frac{U(y) u_{rms}(y)}{U_\infty^2} \right)^2 \frac{\Lambda_\rho(y)}{\delta} d\left(\frac{y}{\delta}\right) \right]^{1/2}. \quad (2.14)$$

Remember here that $\Lambda_\rho(y)$ is the wall-normal density correlation length, which can either be estimated experimentally (although with some difficulty) from hot-wire velocity measurements, or computed directly from CFD results (e.g. Wang & Wang, 2012). Several different density correlation lengths from the literature that have been used for modeling TBL aero-optic aberrations are presented in Figure 2.21. These functions have all been shown to give similar results for models of canonical subsonic and supersonic TBLs (Gordeyev, et al., 2012; Gordeyev, et al. 2014).

For LEBU-manipulated TBLs, it was not expected that the functional forms of Λ_ρ presented in Figure 2.21 is an appropriate estimate for the actual wall-normal density correlation length, since LEBU devices significantly modify streamwise and spanwise correlations in manipulated boundary layers. However, if OPD_{rms} is estimated from equation (2.14) using the any one of the approximations for Λ_ρ for the canonical TBL, the influence of LEBU-modified wall-

normal correlation length can be quantified by comparing predicted levels of reductions to those measured using the Malley probe.

Table 2.3. Comparison of directly measured and indirectly estimated values of OPD_{rms} in LEBU modified TBLs at $x = 6\delta$.

LEBU Device Configuration		$OPD_{rms}^{LEBU} / OPD_{rms}^{BASELINE}$			
		Measured (Malley Probe)	From Eqn. (2.15), with $\Lambda_\rho(y) =$ Λ_1	Λ_2	Λ_3
Single LEBU	$\left\{ \begin{array}{l} l/\delta = 1.6 \\ h/\delta = 0.6 \end{array} \right.$	0.68	0.82	0.87	0.84
Long Single LEBU	$\left\{ \begin{array}{l} l/\delta = 4 \\ h/\delta = 0.6 \end{array} \right.$	0.55	0.85	0.88	0.86
Multi-LEBU	$\left\{ \begin{array}{l} l/\delta = 1.6 \\ h_1/\delta = 0.6 \\ h_2/\delta = 0.3 \end{array} \right.$	0.64	0.78	0.75	0.78
Tandem LEBU	$\left\{ \begin{array}{l} l/\delta = 1.6 \\ h/\delta = 0.6 \\ s/\delta = 8.0 \end{array} \right.$	0.55	0.80	0.83	0.82

The reduction in OPD_{rms} relative to the value predicted from baseline velocity measurements is given in equation (2.15):

$$\frac{OPD_{rms}^{LEBU}}{OPD_{rms}^{BASELINE}} = \sqrt{\frac{\int_0^\infty [\rho_{rms}^{LEBU}(y)]^2 \Lambda_\rho(y) d(y/\delta)}{\int_0^\infty [\rho_{rms}^{BASELINE}(y)]^2 \Lambda_\rho(y) d(y/\delta)}}, \quad (2.15)$$

where the superscripts ‘LEBU’ and ‘BASELINE’ denote quantities for the LEBU modified and baseline TBLs, respectively. Table 2.3 presents the results of that the amount of reduction in OPD_{rms} estimated from the linking equation is significantly under-predicted compared to experimental results. Depending on the correlation function and LEBU case, using the canonical TBL correlation function over-predicts OPD_{rms} in the modified TBL by up to 30% more than the actual value. This result serves as a clear, although indirect, indication that LEBU-induced aero-optic mitigation is not simply achieved by reducing the overall magnitude of density fluctuations in the TBL. Rather, the de-correlating ‘plate’ effects which were found to be a critical mechanism for LEBU drag reduction (Anders, 1990, and references therein) are also an important mechanism for affecting the aero-optic characteristics of LEBU-modified TBLs.

2.4 Conclusions and Discussion

This part of the report presented experimental results of hot-wire velocity and wavefront measurements of TBLs, modified using both single and multi-element LEBU devices. Measurements of mean and fluctuating velocity profiles downstream of LEBU device, the LEBU was found to cause localized reductions in mean velocity downstream of the LEBU device, as

well as reductions in u_{rms} throughout the modified boundary layer. Significant reductions in u_{rms} were found in the LEBU modified boundary layer spectra – especially at low frequencies – over a significant portion of the boundary layer thickness. Some evidence was found that LEBUs introduced a significant amount of small-scale turbulent structures into the LEBU wake; however these are shown to dissipate quickly in the velocity spectra. These findings are consistent with the results of velocity measurements from previous studies (Corke, 1981; Lemay, et al. 1990).

It was shown that LEBU devices are capable of reducing OPD_{rms} of wavefront aberrations caused by turbulent boundary layers by 30 – 35% over streamwise distances of several δ 's. The LEBUs caused this reduction by suppressing large-scale turbulent motions in the modified TBL. These results confirm the theory that careful manipulation of large-scale turbulent structures in aero-optically active flows will be effective for mitigating aero-optic aberrations, and also demonstrate that LEBUs are an effective flow control device for achieving this goal.

From careful analysis of wavefront deflection angle spectra, it was also shown that it is possible to gain some physical insight about the changes to the modified TBL. For example, inspection of wavefront deflection angle spectra showed that the LEBU devices suppressed large-scale turbulent structures in the manipulated boundary layer. This result is consistent with the findings obtained of velocity measurements. Also, changes in turbulence production and dissipation, as well as spectral features associated with the growth of the LEBU wake were identified through analysis of wavefront data. This supports the idea that it is possible to study changes to compressible turbulent flow structure using non-intrusive aero-optic wavefront sensors, which was initially put forth by Sutton (1969).

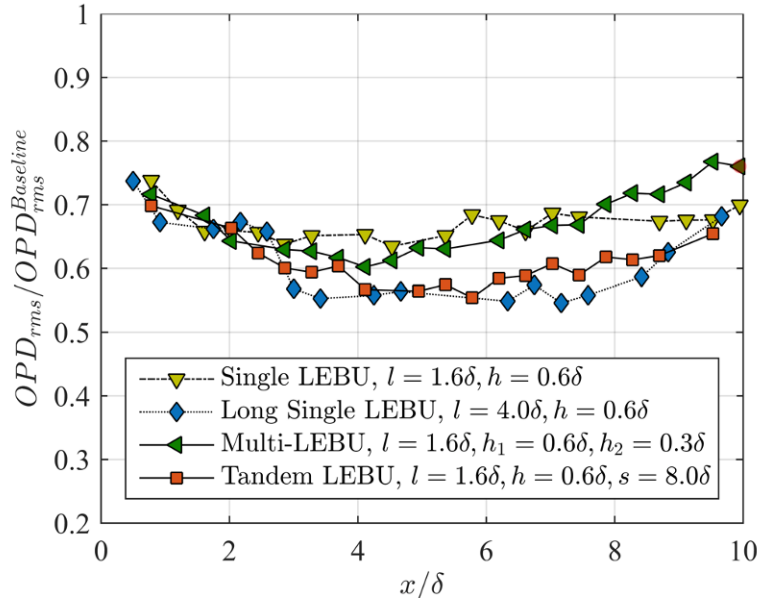


Figure 2.22. Baseline normalized OPD_{rms} downstream of selected “best” LEBU device configurations.

After analyzing all cases from the parametric investigation, the optimal *tested single* LEBU configuration was identified as the $l = 4\delta$, $h = 0.6\delta$, ‘long’ LEBU device. This configuration resulted in a maximum reduction in OPD_{rms} of approximately 45%, and also gave sustained reductions over 40% for 6δ in the streamwise direction, and reductions in OPD_{rms} over 30% for 9δ . The word ‘tested’ is emphasized above, as the optimal length found in this parameter

space resided on the edge, which leaves open the possibility that LEBUs of even longer chord length will give even larger reductions in OPD_{rms} , although LEBUs with increasing chord length will result in additional device drag.

The effects of Multi-LEBU and Tandem-LEBU devices on aero-optic aberrations in the TBL were also investigated using a number of configurations. A summary of results for the best-performing types of LEBU are presented in Figure 2.22. The results demonstrated that the best-performing Tandem-LEBU configuration for aero-optic mitigation is two-element tandem LEBU with $l = 1.6\delta$, $h = 0.6\delta$, and $s = 8\delta$. This configuration gave the maximum reduction in OPD_{rms} of more than 40% downstream of the device to about 5δ , and reductions greater than about 35% over a large streamwise range between 1δ and 10δ . Similar reductions in OPD_{rms} of 35% were also shown for a multi-LEBU device with $l = 1.6\delta$, $h_1 = 0.6\delta$, $h_2 = 0.3\delta$, although the streamwise extent of the reduction was limited to about 4δ .

Additional velocity measurements were also obtained at a single streamwise station for several selected single, tandem, and multi-LEBU device configurations. The fluctuating density spectra were estimated for each of these devices using the Strong Reynolds Analogy, and the results were showed that significant reductions in the contributions from large scales below the LEBU devices, and increased small scale turbulent fluctuations above the LEBU device that are consistent with increased production on the upper side of the LEBU wake. Estimates of OPD_{rms} were also computed from velocity data through Sutton's linking equation, and the results gave indirect evidence that changes in wall-normal correlation length are also a key mechanism responsible for reducing aero-optic aberrations in the LEBU-modified TBL.

Levels of aero-optic mitigation for two tested multi-element LEBU configurations were shown to be better than levels of mitigation achieved by the $l = 1.6\delta$ single-element LEBU device. However, the long $l = 4\delta$ LEBU performed better than both of the tandem and multi LEBU devices, although only just slightly. These results demonstrate that aero-optic aberrations caused by the TBL can be easily and significantly suppressed by 30 – 40% over several δ in the streamwise direction using Large Eddy Break-Up devices. The mechanical simplicity of LEBU devices, along with the experimental demonstration of their aero-optic mitigation abilities in this work, makes them very good candidates for incorporation into the design of airborne directed energy systems that must contend with aberrations caused by compressible TBLs.

3. Wall Cooling Effects

3.1 Original Aero-Optic Model for Wall Temperature Effects

While aero-optical effects caused by compressible boundary layers have been studied since 1950s, most of the studies have not previously accounted for the potential temperature mismatch between the underlying wall and freestream temperature. So there is a need to investigate the impact that heat transfer at the underlying wall of a subsonic, compressible, turbulent boundary layer has on optical aberrations.

Wyckham and Smits (2009) used a high-speed two-dimensional Shack-Hartmann sensor to study aero-optical properties of subsonic and supersonic boundary layers. Although they did not perform heated wall experiments, they used a bulk-flow analysis and developed a scaling law for aero-optical aberrations for non-adiabatic walls as a function of the freestream Mach number, the local skin friction coefficient, C_f , and the ratio of the freestream static temperature, T_∞ , to the

wall temperature, T_w , $OPD_{rms} \sim K_{GD} \delta M_\infty^2 \sqrt{C_f} \left(\frac{T_w}{T_\infty} + 1 \right)^{-3/2}$. From this scaling law it follows that aero-

optical distortions should decrease when the wall is heated. These predictions contradicted the preliminary experimental studies conducted in Cress et al (2012), where it was shown that aero-optical distortions increase when the wall is heated. White and Visbal (2012) have performed Large Eddy Simulations of aero-optic aberrations caused by compressible turbulent boundary layers for heated and cooled walls and also have shown that aero-optical aberrations increased when the wall was heated. So, there is a need for a statistical model for the OPD_{rms} as a function of subsonic Mach number and moderate temperature difference between the wall and the freestream.

In the previous AFORS-funded work, the Extended Strong Reynolds Analogy was used to derive the model for aero-optical distortions with non-adiabatic wall was derived,

$$OPD_{rms} = A(\rho_\infty / \rho_{SL}) \delta^* M_\infty^2 \left(1 + C_1 \left(\frac{\Delta T}{T_\infty M_\infty^2} \right) + C_1 \left(\frac{\Delta T}{T_\infty M_\infty^2} \right)^2 \right)^{1/2}. \quad (3.1)$$

Cress (2010) reported that using velocity measurements for a boundary layer with $M = 0.5$, C_1 and C_2 were theoretically predicted to be 6.38 and 10.28, respectively. A linearized form of equation (3.1) was also found to work well for modeling wavefront measurements for wall heating, since for $\Delta T > 0$, the third term of (3.1) is much smaller compared than the first two;

$$OPD_{rms} = A(\rho_\infty / \rho_{SL}) \delta^* M_\infty^2 \left(1 + D_1 \left(\frac{\Delta T}{T_\infty M_\infty^2} \right) \right), \Delta T > 0, \quad (3.2)$$

where the empirical constant $D_1 = C_1/2$ (Cress, 2010).

OPD_{rms} computed from Malley probe measurements of heated wall TBLs also showed good agreement between experimental results and the model equations (3.1) and (3.2), as shown in Figure 3.1 for a wide range of wall temperatures and Mach numbers. These experiments demonstrated that OPD_{rms} could be successfully modeled using the linear scaling relationship over a wide range of wall temperature differences and subsonic Mach numbers. The results of these tests also highlighted the fact that even moderate values of wall heating could significantly increase wavefront aberrations above levels encountered for adiabatic wall temperature conditions only (Cress, 2010).

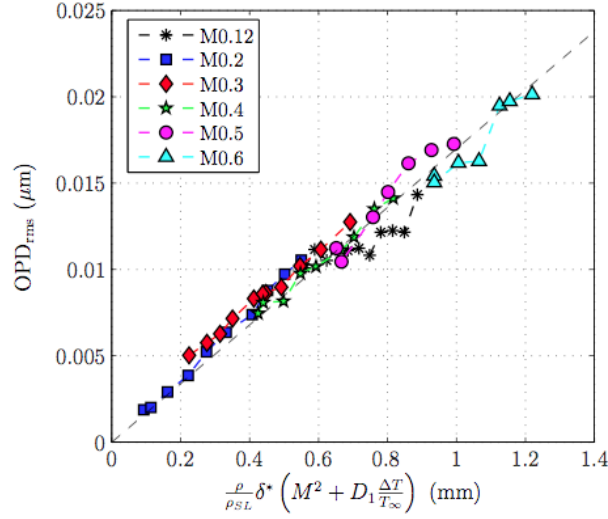


Figure 3.1. OPD_{rms} versus the linearized heated wall temperature scaling, equation (3.2), using empirically determined D_1 constants. [image source Cress (2010)]

3.2. Updated model for non-adiabatic boundary-layer aero-optical distortions

For nearly as long as turbulent boundary layers have been studied, those with a moderate heat transfer at the wall have been the subject of experimental and computational research, especially applied to supersonic and hypersonic boundary layers; see Smits & Dussauge (1996), Spina et al (1994) for summaries of the effects of heat transfer in a compressible, turbulent boundary layer. A significant advancement in the field came in 1962 from Morkovin (1962) presentation of the Strong Reynolds Analogy (SRA), which presumes that p' is negligible. From this analogy between the Reynolds-averaged form of the energy and momentum equations, a relationship between the fluctuating static temperature and fluctuating velocity can be shown to be,

$$\frac{T_{rms}}{\bar{T}} = -A(y)(\gamma - 1)M^2 \frac{u_{rms}}{\bar{U}} \quad (3.3)$$

where $A(y)$ takes into account the stress integral distribution in the boundary layer (Smits & Dussauge, 1996); in the original SRA $A(y) = 1$. Both experiments (Smits & Dussauge, 1996; Debieve, 1983; Smith & Smits, 1993) and DNS simulations (Guarini et al, 2000; Duan et al, 2010) have shown that $A(y) \approx 1$ for $y/\delta < 0.6$ and increases in the outer layer.

However, for non-adiabatic wall conditions, experimental (Debieve et al 1997) and computational (Duan et al, 2010; Liu & Pletcher, 2007) studies have shown that SRA fails to predict the correct temperature fluctuations. Walz (1969) proposed a form of the enthalpy equation such that $\tilde{h} = h(\tilde{u})$, where fluctuations in the total temperature are not ignored (Smits & Dussauge, 1996); and the following relationship for mean static temperature was found,

$$\frac{\tilde{T}}{T_\infty} = \frac{\tilde{T}_w}{T_\infty} + \frac{\tilde{T}_r - \tilde{T}_w}{T_\infty} \left(\frac{\tilde{U}}{U_\infty} \right) - r \frac{(\gamma - 1)}{2} M_\infty^2 \left(\frac{\tilde{U}}{U_\infty} \right)^2 \quad (3.4)$$

where \tilde{T} , \tilde{T}_∞ , \tilde{T}_w , and \tilde{T}_r are the Favre-averaged static, freestream, wall, adiabatic and recovery temperatures, respectively, \tilde{U} is the Favre-averaged mean velocity, M_∞ is the freestream Mach

number and $r = (\tilde{T}_r - \tilde{T}_\infty) / (\tilde{T}_{0_\infty} - \tilde{T}_\infty)$ is the recovery factor. In turbulent boundary layers with air as the fluid in motion, r is typically about 0.89. Equation (3.4) is known by several names: the modified Crocco relation, the Walz equation or the Extended SRA (ESRA).

Linearizing this equation in the case of small fluctuations (Debieve et al, 1997), a relation between temperature and velocity fluctuations becomes,

$$\frac{T''_{rms}}{T_\infty} = \frac{\tilde{T}_r - \tilde{T}_w}{T_\infty} \left(\frac{u''_{rms}}{U_\infty} \right) - r(\gamma - 1) M_\infty^2 \frac{\tilde{U} u''_{rms}}{U_\infty^2} \quad (3.5)$$

where T''_{rms} and u''_{rms} are the Favre-averaged fluctuating temperature and velocity, respectively. Cebesi & Smith (1974) derived a very similar expression with $A(y) = 1$. In general, equation (3.5) can be written in the following form,

$$\frac{T_{rms}}{T_\infty} = \frac{T_r - T_w}{T_\infty} \left(\frac{u_{rms}}{U_\infty} \right) - A(y)(\gamma - 1) M_\infty^2 \frac{U u_{rms}}{U_\infty^2} \quad (3.6)$$

Strictly speaking, equation (3.6) simply postulates the relationship between T_{rms} and u_{rms} , while ESRA, in addition to equation (3.6), also requires that the temperature and velocity fluctuations are perfectly anti-correlated. This was shown not to be true, see for example Debieve et al (1997), Guarini et al (2000), Duan et al (2010), Gaviglio (1987).

The original model, equation (3.2), was derived for subsonic boundary layer only and assuming a particular relations between the temperature and the velocity, equation (3.6). During this work, the model was generalized and extended to a supersonic regime. The derivation is provided below.

From the linking equation (1.2) it follows that if the density fluctuations and their correlation lengths across the boundary layer are known, optical distortions can be calculated. From the ideal gas law, $p = \rho RT$, the density fluctuations, ρ' , are related to pressure fluctuations, p' , and temperature fluctuations, T' . In the case of small fluctuations, it can be written as $\rho' / \rho(y) = p' / p(y) - T' / T(y)$. While the pressure fluctuations in adiabatic boundary layers have been shown to be several times smaller than the temperature fluctuations Wang & Wang (2012), Smits & Dussauge (1996), Spina et al 1994), for cooled walls the temperature fluctuations are smaller than in the adiabatic case, Duan et al (2010). So, the pressure fluctuations can be comparable with the temperature fluctuations.

Using equations (3.4) and (3.6), letting $\Delta T = T_w - T_r$, and replacing fluctuating values with root-mean-square values, the following expression for T_{rms} can be found,

$$\left(\frac{T_{rms}}{T_\infty} \right)^2 = \left(\frac{u_{rms}}{U_\infty} \right)^2 \cdot \left[\left(\frac{\Delta T}{T_\infty} \right)^2 + 2A(y)(\gamma - 1) M_\infty^2 \left(\frac{\Delta T}{T_\infty} \right) \frac{U}{U_\infty} + \left(A(y)(\gamma - 1) M_\infty^2 \frac{U}{U_\infty} \right)^2 \right] \quad (3.7)$$

where $U(y)$ is the mean local streamwise velocity. Thus, the equation of state can be used to compute the density fluctuations, assuming no correlation between the pressure and temperature (we will discuss this assumption later),

$$\left(\frac{\rho_{rms}}{\rho(y)} \right)^2 = \left(\frac{T_{rms}}{T(y)} \right)^2 + \left(\frac{p_{rms}}{P_\infty} \right)^2 \quad (3.8)$$

Here the local pressure is assumed to be constant across the boundary layer. The local density can be found from the equation of state, $\rho(y) = P_\infty / (RT(y)) = \rho_\infty (T_\infty / T(y))$, where the mean temperature profile can be computed from Equation (5a),

$$\frac{T(y)}{T_\infty} = 1 + r \frac{(\gamma - 1)}{2} M_\infty^2 \left(1 - \left[\frac{U(y)}{U_\infty} \right]^2 \right) + \frac{\Delta T}{T_\infty} \left(1 - \frac{U(y)}{U_\infty} \right) \quad (3.9)$$

For non-adiabatic boundary layers, the fluctuating velocity component, compensated for density changes near the wall using the Van Driest transformation, $\frac{u_{rms}}{u_\tau} \sqrt{\frac{\rho(y)}{\rho_w}}$, was found to be mostly unchanged over a wide range of Mach numbers (Spina et al, 1994, Guarini et al, 2000, Duan et al, 2010), so a fluctuating velocity profile from the adiabatic boundary layer, Guarini et al (2000), can be used,

$$\frac{u_{rms}(y)}{u_\tau} \sqrt{\frac{\rho(y)}{\rho_w}} = \frac{u_{rms}(y)}{U_\infty \sqrt{C_f/2}} \sqrt{\frac{\rho(y)}{\rho_\infty}} = \frac{u_{rms}(y)}{U_\infty \sqrt{C_f/2}} \sqrt{\frac{T_\infty}{T(y)}} = g(y/\delta) \quad (3.10)$$

We further assume that the mean velocity profile is independent of the wall temperature as,

$$U(y)/U_\infty = f(y/\delta) \quad (3.11)$$

Finally, the fluctuating pressure profile from Guarini et al (2000) will be used,

$$p_{rms}/(\rho_w u_\tau^2) = p_{rms}/(\rho_w U_\infty^2 (C_f/2)(\rho_\infty/\rho_w)) = p_{rms}/(\rho_\infty U_\infty^2 (C_f/2)) = h(y/\delta) \quad (3.12)$$

where the functions f , g and h are presented in Gordeyev et al. (2015). Substituting equation (3.7) into equation (3.8) and using equations (3.10), (3.11) and (3.12) gives the following relationship for ρ_{rms} in terms of the velocity and the temperature profiles in the wall normal direction for a given ΔT yields,

$$\begin{aligned} \left(\frac{\rho_{rms}}{\rho_\infty} \right)^2 &= \left(\frac{T_\infty}{T(y)} \right)^2 \left[\left(\frac{T_{rms}}{T(y)} \right)^2 + \left(\frac{p_{rms}}{P_\infty} \right)^2 \right] = \left(\frac{T_{rms}}{T_\infty} \right)^2 \left(\frac{T_\infty}{T(y)} \right)^4 + \left(\frac{T_\infty}{T(y)} \right)^2 \left(\frac{p_{rms}}{P_\infty} \right)^2 = \\ &= \left(\frac{T_\infty}{T(y)} \right)^3 (C_f/2) g^2(y) \cdot \left[\frac{\Delta T}{T_\infty} + A(y)(\gamma - 1) M_\infty^2 f(y) \right]^2 + \left(\frac{T_\infty}{T(y)} \right)^2 [\gamma M_\infty^2 (C_f/2) h(y)]^2 \end{aligned} \quad (3.13)$$

Finally, substituting equation (3.13) into equation (1.2) results in the following relationship,

$$\text{OPD}_{rms} = A_0 K_{GD} \rho_\infty \delta \sqrt{C_f} \left[M_\infty^4 + C_1 \frac{\Delta T}{T_\infty} M_\infty^2 + C_2 \left(\frac{\Delta T}{T_\infty} \right)^2 \right]^{1/2} \quad (3.14)$$

where,

$$\begin{aligned} A_0^2 &= \int_0^\infty [(\gamma - 1) A(y) f(y) g(y)]^2 (T_\infty / T(y))^3 \Lambda(y) dy + \gamma^2 (C_f/2) \int_0^\infty g^2(y) h^2(y) (T_\infty / T(y))^2 \Lambda(y) dy, \\ C_1 &= 2(\gamma - 1) \int_0^\infty A(y) f(y) g^2(y) (T_\infty / T(y))^3 \Lambda(y) dy / A_0^2 \\ C_2 &= \int_0^\infty g^2(y) (T_\infty / T(y))^3 \Lambda(y) dy / A_0^2. \end{aligned}$$

Note that for the adiabatic wall boundary layer, i.e., $\Delta T = 0$, equation (3.14) reduces to the experimentally-proven scaling relation, $\text{OPD}_{rms} \sim \rho_\infty \delta \sqrt{C_f} M_\infty^2$ (Gordeyev et al 2012, 2014).

From equation (3.14), OPD_{rms}^2 is a quadratic function of ΔT and reaches a minimum at

$$\frac{\Delta T_{\min}}{T_{\infty} M_{\infty}^2} = -\frac{C_1}{2C_2} = -\frac{(\gamma-1) \int_0^{\infty} A(y) f(y) g^2(y) (T_{\infty}/T(y))^3 \Lambda(y) dy}{\int_0^{\infty} g^2(y) (T_{\infty}/T(y))^3 \Lambda(y) dy} \quad (3.15)$$

with a value of

$$\frac{OPD_{rms}^2(\Delta T_{\min})}{OPD_{rms}^2(\Delta T = 0)} = \frac{\int_0^{\infty} \left(g^2(y) \cdot (T_{\infty}/T(y)) \left[A(y)(\gamma-1)M_{\infty}^2 f(y) - \frac{\Delta T_{\min}}{T_{\infty}} \right]^2 + \gamma^2 (C_f/2) h^2(y) \right) (T_{\infty}/T(y))^2 \Lambda(y) dy}{A_0^2} \quad (3.16)$$

For positive ΔT , equation (3.14) can be rearranged in the following manner,

$$OPD_{rms} = A_0 K_{GD} \rho_{\infty} \delta \sqrt{C_f} \left(M_{\infty}^2 + D_1 \frac{\Delta T}{T_{\infty}} \right) \left[1 + \frac{D_2}{2} \left(\frac{\Delta T/T_{\infty}}{M_{\infty}^2 + D_1 \Delta T/T_{\infty}} \right)^2 + H.O.T. \right] \quad (3.17)$$

where $D_1 = C_1/2$ and $D_2 = C_2 - (C_1/2)^2$. For positive temperature differences, the second term in the square brackets in equation (3.17) will be shown to be much smaller than unity and equation (3.17) can be further simplified as,

$$OPD_{rms} = A_0 K_{GD} \rho_{\infty} \delta \sqrt{C_f} \left(M_{\infty}^2 + D_1 \frac{\Delta T}{T_{\infty}} \right), \quad \Delta T > 0 \quad (3.18)$$

Several important conclusions can be drawn from analyzing the model predictions:

1. Cooling the wall to ΔT_{\min} should significantly reduce the aero-optical distortions.
2. Amount of cooling, ΔT_{\min} , is proportional to a square of the freestream Mach number.
3. $\Delta T_{\min}/(T_{\infty} M_{\infty}^2)$ primarily depends on the choice of $A(y)$.
4. Finally, heating the wall will increase the aero-optical distortions.

In summary, the model provides testable predictions about choices for $A(y)$ and $\Lambda(y)$, and comparing experimental results to the model predictions should provide the evidence to support (albeit indirectly) a particular choice of both $A(y)$ and Λ .

3.2.1 Cooled Wall Results

In the previous AFOSR-funded investigation, effects of the wall heating were primarily investigated, with only few experimental points for a cooled wall. In this work the cooling effects were thoroughly documented and presented below.

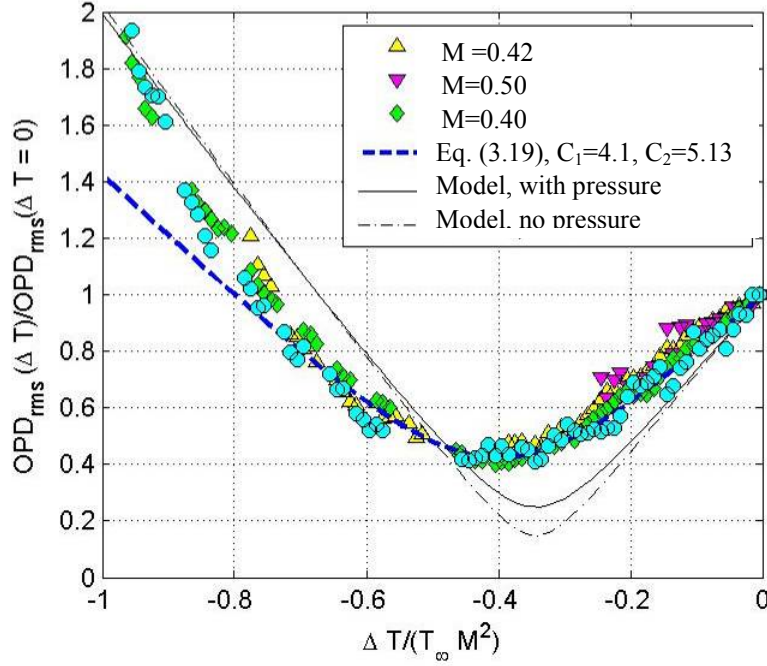


Figure 3.2. OPD_{rms} normalized by the OPD_{rms} value with $\Delta T = 0$ versus $\Delta T / (T_{\infty} M_{\infty}^2)$, the best-fit using equation (3.19) and the model predictions, equation (3.14), using $\Lambda_1(y)$ and $A(y)$ with and without the pressure term.

For negative temperature differences, the full scaling relationship, equation (3.14) should be used. Factoring out M_{∞}^2 from the right hand side of equation (3.14) gives the normalized OPD_{rms} expression,

$$\frac{OPD_{rms}(\Delta T)}{OPD_{rms}(\Delta T = 0)} = \left[1 + C_1 \frac{\Delta T}{(T_{\infty} M_{\infty}^2)} + C_2 \left(\frac{\Delta T}{(T_{\infty} M_{\infty}^2)} \right)^2 \right]^{\frac{1}{2}}. \quad (3.19)$$

As discussed earlier, for negative temperature differences, aero-optical distortions should be at their minimum. The normalized OPD_{rms} data for three Mach numbers are plotted versus $\Delta T / (T_{\infty} M_{\infty}^2)$ in Figure 3.2 and the strong effect of the difference between the wall and adiabatic wall temperature is apparent in this figure. All experimental results successfully collapse onto one curve and the minimum of approximately 0.4 in the normalized OPD_{rms} value is clearly observed around $\Delta T / (T_{\infty} M_{\infty}^2) = -0.4$. In other words, the optical aberrations in the turbulent boundary layer were decreased by 60% at this temperature difference. This is a dramatic decrease in the magnitude of optical aberrations and it provides a promising passive way to significantly reduce aero-optical distortions caused by turbulent boundary layers. The results also confirm the model prediction that the modest wall cooling reduces OPD_{rms} . Performing a least-square fit, the constants C_1 and C_2 were found to be 4.1 and 5.13, respectively. equation (3.19) with these constants is plotted in Figure 3.2, showing a fairly good prediction of the normalized OPD_{rms} -values for the range of $\Delta T / (T_{\infty} M_{\infty}^2)$ between zero and -0.7; below -0.7 experimental results are higher than equation (3.19) predicts, indicating a possible departure from some of the assumptions used in deriving the model. The value of C_1 agrees within experimental error with the one

obtained from the heated-wall experiment. Also, the second term in equation (3.17) is always less than $D_2 / (2D_1^2) = 0.03$, verifying the assumption made in deriving equation (3.18).

The model requires the knowledge of the velocity profile, equations (3.10) and (3.11), the pressure fluctuation profile, equation (3.12), the function $A(y)$, defined in equation (3.6), and the density correlation length, $\Lambda(y)$. The mean velocity profile was measured using the hot-wire at $M_\infty = 0.4$, while the fluctuation velocity and pressure profiles are taken from the DNS simulations, Guarini et al (2000). Three different choices of the density correlation lengths, shown in Figure 2.21, were used. For the A -function, three choices are tested: $A(y) = r$, $A(y) = 1$ and $A(y)$, taken from Smits & Dussauge (1996).

Table 3.1. Various parameters predicted by the model.

$A(y)$	$\Lambda(y)$	A_0	C_1	C_2	$\frac{\Delta T_{\min}}{T_\infty M_\infty^2}$	$\frac{OPD_{rms}(\Delta T_{\min})}{OPD_{rms}(\Delta T = 0)}$	$\frac{OPD_{rms}(\Delta T_{\min})}{OPD_{rms}(\Delta T = 0)}, h = 0$
$= r$	Λ_1	0.17	6.41	10.99	-0.29	0.25	0.10
$= r$	Λ_2	0.15	6.84	12.69	-0.27	0.27	0.14
$= r$	Λ_3	0.13	6.59	11.73	-0.28	0.27	0.12
$= 1$	Λ_1	0.19	5.77	8.80	-0.33	0.23	0.10
$= 1$	Λ_2	0.17	6.17	10.18	-0.30	0.27	0.14
$= 1$	Λ_3	0.15	5.94	9.41	-0.32	0.25	0.12
$A(y)$	Λ_1	0.20	5.46	7.92	-0.34	0.25	0.14
$A(y)$	Λ_2	0.18	5.91	9.44	-0.31	0.27	0.17
$A(y)$	Λ_3	0.15	5.63	8.54	-0.33	0.27	0.17

Table 3.1 presents values of A_0 , C_1 , C_2 , $\Delta T_{\min} / (T_\infty M_\infty^2)$ and $OPD_{rms}(\Delta T_{\min}) / OPD_{rms}(\Delta T = 0)$, predicted by the model for different selected $A(y)$ and $\Lambda(y)$. Using results from Table 3.1, the closest prediction of the experimentally-measured values of C_1 , C_2 , the location and the value of the minimum OPD_{rms} is given with Λ_1 or Λ_3 and $A(y)$. Theoretical predictions with and without the pressure term are also shown in Figure 3.2. The theoretical model predicts the location of the minimum OPD_{rms} for $\Delta T_{\min} / (T_\infty M_\infty^2) = -0.34$, which is within 15% of the experimentally-observed value. The theoretical model underpredicts the minimum value of OPD_{rms} by 30%. One possible source for this discrepancy is that in deriving the model, the cross-term $\langle T' p' \rangle$ was not included. However, this term is not negligible, as the temperature fluctuations are partially due to the total temperature fluctuations (Debieve et al 1997; Guarini et al 2000), which are, in turn, the consequence of the pressure fluctuations. So the inclusion of the cross-term would most probably increase the level of density fluctuations and would result in higher values of OPD_{rms} .

The model supports the choice of $A(y)$, as all other choices lead to even smaller values of $\Delta T_{\min} / (T_\infty M_\infty^2)$, see Table 3.1. Notice that the choice of Λ does not significantly affect $\Delta T_{\min} / (T_\infty M_\infty^2)$.

Figure 3.2 also shows the importance of including the pressure term into the model, as without it the model predicts a much lower value of 0.17 for $OPD_{rms}(\Delta T_{\min}) / OPD_{rms}(\Delta T = 0)$.

Notice that the inclusion of the pressure term is important only in the temperature range of the lowest OPD_{rms} and does not significantly alter OPD_{rms} for the canonical adiabatic-wall boundary layer. As discussed earlier, it is generally accepted that in adiabatic-wall boundary layers the temperature fluctuations are several times larger than the pressure fluctuations, so the pressure fluctuations can be neglected. But from the presented model, equation (3.7), it follows that in the moderately-cooled boundary layers the temperature fluctuations are suppressed, while the pressure fluctuations, which are related to velocity fluctuations, are not significantly modified. Thus, the cooled-wall boundary layer might be a better suitable flow to study the pressure fluctuations inside the boundary layer.

A final comment about the pressure term in the model is that its relative importance is proportional to C_f , see equation (3.16), and it would be even more important at low Reynolds numbers.

As mentioned before, the only other model for including temperature effects to predict aero-optical distortions of a boundary-layer is the model proposed in Wyckham & Smits (2009). From their model it follows that optical aberrations are inversely related to the wall temperature; their model predicts that the value of OPD_{rms} will *decrease* as the wall temperature is *increased*. Clearly, the presented experimental data pointedly contradicts this result. A close inspection shows that the model from Wyckham & Smits (2009) is based upon the SRA, not the “extended” SRA, and assumes that total enthalpy is constant throughout the boundary layer, and therefore does not allow the total temperature to vary.

3.2.2 Convective speeds

The presented model, equation (3.13), estimates the boundary-layer density profile for different wall temperatures. One can make a plausible assumption that the density structure convects at the local velocity and the observed overall convective speed of the aero-optical structure is related to the velocity integral weighted by the density field. So, we can speculate that the measured convective speed of aero-optical structures can be presented as,

$$\frac{U_c}{U_\infty} = \frac{\int |\rho_{rms}(y, \Delta T)| f(y/\delta) dy}{\int |\rho_{rms}(y, \Delta T)| dy} \quad (3.20)$$

It is worth noting that the similar approach was used to correctly predict the experimentally-observed increase in the convective speed of aero-optical structures in a boundary layer at supersonic speeds, Gordeyev et al (2012), Gordeyev et al (2015). The model prediction, equation (3.20), with $A(y)$, is plotted in Figure 3.3 as a function of the wall temperature, along with experimental measurements of the convective speeds. While the particular choice of the integral in equation (3.20) is admittedly somewhat ad hoc, the model properly predicts all the experimentally-observed trends, including the reduction of the convective speed for large negative $\Delta T / (T_\infty M_\infty^2) < -0.5$ and even absolute values of the convective speed for the adiabatic wall boundary layer. From the model one can see that for large negative temperature differences, the mean temperature profile near the wall, equation (3.9), was modified, compared to the adiabatic wall case. This led to the increase of the density fluctuations near the wall, while in the outer part of the boundary layer the density fluctuations were still suppressed. Therefore, the slower-moving structures near the wall were optically “amplified”, leading to the decrease in the overall convective speed of aero-optical structure. The model prediction without the inclusion of the pressure term is also shown in Figure 3.3 and shows a lesser agreement with the data. Thus, it also

indicates that the pressure term has to be included to study density fluctuations in moderately-cooled boundary layers.

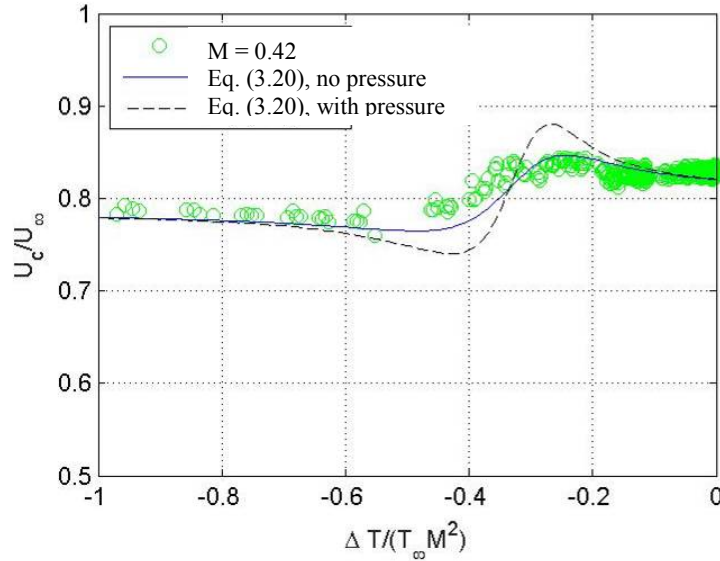


Figure 3.3. Convective velocity of aero-optic aberrations for full wall cooling as a function of wall temperature and comparison with the theoretical predictions.

3.3 Extension to supersonic speeds

The model reasonably predicts all the important aero-optical characteristics of non-adiabatic-wall subsonic boundary layers; it also correctly predicts OPD_{rms} for supersonic adiabatic boundary layers, Gordeyev et al (2012). Because the density correlation lengths (Gao et al, 2013), and normalized pressure variations (Duan & Choudhari, 2013), are similar for subsonic and supersonic speeds, the model predictions can be extended to the supersonic non-adiabatic regime. Results of the predicted levels of OPD_{rms} at different Mach numbers and temperature differences, *adjusted to match experimental results at subsonic speeds* are shown in Figure 3.4. At supersonic speeds, the OPD_{rms} -level becomes a non-linear function of the wall temperature for the heated boundary layer and the relative increase in OPD_{rms} becomes less pronounced for Mach numbers larger than one. OPD_{rms} still has a minimum value around $\Delta T / (T_\infty M_\infty^2) = -0.4$ for all Mach numbers; also the relative reduction in OPD_{rms} is similar for both subsonic and supersonic boundary layers. Note that for $M_\infty = 2.0$ and $M_\infty = 3.0$ the lines in Figure 10 do not extend to large negative temperatures because the wall temperature eventually reaches the absolute zero and cannot be cooled further.

Overall, the wall cooling still should be an effective way to reduce aero-optical distortions of the boundary layer at low supersonic speeds, $M_\infty < 3$. The optimal cooling is expected to be around $\Delta T / (T_\infty M_\infty^2) = -0.4$ with the reduction in OPD_{rms} by a factor of two or so.

3.4 Results for Partial Wall Cooling

The predictions from the model raise the possibility of using wall cooling as a method for aero-optic mitigation. In practical applications where this is of potential use, however, the energy expense of cooling of the full TBL development length in an airborne application might be impractical (Cress, 2010). One alternate means of applying wall cooling flow control might be to

apply cooling over only partial lengths of the TBL development length upstream of the optical aperture.

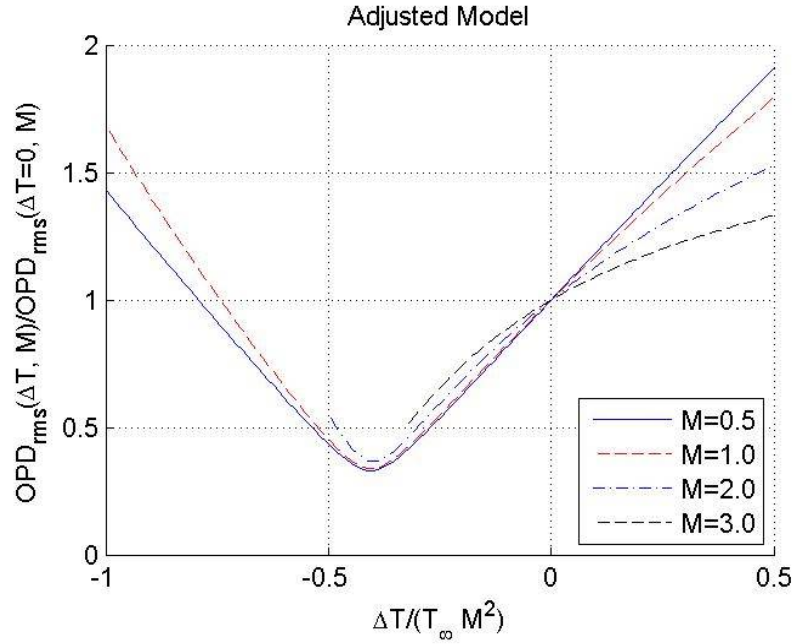


Figure 3.4. Adjusted model predictions (with Λ_1 and $A(y)$) at subsonic and supersonic speeds.

In addition to the full wall cooling case, several different types of partial wall cooling configurations were evaluated using the Malley probe wavefront sensor. A set of near-aperture partial wall-cooling wavefront measurements were obtained, in which the cooling end location x_1 was fixed just upstream of the optical measurement section at $x = 120$ cm, and the location where cooling began, x_0 , was varied in order to change the length of cooling, $L_{cool} = x_1 - x_0$. The second category of partial wall-cooling tests was a set of wavefront measurements for far-upstream cooling, in which x_0 was fixed, and x_1 was varied in order to change the cooling length. The full list of the wall-cooling cases tested in this experiment is given in Table 3.2 along with the streamwise locations of the start, x_0 , and end, x_1 , of the cooled wall segments. The ratio of L_{cool} to the TBL development length to the Malley probe location, $R_{cool} = L_{cool}/x_{MP}$, are also given in Table 3.2.

Table 3.2. Parameters for full and partial wall cooling cases.

Sections Cooled	Case Description	M_∞	$\frac{L_{COOL}}{L_{DEV}}$
1, 2, 3	Full Wall Cooling	0.4.. 0.5	96%
1	Far-Upstream (Short)	0.35.. 0.4	32%
2	Upstream Strip (Short)	0.35.. 0.4	32%
3	Near-Aperture (Short)	0.35.. 0.4	32%
1, 2	Far-Upstream (Long)	0.4	64%
2, 3	Near-Aperture (Long)	0.35.. 0.4	64%

OPD_{rms} was computed from partial wall cooling wavefront measurements in the same manner as for full wall cooling; the results are presented in Figure 3.5 along with the $M = 0.4$, full wall cooling OPD_{rms} data for comparison. The results for the three longer partial wall cooling configurations, where $R_{cool} = 64\%$, are shown in Figure 3.5a. For the far-upstream 64% cooling configuration, the minimum value of OPD_{rms} was about $0.53 OPD_{rms}(\Delta T = 0)$, and value of $\Delta T_{Optimal}$ was approximately $-0.47 T_{\infty} M^2$. For the same length of wall cooling near the aperture, the optimal wall temperature was found to be about $-0.40 T_{\infty} M^2$, and effectiveness for aero-optic mitigation is slightly better than for the far-upstream cooling, at $0.45 OPD_{rms}(\Delta T = 0)$. The optimal cooling temperature for the far-upstream cooling case was about 20% lower than the value found for full wall cooling; however for near aperture cooling $\Delta T_{Optimal}$ was not altered significantly. Recall from the description in Table 3.2 that the third partial wall cooling configuration was a hybrid of short near-aperture and far-upstream cooling, each with $R_{cool} = 32\%$. Combined, this results in a total non-contiguous cooling area, R_{cool} , equal to 64% of the total TBL development length. The near/far combined configuration yielded an optimal cooling temperature estimated to be in the neighborhood of $\Delta T_{Optimal} = -0.40 T_{\infty} M^2$ (although wavefront data was not obtained for $\Delta T/(T_{\infty} M^2) = -0.5$ to -0.3). For the whole range of wall temperatures measured for this case, OPD_{rms} is slightly higher compared to the full wall cooling case.

Data for shorter lengths of wall cooling are presented in Figure 3.5b for three additional partial wall configurations: near-aperture cooling, far-upstream cooling, and ‘mid-range’ cooling, in which the middle one-third of the wall in the middle of the TBL development test section was cooled. For the short length of far-upstream cooling, $\Delta T_{Optimal}$ was found to be $-0.53 T_{\infty} M^2$, and OPD_{rms} was only reduced by approximately 28% at this temperature. For the short length of near aperture partial cooling, $\Delta T_{Optimal}$ was about $-0.38 T_{\infty} M^2$, where aero-optic aberrations were only reduced by about 23%. These data show that the aero-optic mitigation performance is slightly better for the near-aperture configuration than the far-upstream case of the same length, but the differences are not very large. Cooling a strip of the wall in the middle of the TBL development section (i.e. mid-range strip cooling), resulted in a shift in $\Delta T_{Optimal}$ to a lower temperature ($\approx -0.5 T_{\infty} M^2$) than was found for full wall cooling. However, this configuration was found to result in a slightly larger reduction in OPD_{rms} (about a 44% decrease) than either of the other short length cooling configurations.

While OPD_{rms} measured for a variety of different partial wall cooling configurations possessed a functional form similar to the one that has been both observed and predicted for full wall cooling, changes in optimal temperature value and OPD_{rms} reduction were found to be highly dependent on the partial wall cooling configuration. It was shown before that both the optimal temperature value and the amount of aero-optic mitigation are a function of the model constants C_1 and C_2 . Therefore, it is likely that an effective means of modifying the model for partial wall cooling is to change the model constant definitions so that they are functionally dependent on the length and location of wall cooling.

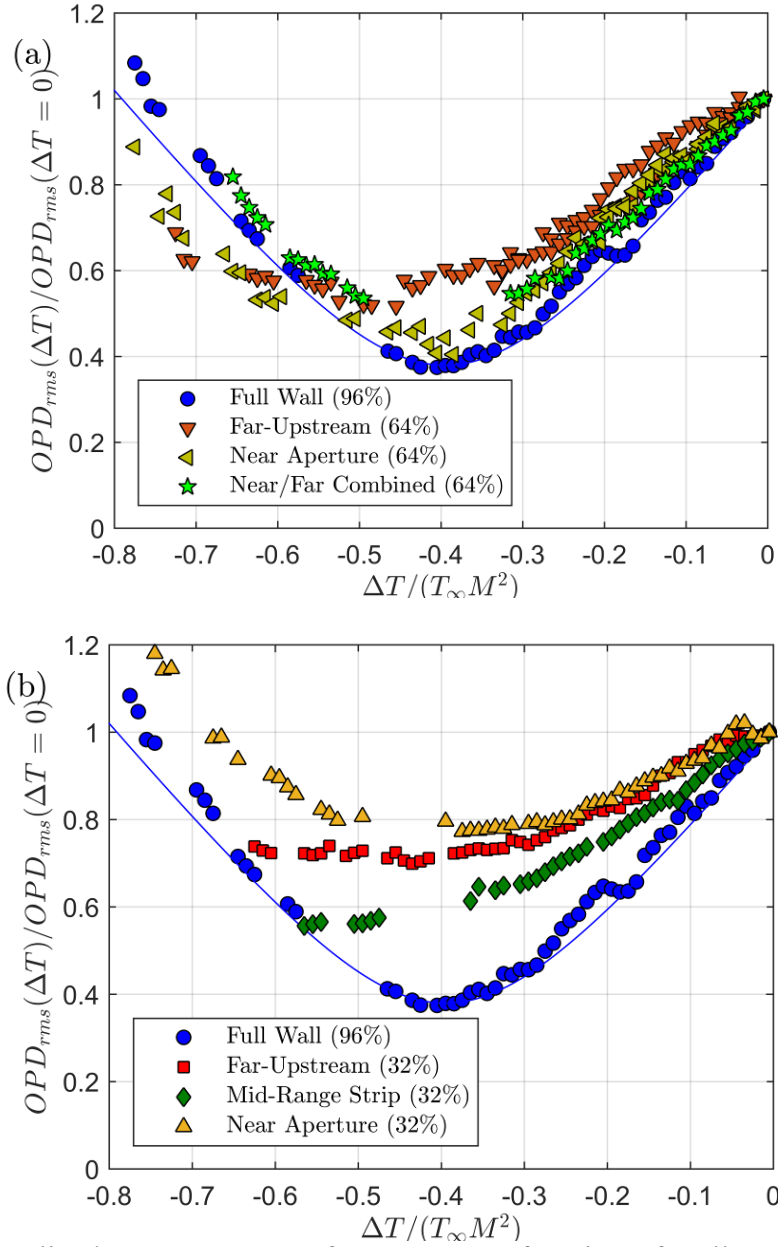


Figure 3.5. Normalized measurements of OPD_{rms} as a function of wall temperature $\Delta T/(T_\infty M^2)$ for partial wall cooling cases: a) long lengths of cooling (64%) and b) shorter lengths of cooling (32%).

Convection velocity was also computed from wavefront measurements, and the results for the shortest strips ($R_{cool} = 32\%$) for both near aperture and far-upstream cooling are plotted in Figure 3.6. The results of measured U_C from full-wall cooling measurements (from Figure 3.3) are also shown for comparison. For far-upstream wall cooling, the convection velocity is reduced below the value of $0.83U_\infty$ measured for adiabatic wall TBLs, with U_C decreasing monotonically with wall temperature to about $0.73U_\infty$ at $\Delta T = -0.8T_\infty M^2$. Variation in U_C with wall temperature was also found in full wall cooling wavefront measurements, however for far-upstream partial wall cooling the measured values of U_C showed were consistently lower than those found for full-

wall cooling. For near-aperture cooling, convective velocity is actually increased over the value of $0.83U_\infty$ measured for adiabatic wall TBLs. As wall temperature was decreased to around $-0.45T_\infty M^2$, U_C increased to a maximum value of about $0.88U_\infty$, and as temperature was decreased further, U_C was found to decrease, reaching a value of about $0.78U_\infty$ around $\Delta T = -0.75T_\infty M^2$.

In Figure 3.6, it is clear that the functional dependence of U_C on ΔT for partial wall cooling temperature is distinctly different than the functional dependence measured for full wall cooling. Measured values of U_C for near aperture partial wall cooling were found to be generally greater than for full wall cooling, while U_C measured for far-upstream cooling was generally less than the full wall cooling results. One possible explanation for these differences was discussed in Chapter 4, namely that step changes in wall temperature create distinct thermal sub-layers within the turbulent boundary layer. Assuming that this is the case, far-upstream cooling could generate a thermal sub-layer that would affect density fluctuations in the outer part of the turbulent boundary layer. Conversely, a thermal sub-layer generated by near aperture cooling would tend to affect density near to the wall, reducing the aero-optic signature of this region. The experimentally observed effect on U_C is consistent with this hypothesis.

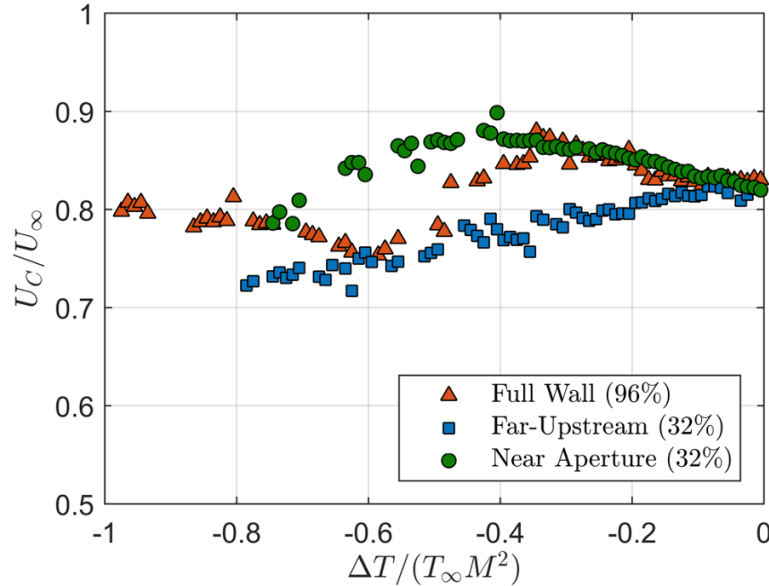


Figure 3.6. Convective velocity computed from partial wall cooling wavefront measurements.

3.5 Partial Wall Cooling Model

Based on characteristics observed in partial wall heating/cooling literature and in convective velocity measurements from different partial wall cooling cases, it is reasonable to assume that the variation in the effect of the length and location of wall cooling on aero-optic aberrations is caused by the differences between thermal sub-layers generated by each unique configuration. Since the model constants C_1 and C_2 account for the effect of wall-temperature in the TBL aero-optic model, equation (3.14), it was assumed that these empirical constants would retain the functional form found in equation (3.14) for partial wall cooling, but with C_1 and C_2 being dependent on the start location, x_0 , and end location x_1 , of wall cooling:

$$OPD_{rms}^{NORM}(\Delta T) = \left[1 + C_1(x_0, x_1) \left(\frac{\Delta T}{T_\infty M_\infty^2} \right) + C_2(x_0, x_1) \left(\frac{\Delta T}{T_\infty M_\infty^2} \right)^2 \right]^{\frac{1}{2}}. \quad (3.21)$$

This notion is supported by the general characteristics of $OPD_{rms}(\Delta T)$ observed in experiments for a variety of different partial wall cooling configurations, as shown in Figure 3.5.

Table 3.3 Empirical constants computed for full and partial wall cooling experiments

Configuration	R_{cool}	C_1	C_2	$\frac{\Delta T_{Optimal}}{T_\infty M_\infty^2}$	$\frac{OPD_{rms}(\Delta T_{min})}{OPD_{rms}(\Delta T = 0)}$
Full Wall	96%	4.42	5.71	-0.39	0.38
Far-Upstream (Short)	32%	2.09	2.18	-0.48	0.71
Far-Upstream (Long)	64%	3.07	3.32	-0.46	0.54
Near Aperture (Short)	32%	2.43	3.67	-0.33	0.77
Near Aperture (Long)	64%	3.95	4.94	-0.40	0.46
Mid-Range (Short)	32%	2.74	2.74	-0.50	0.56
Near/Far Combined	64%*	3.97	5.29	-0.38	0.51

*Length of cooling is not continuous.

To empirically determine the values of C_1 and C_2 that corresponded to each partial wall cooling case from experiments, equation (3.21) was fit to the results of each experiment over the range $-0.7 < \Delta T / (T_\infty M_\infty^2) < 0$, and the results are presented in Table 3.3 along with the values of $\Delta T_{Optimal} / (T_\infty M_\infty^2)$ and $OPD_{rms}(\Delta T_{Optimal}) / OPD_{rms}(\Delta T = 0)$ computed from the empirically determined C_1 and C_2 . For increasing values of R_{cool} , the experimentally determined values of both constants also monotonically increased towards the values obtained for full wall cooling wavefront measurements. The values of C_1 and C_2 calculated for far-upstream cooling were lower than those found for all other configurations. Out of all the configurations where $R_{cool} = 32\%$, the mid-range case (where Section 2 only was cooled) resulted in the largest aero-optic mitigation. For cases where $R_{cool} = 64\%$, the near-aperture cooling case gave the biggest reduction in OPD_{rms} .

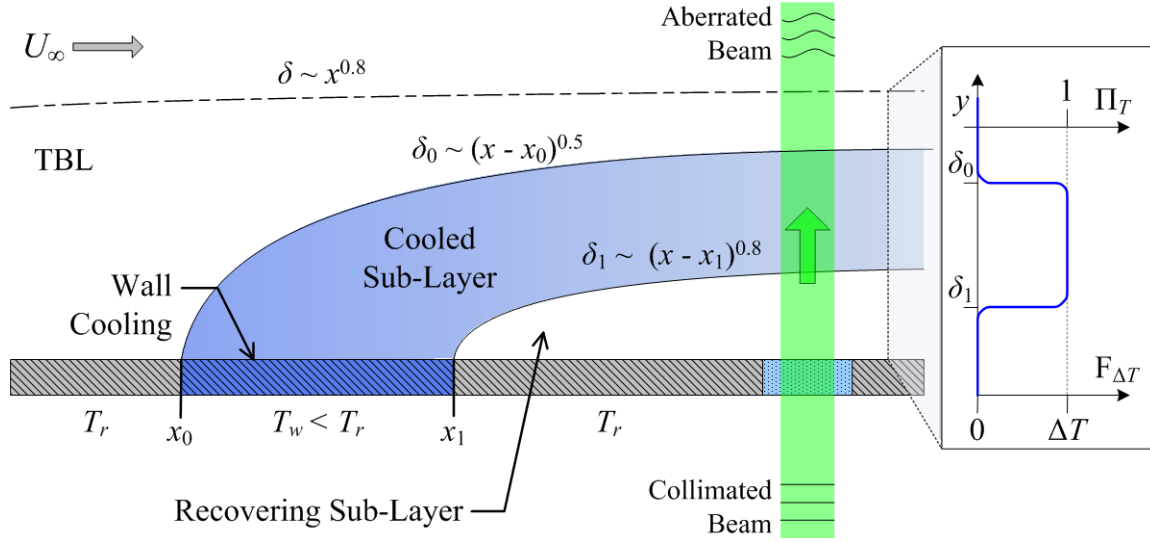


Figure 3.7. Schematic of a simple thermal sub-layer used for modeling the effects of partial wall cooling on wavefront aberrations in the TBL.

Previous characterizations of thermal sub-layers caused by step changes in wall temperature (Gran, et al., 1974; Antonia, et al., 1977) were used to inform the modification of the existing wall cooling model for the effect of partial wall cooling. To simulate the effect of thermal sub-layer on boundary layer aero-optic statistics, the scalar ΔT in equation (3.7) was replaced with an arbitrary temperature difference function $F_{\Delta T}$, which is a function of y and the upper and lower bounds of the thermal sub-layer, δ_0 and δ_1 :

$$\left(\frac{T_{rms}(y)}{T_\infty} \right)^2 = \left(\frac{u_{rms}(y)}{U_\infty} \right)^2 \left[\frac{F_{\Delta T}(\delta_0, \delta_1, y)}{T_\infty} + r(\gamma - 1) M_\infty^2 \frac{U(y)}{U_\infty} \right]^2. \quad (3.22)$$

Comparing equation (3.22) to (3.7) it becomes clear that $F_{\Delta T}(\delta_0, \delta_1, y)$ can be thought of as the effective value of ΔT at any point y in the TBL profile for a given wall cooling configuration. It follows then that $F_{\Delta T}$ can be written as the product of the wall temperature difference ΔT and a configuration-specific sub-layer mask function, $\Pi_T(\delta_0, \delta_1, y)$: $F_{\Delta T}(\delta_0, \delta_1, y) = \Delta T \times \Pi_T(\delta_0, \delta_1, y)$. Note that Π_T is bounded between 0 and 1 and has the same functional form as $F_{\Delta T}$ (see inset of Figure 3.7). Substituting this relation into (3.22), the temperature-velocity relationship for partial wall cooling becomes

$$\left(\frac{T_{rms}(\delta_0, \delta_1, y)}{T_\infty} \right)^2 = \left(\frac{u_{rms}(y)}{U_\infty} \right)^2 \left[\frac{\Delta T \times \Pi_T(\delta_0, \delta_1, y)}{T_\infty} + r(\gamma - 1) M_\infty^2 \frac{U(y)}{U_\infty} \right]^2. \quad (3.23)$$

In effect, the addition of a mask function to the model limits the application of the ESRA temperature-velocity relation to the region of the TBL within the thermal sub-layer; outside of the sub-layer, where $\Pi_T = 0$, equation (3.23) reduces to the SRA.

This temperature-velocity relation was combined with equation (3.8) to find that

$$\left(\frac{\rho_{rms}(\delta_0, \delta_1, y)}{\rho_\infty}\right)^2 = \left(\frac{u_{rms}(y)}{U_\infty}\right)^2 \left(\frac{T_\infty}{T(y)}\right)^4 \left[\frac{\Delta T \times \Pi_T(\delta_0, \delta_1, y)}{T_\infty} + r(\gamma - 1) M_\infty^2 \frac{U(y)}{U_\infty} \right]^2 + \left(\frac{P_{rms}(y)}{P_\infty}\right)^2 \left(\frac{T_\infty}{T(y)}\right)^2, \quad (3.24)$$

where $T(y)/T_\infty$ is given in equation(8a). Equation (3.24) was then integrated using Sutton's linking equation (1.2) to calculate OPD_{rms} . The resulting aero-optic model equation reduces to the same functional form found in equation (3.14) with the sub-layer mask function being grouped into the integrals for C_1 and C_2 :

$$C_1(x_0, x_1) = \frac{2(\gamma - 1)}{A_0^2} \int_0^\infty \Pi_T(y, \delta_0, \delta_1) A(y) f(y) g^2(y) \left(\frac{T_\infty}{T(y)}\right)^3 \Lambda(y) dy \quad (3.25a)$$

$$C_2(x_0, x_1) = \frac{1}{A_0^2} \int_0^\infty \Pi_T^2(y, \delta_0, \delta_1) g^2(y) \left(\frac{T_\infty}{T(y)}\right)^3 \Lambda(y) dy \quad (3.25b)$$

where δ_0 and δ_1 are functions of x_0 and x_1 , respectively.

A piecewise step function was used to define the sub-layer mask function:

$$\Pi_T(y, \delta_0, \delta_1) = \begin{cases} 0, & \text{if } y < \delta_1, \\ 1, & \text{if } \delta_1 \leq y \leq \delta_0, \\ 0, & \text{if } y > \delta_0. \end{cases} \quad (3.26)$$

The thermal sub-layer limits δ_0 and δ_1 were calculated at the Malley probe measurement location, x_{MP} , using the following approximations:

$$\delta_0 = \delta(x_{MP}) \left(\frac{x_{MP} - x_0}{x_{MP}} \right)^{0.5}, \quad (3.27)$$

$$\delta_1 = \delta(x_{MP}) \left(\frac{x_{MP} - x_1}{x_{MP}} \right)^{0.8}.$$

These growth rates for these internal sub-layer boundaries were estimated from the results of prior investigations of thermal step changes in the wall boundary conditions presented by Gran, et al. (1974), Antonia, et al., (1977), and others.

It follows from equation (3.21) that the optimal temperature difference $\Delta T_{Optimal}$ at which maximum aero-optic mitigation is achieved for partial wall cooling is computed

$$\frac{\Delta T_{Optimal}(x_0, x_1)}{T_\infty M_\infty^2} = -\frac{1}{2} \frac{C_1(x_0, x_1)}{C_2(x_0, x_1)} \quad (3.28)$$

Subsequently, the value of the baseline normalized OPD_{rms} at the optimal temperature is

$$OPD_{rms}^{NORM}(\Delta T_{Optimal}) = \left[1 - \frac{1}{4} \frac{C_1^2(x_0, x_1)}{C_2(x_0, x_1)} \right]^{1/2}. \quad (3.29)$$

Since using the function of $A(y)$ from Smits & Dussauge (1996) gave model predictions that were closest to experimental results for the full wall cooling model, this term will be used in the partial wall cooling model predictions.

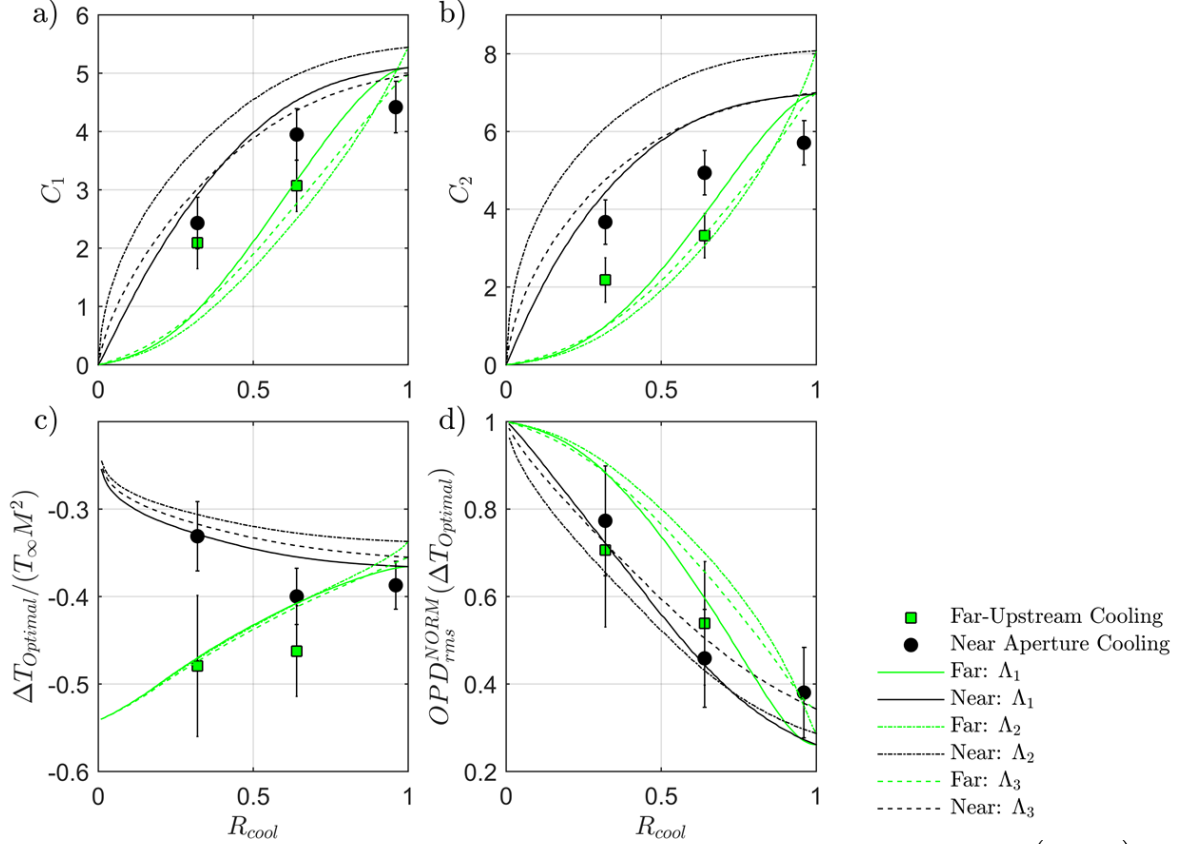


Figure 3.8. Effect of $\Lambda_\rho(y)$ on model predicted constants a) C_1 , b) C_2 , c) $\Delta T_{Optimal}/(T_\infty M^2)$, and d) $OPD_{rms}^{NORM}(\Delta T_{Optimal})$.

The effect of $\Lambda_\rho(y)$ on model predictions of C_1 , C_2 , $\Delta T_{Optimal}/(T_\infty M^2)$, and $OPD_{rms}^{NORM}(\Delta T_{Optimal})$ is shown in Figure 3.8 along with, the values calculated from experimental results. The choice of wall-normal density correlation function, $\Lambda_\rho(y)$, was found to have a strong influence on the shape of the functional dependence of model predictions on R_{cool} . All of the model predictions tended to over-predict the near aperture cooling constants with respect to the experimentally obtained values. The results of the model predictions using Λ_2 over predicted experimental results by as much as 40%, while model predictions using Λ_1 and Λ_3 only gave a 23% over prediction. For the far-upstream case, all three choices for Λ_ρ gave decent model predictions of C_1 and C_2 around $R_{cool} = 0.64$, but significantly under predicts for $R_{cool} < 0.64$, and over predicts for $R_{cool} \approx 1$. For all three choices of density correlation length, the partial wall cooling model gave estimates of $\Delta T_{Optimal}$ or OPD_{rms} that were not in great quantitative agreement with experimental results, but had functional forms that were consistent with trends observed in experiments.

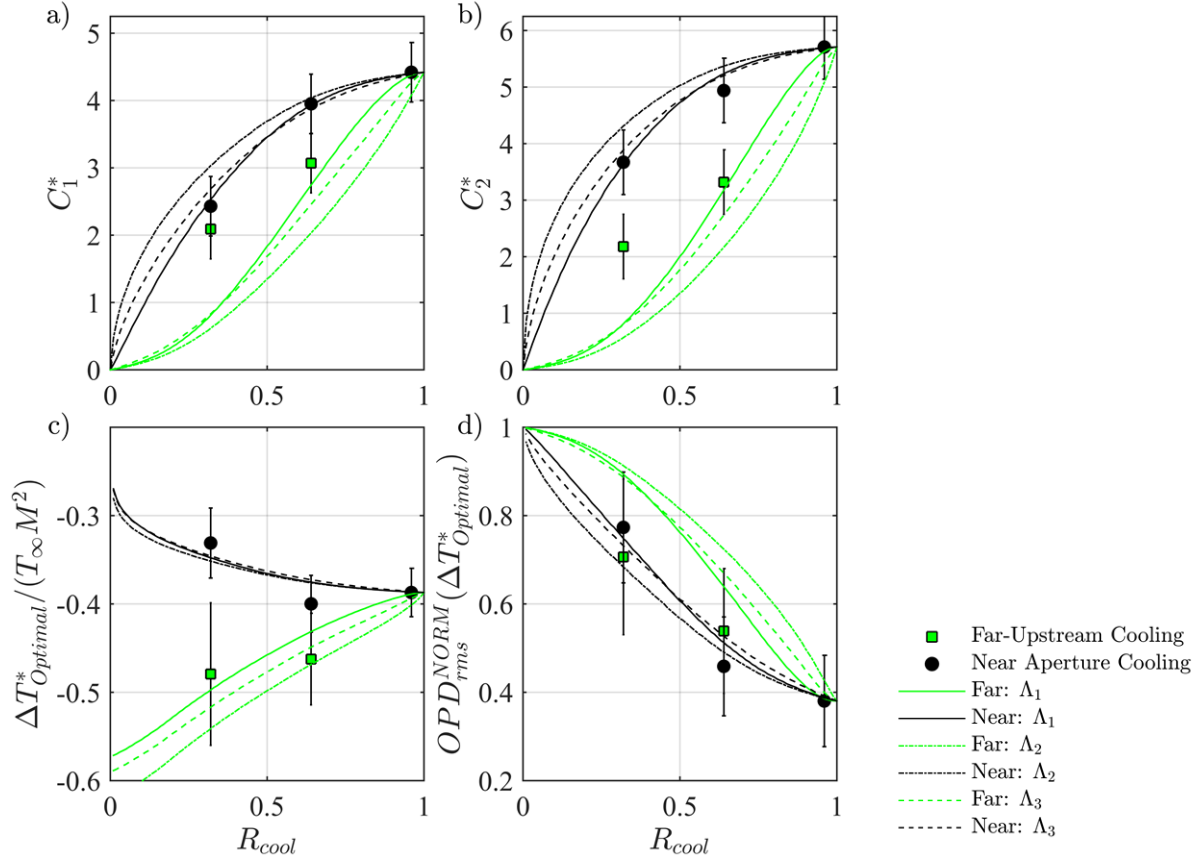


Figure 3.9. Partial wall cooling model predictions for different choices of $\Lambda_p(y)$, scaled to match empirically determined full-wall constants.

It is apparent that the simple analytical model proposed in equation (3.25) does a good job of qualitatively modeling the effect of partial wall cooling on aero-optic characteristics. Quantitatively, however, the model has been shown to be sensitive to different choices for input parameters, and to have generally poor agreement with experimental results. To correct this quantitative discrepancy, the model predicted constants $C_1(x_0, x_1)$ and $C_2(x_0, x_1)$ were scaled so that they are equal to the experimentally obtained values of C_1 and C_2 for the full wall cooling case ($R_{cool} \approx 1$). The results of this scaling are shown in Figure 3.9, for different values of $\Lambda_p(y)$ using the same parameters for the calculations presented in Figure 3.8. The results show that the model predictions for Λ_1 and Λ_3 match experimental data well for near-aperture cooling. For the case of far-upstream cooling, Λ_1 performs the best, but still under-predicts C_1 and C_2 and over-predicts $OPD_{rms}(\Delta T_{Optimal})$ with respect to the experimentally determined values. Despite this discrepancy, the model still does a reasonably good job of predicting the $\Delta T_{Optimal}$ for far-upstream cooling.

This good qualitative agreement, and the prior literature on step changes in wall temperature, indicates that the thermal sub-layer assumption for modeling partial wall cooling is the appropriate approach, but the quantitative disagreement demonstrates that particular methodology used in the present study does not fully capture the physics of all partial wall cooling configurations.

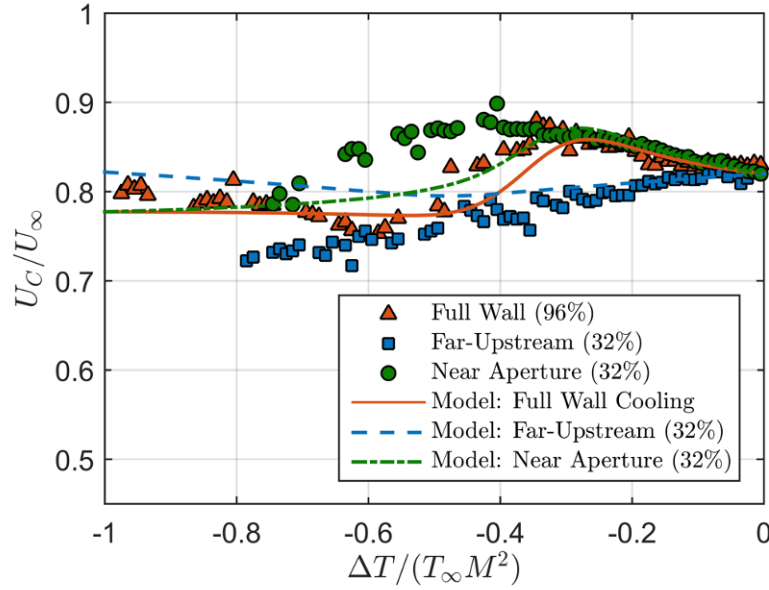


Figure 3.10. Convection velocity of aero-optic aberrations, measured from partial wall cooling experiments and predicted from the model equation (3.30).

Earlier in this chapter, it was shown that equation (3.24) predicts profiles of ρ_{rms} in the non-adiabatic TBL. Similar to equation (3.20), the convective velocity, U_C , of wavefront aberrations in the partially-cooled wall TBLs can be estimated using relation

$$\frac{U_C(\Delta T, x_0, x_1)}{U_\infty} = \frac{\int |\rho_{rms}(y, \Delta T, x_0, x_1)| f(y/\delta) dy}{\int |\rho_{rms}(y, \Delta T, x_0, x_1)| dy} \quad (3.30)$$

The model-predicted dependence of U_C on ΔT was computed from equation (3.30) for the shorter (32%) lengths of wall cooling for which wavefront measured values of U_C were reported in Figure 3.6, and the predictions are compared to experimental data in Figure 3.10. Similarly to other model predictions, the results shown in this figure demonstrate that while the model-predicted values of U_C are in poor quantitative agreement with experimental results, the configuration-dependent trends predicted by the model are very similar to those found experimentally.

3.6 Conclusions and Discussion

The primary objective of this work is to present a theoretical model for the fluctuating density field in adiabatic, cooled and heated boundary layers based on the Extended Strong Reynold Analogy. The fluctuating density field in turn can be used to predict the aero-optical distortions in adiabatic- and non-adiabatic-wall boundary layers. Strictly speaking, the model presented here does not require a perfect anti-correlation between the velocity and the temperature fluctuations but rather simply assumes a functional dependence between them. The experimental data were collected specifically to validate the theoretical model; these data were used to test predictions for heated- and cooled-wall experiments at several subsonic Mach numbers. The wall temperature effect on OPD_{rms} was successfully predicted by the model. For a heated wall the data validated the model's prediction that the level of aero-optical distortion is a linear function of $\Delta T/(T_\infty M_\infty^2)$. For the cooled wall boundary layer, aero-optical distortions initially decrease with a negative

$\Delta T / (T_\infty M_\infty^2)$, reach a minimum value at the optical wall temperature of $\Delta T / (T_\infty M_\infty^2) = -0.4$ and finally increase for larger negative temperature differences; this behavior was also successfully predicted by the model. By assuming different relations between the velocity and the temperature fields and comparing the theoretical predictions with the experimental results, the particular functional dependence between the velocity and the temperature fields was generally supported. In addition, the comparison demonstrated that the pressure term should be included to explain the density fluctuations for the moderately-cooled boundary layers. The model also correctly predicts the variation in the aero-optical convective speed for cooled walls. Finally, the model predictions for different temperature differences were extended to supersonic speeds.

Aero-optical distortions are directly linked to the density structure by the linking equation, equation (1.2), so studying these aero-optical distortions gives many important insights about properties of the density field in boundary layers, which is a hard quantity to measure experimentally. Also, by varying the wall temperature, the temperature field can be modified independently from the pressure field and their respective effects on the density field can be accurately and non-intrusively measured.

The results show that a heat addition or subtraction at the wall in a subsonic, compressible turbulent boundary layer has an important impact on the optical aberration imprinted on the wavefront of a laser propagated through the boundary layer. Particularly, it implies that the aircraft skin upstream of the optical aperture should be kept close to or below the recovery temperature; otherwise, any airborne system which requires optical propagation through the boundary layer will experience larger values of aero-optical distortions. Using cooled walls, aero-optical distortions might be decreased by as much as 60%, providing potentially important practical means to passively mitigate aero-optical effects in boundary layers.

From the deflection angle spectra, it is apparent that for the range of ΔT values tested, a moderate ΔT from the heated wall simply amplifies the density fluctuations in the boundary layer with little or no effect on the velocity statistics of the boundary layer. Further, the amplitude in the deflection angle spectrum varied linearly with the temperature difference. Thus, increasing the wall temperature will not alter the aero-optical structure, but rather will simply amplify it optically, at least in the temperature range tested. These results suggest that low speed flows with very low levels of optical aberrations can be made optically active by introducing a temperature mismatch between the wall and freestream; therefore, optical aberrations that are unobservable at $\Delta T = 0$ can be measured with the same optical wavefront instruments without distorting the relevant structures by simply heating the wall. One consequence of this result is the possibility of using non-intrusive optical diagnostic tools, like a Malley probe or a high-speed wavefront sensor, to study boundary layers in low speed turbulent boundary layer facilities. This result greatly increases the number of turbulent boundary layer facilities that can be used in aero-optic research, as well as allows sensitive optical sensors to be used to study turbulent boundary layers at low subsonic speeds; this has already led to a development of new experimental approaches to study fundamental physics of boundary layers, described in Chapters 4 and 5 of this report.

Experimental investigations of the effect of partial wall cooling have also successfully demonstrated notable aero-optic mitigation capabilities, with OPD_{rms} being reduced by as much as 60% using this flow control scheme. This maximum reduction was achieved for cooling applied over the full wall, and experiments showed that OPD_{rms} monotonically decreases with increasing R_{cool} , meaning that there is no ‘optimal’ *partial* wall cooling configuration. Rather, the greatest reduction of aero-optic aberrations comes from cooling the wall over the full length of the TBL. Results showed, however, that partial cooling can still provide significant reductions in

OPD_{rms} : cooling over 64% of the wall resulted in reductions between 40 – 55%, while cooling over just 32% of the wall reduced OPD_{rms} by about 20 – 40%. Partial cooling results were also highly dependent on the location of the applied cooling, with the largest reductions being achieved for cooling just upstream of the optical aperture over longer lengths of the wall. This result is especially beneficial for the design of any potential wall cooling aero-optic mitigation system where cooling over the full TBL development length is not possible due to space or energy cost constraints.

Wall cooling at supersonic speeds. Results presented in Section 3.3 indicate that the full wall cooling model can be easily extended for supersonic freestream velocities. For partial cooling, Gran, et al. (1974) demonstrated that thermal sub-layer effects are present and similar for partial cooling in supersonic TBLs. Therefore, the partial wall cooling aero-optic model is also expected to extend to the supersonic regime. One limitation of cooling for supersonic TBL aero-optic flow control, however, is found by calculating the value of the optimal cooling temperature.

As it was shown in this work, for full wall cooling, $T_{Optimal} \cong T_{aw} - 0.4T_{\infty}M_{\infty}^2$. Figure 3.11 presents estimates of $T_{Optimal}$ for several different freestream air temperatures that were estimated from the 1976 U. S. Standard Atmosphere. Note that in all cases $T_{Optimal}$ becomes equal to absolute zero (0 K) at about $M_{\infty} = 2.13$, which sets the theoretical maximum speed at which the optimal wall cooling temperature is reachable. Since cooling the wall to 0 K is not feasible in practical applications, however, it is more practical to consider the temperatures of common cryogenic materials, such as liquid Oxygen (LO_2), liquid Nitrogen (LN_2), and liquid Hydrogen (LH_2). Comparing $T_{Optimal}$ to these more realistic estimates of the minimum achievable wall cooling temperature shows that for LH_2 optimal cooling temperatures could be achieved for $M_{\infty} < 2$, and for LO_2 and LN_2 this range of Mach numbers shrinks to approximately $M_{\infty} < 1.6$.

This does not mean, however, that wall cooling would not be an effective means of aero-optic mitigation for supersonic TBLs with $M_{\infty} > 2$. In fact, the aero-optic model predicts that even cooling the wall to temperatures that are greater than $T_{Optimal}$ will result in considerable reductions of aero-optic aberrations. Estimates of the minimum value of OPD_{rms} that can be achieved for wall cooling temperatures greater than a set minimum value (i.e. $T_w \geq T_{Optimal}$) are presented in Figure 3.12 for LO_2 , LN_2 , and LH_2 . The results show that even up to Mach 5, optical aberrations can be reduced by between 40 – 45% for *full* wall cooling to temperatures on the order of 20 – 100 K. It is also expected that for *partial* wall cooling, the amount of aero-optic be further reduced as R_{cool} is decreased, as was shown for subsonic TBLs. While this is somewhat short of the roughly 60% reduction that was measured for the subsonic TBL, it is still a significant improvement. Therefore wall cooling should still be considered as a good candidate for use as an aero-optic mitigation technique in supersonic TBLs.

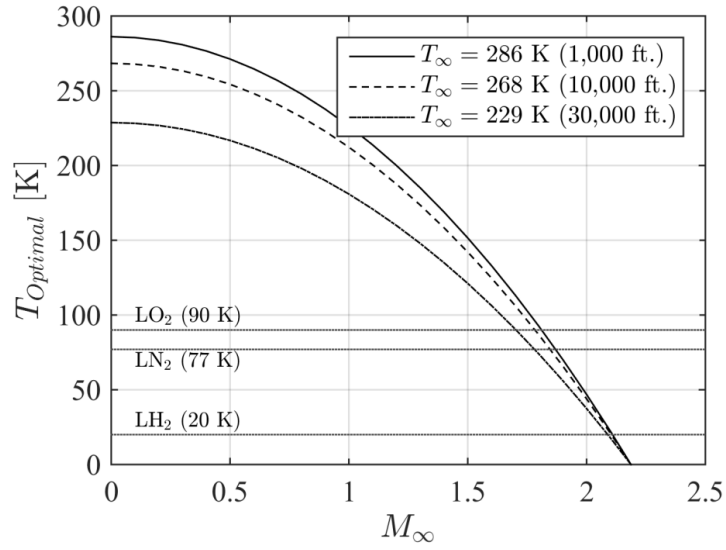


Figure 3.11. Optimal wall cooling temperatures as a function of Mach number using experimentally-obtained model constants, for different altitudes (1976 U. S. Standard Atmosphere).

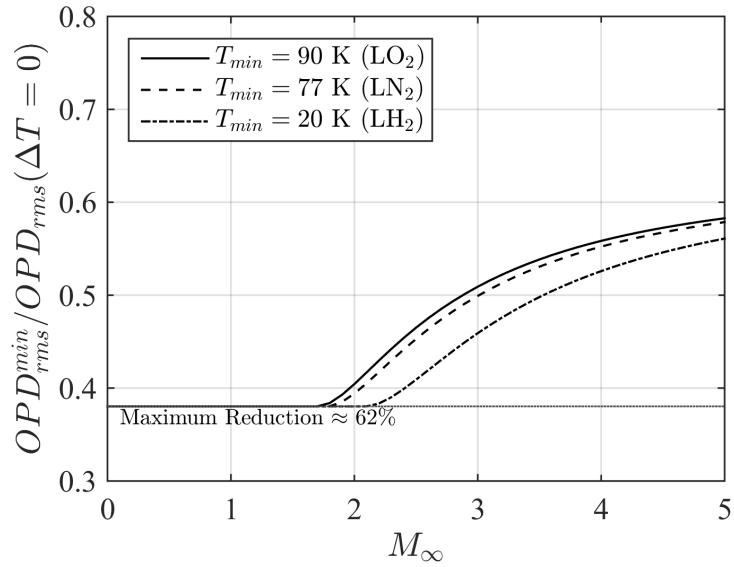


Figure 3.12. Estimates of the minimum value of OPD_{rms} that can be achieved when T_w is constrained so that $T_w \geq T_{Optimal}$, for full wall cooling with $T_\infty = 229$ K (conditions at approximately 30,000 ft.)

4. Aero-Optics of Boundary Layers at Low Reynolds Numbers

4.1 Motivation

As it was discussed in the previous chapter, wall heating acts as a passive amplifier of wavefront distortions. This passive amplification effect can be used advantageously to study low Reynolds number TBLs that have a weak aero-optic signature, such as those with low subsonic freestream velocities and/or TBLs that are very thin. By heating the wall it is possible to a passive ‘marker’ to make low-Reynolds number TBLs aero-optically ‘visible.’ Thus wavefront sensors can be used as non-intrusive diagnostic tools to allow for investigation of the dynamics of turbulent boundary layers at relatively low Reynolds numbers. The heating technique can also provide valuable experimental wavefront information that can be used to verify/correct various scaling models at low Reynolds numbers and to provide a direct comparison with computational simulations, as currently there is a large Reynolds number ‘gap’ between experimental measurements with typical $Re_\theta > 20,000$ (Gordeyev et al, 2014) and numerical simulations (Wang & Wang, 2012; White & Visbal, 2012) with much lower $Re_\theta \sim 1,000$ to 3,000.

4.2 Results

One set of measurements were conducted in the Hessert Transonic Wind Tunnel (TWT) at the University of Notre Dame. The total length to the beginning of the optical section was shortened to approximately 100 cm to reduce the boundary layer thickness, and therefore the Reynolds number. Non-adiabatic wall temperatures were introduced by replacing the Plexiglas wall with an aluminum wall with an 8 mm thick Aluminum plate for the first 100 cm of the test section, and heating it from the outside surface using strips of flexible electric resistive coil heaters. Just downstream of the boundary layer development/wall heating section, portions of the Plexiglas on the upper and lower walls of the wind tunnel were replaced with optical quality glass plates to allow accurate optical characterization of the boundary layer using aero-optic wavefront sensors. A Pitot tube mounted downstream of the optical measurement location was used to measure the free-stream velocity throughout the experiment.

Additional experiments were performed at California Institute of Technology in the Merrill Wind tunnel (MWT), a recirculating tunnel with a $0.6 \times 0.6 \times 2.4$ m constant area test section. The wall of a test plate mounted in the center of the test section was heated at two streamwise locations using the same flexible heating panels as in the Notre Dame experiments, this time sandwiched between the aluminum test surface and a heavily insulated lower surface.

Table 4.1 Boundary Layer Wall Heating Conditions

Facility	V_∞ [m/s]	M	δ [cm]	Re_θ	ΔT [K]	f_{samp} [kHz]
Caltech MWT	9.4	0.03	2.7	1,700	21	30
ND TWT	64.8	0.18	1.2	4,200	15-28	200
"	98.8	0.28	1.2	5,700	9-24	200
"	118	0.35	1.2	7,900	7-28	200
"	140	0.41	1.2	9,000	7-24	200
"	140	0.41	2.4	20,000	0	200

Wavefront measurements were acquired downstream of the heated wall boundary layer development section in both facilities using the Malley Probe 1-D wavefront sensor. The Mach

number M , boundary layer thickness δ , Reynolds number Re_θ , wall temperature ΔT , and sampling rate f_{samp} , corresponding to each of these cases are given in Table 4.1. From the deflection angle time series measured with the Malley probe, deflection angle amplitude spectra and OPD_{rms} were computed.

Figure 4.1 presents normalized deflection angle spectra obtained using wall heating as a passive amplifier for the different Reynolds numbers spanning an order of magnitude, from $Re_\theta = 1,700$ to $20,000$. In the vicinity of the spectra peak, and for the low end of the spectral peak ($St_\delta < 1$), all cases show good collapse. The peaks for all measured spectra are at approximately $St_\delta = 1.0$, independent of Reynolds number. In Gordeyev, et al. (2014) it was shown that using Kolmogorov-like arguments for the inertial range, the deflection angle amplitude spectrum at large frequencies should behave as $\sim f^{(-2/3)}$; this curve is plotted in Figure 4.1 as a dashed black line. The spectrum at the lowest Reynolds number quickly falls off of this theoretically predicted behavior, indicating a fairly small inertial range, while the fall-off is less drastic for larger Reynolds numbers, implying a larger inertial range.

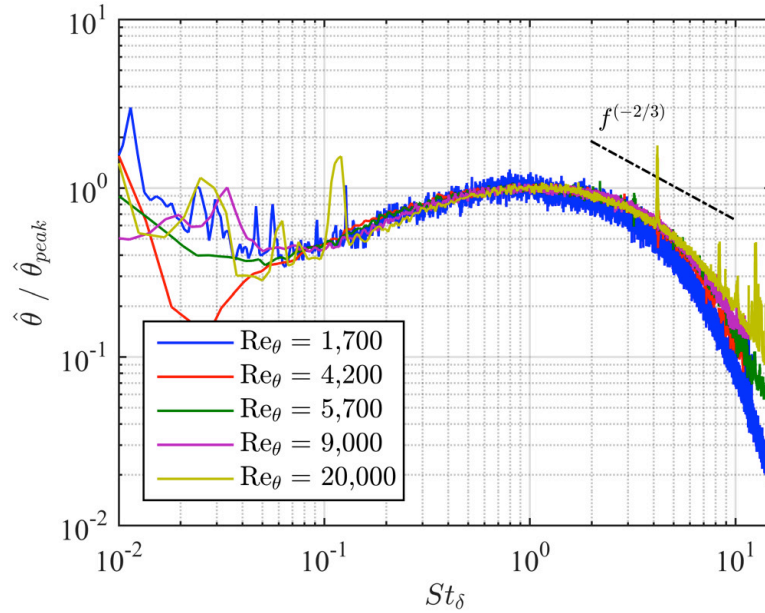


Figure 4.1. Normalized deflection angle spectra for different Reynolds numbers.

To model the observed changes in the (high frequency slope) size of the inertial range of deflection angle spectra for different Reynolds numbers, the spectral model from presented in Gordeyev, et al. (2014) was modified in order to account for changes in the spectra roll-off as a function of Re_θ . The fall-off of the spectra was assumed to take a form inspired by Tatarski's modification of Kolmogorov's atmospheric wavefront spectrum to account for the presence of inner scale dissipative structures (Tatarski, 1971). Seeking a function in the form of the original model times the exponential term, the modified spectral model was found to be

$$\hat{\phi}_{\text{fit}}(St_\delta) = \hat{\phi}_{\text{peak}} \frac{St_\delta}{1 + (St_\delta / 0.83)^{5/3}} \exp \left[- \left(\frac{St_\delta}{f(Re_\theta)} \right)^2 \right] \quad (4.1)$$

The $f(Re_\theta)$ term was empirically determined to be $f(Re_\theta) \approx 1.6 Re_\theta^{(0.22)}$ by fitting equation (4.1) to the experimental data presented in Figure 4.1.

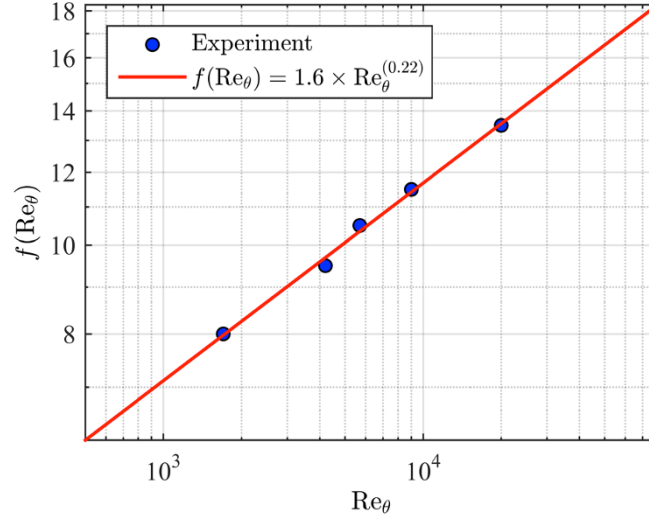


Figure 4.2. Empirically determined values of $f(\text{Re}_\theta)$ from equation (4.1) and the corresponding power law fit.

Figure 4.3 shows comparisons between experimental data and the modified model, equation (4.1), for four Reynolds numbers ranging from 1,700 to 20,000. For $St_\delta < 0.5$, the experimentally measured spectra and model spectra deviate from one another, with the experimentally measured spectra containing more energy. This behavior is consistent with results from previous studies, where it was shown that for Malley probe measurements, this increase in energy is a result of contamination from mechanical vibrations in Malley probe data that cannot be properly removed (Gordeyev et al, 2014). For $St_\delta > 0.5$, Figure 4.3 shows that the modified spectral model, equation (4.1), does a good job of describing the high-frequency roll-off behavior for a large range of Reynolds numbers.

Heated wall TBL wavefront statistics can also be used to evaluate the validity of scaling laws for OPD_{rms} at low Reynolds numbers. One method of doing this is to rearrange the terms of the TBL aero-optic model presented in equation (3.18) to solve for the model constant, B :

$$B = \frac{OPD_{rms}(\Delta T = 0)}{K_{GD} \rho_\infty \delta M^2 \sqrt{C_f}} \quad (4.2)$$

Here the only term that explicitly depends on Reynolds number is C_f , and there are a number of relations for computing C_f as a function of Re_θ that compare with experimental measurements (Nagib, et al., 2007). Therefore if the assumptions used to derive equation (3.18) are valid at low Reynolds numbers, the model constant should be consistent with what was found at high Re_θ , where $B = 0.19 \pm 0.01$ (Gordeyev et al., 2014).

Equation (4.2) was used to estimate B from experimental data obtained at low Reynolds number, using values of $OPD_{rms}(\Delta T = 0)$ measured directly for adiabatic wall conditions and values of $OPD_{rms}(\Delta T = 0)$ estimated from a linear fit of heated wall data. The results of these estimates are shown in Figure 4.4, compared with the previously obtained experimental value of $B = 0.19 \pm 0.01$ from Gordeyev, et al. (2012). Good agreement was found between values of B estimated from equation (4.2) for both adiabatic wall wavefront measurements and heated wall wavefront measurements at low Reynolds numbers, especially for $\text{Re} > 5,700$. At $\text{Re} = 4,200$, there is a slight increase in the value of $B_{estimated}$ to about $0.22 - 0.23$, however the error bars for these estimates are large.

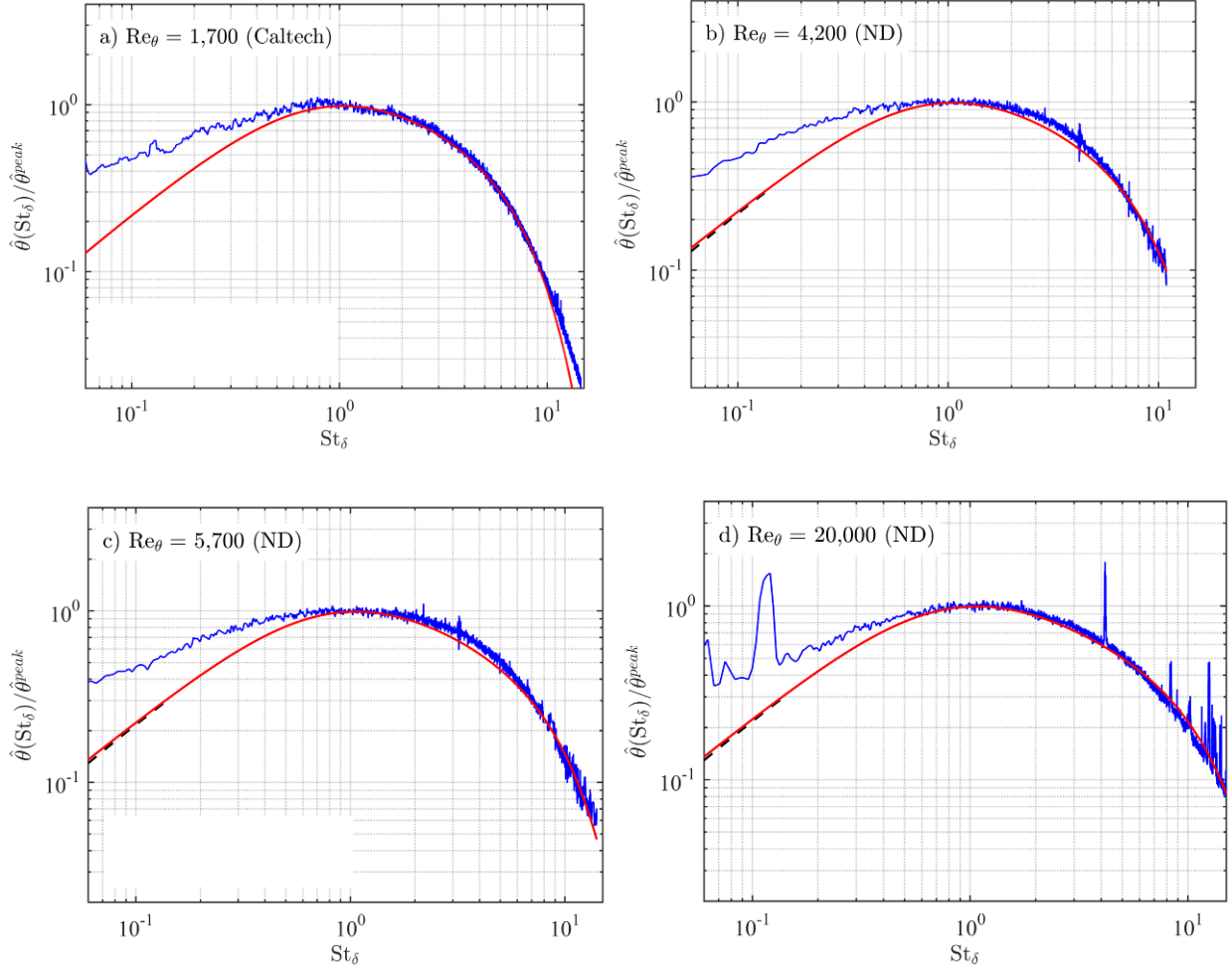


Figure 4.3. Comparison of experimental deflection angle spectra (blue line) and the modified empirical model from equation (4.1) (red line) for Reynolds number, Re_θ , a) 1,700 (Caltech), b) 4,200 (Notre Dame), c) 5,700 (Notre Dame), and d) 20,000 (Notre Dame).

4.3 Conclusions and Discussion

This chapter presented the results of aero-optic wavefront measurements of heated-wall boundary layers for a range of subsonic Mach numbers from 0.03 to 0.4, and Reynolds numbers $Re_\theta = 1,700 - 20,000$. The effect of increased wall temperatures on deflection angle spectra was analyzed, and it was found that heating indeed acted as a passive amplifier on TBL turbulence, confirming that the wall heating scaling laws developed by Cress (2010) for higher Reynolds number TBLs were valid for Reynolds numbers at least as low as 4,200. Using the scaling laws, it was shown that equation (3.18) for heated walls could be used to re-scale heated-wall wavefront data to recover wavefront statistics for adiabatic wall temperatures at low Reynolds numbers.

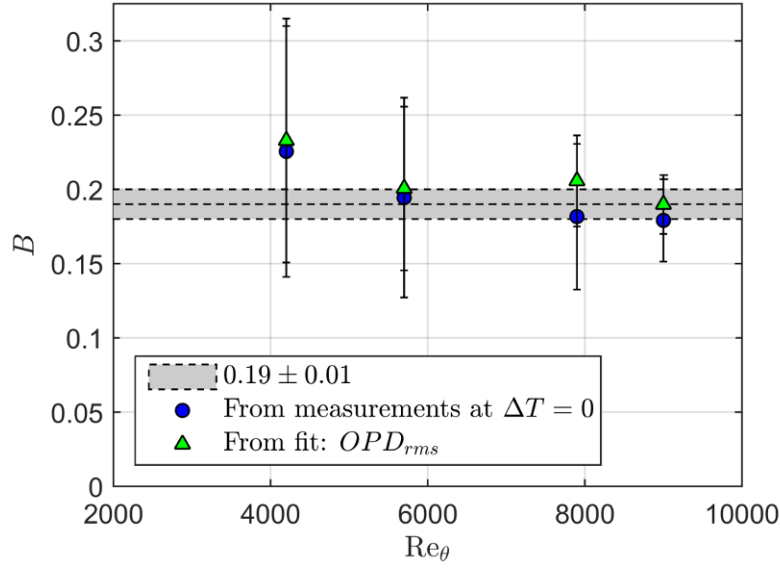


Figure 4.4. Model constant B from equation (3.18) estimated from low-Reynolds number wavefront measurements from OPD_{rms} .

Wavefront spectra from both heated and un-heated walls were extracted and compared to investigate the effect of Reynolds number on the shape of boundary layer wavefront spectra. It was found that the inertial sub-range of aero-optic wavefront spectra is reduced with decreasing Reynolds number, which is consistent with previous observations of other turbulence spectra (Tatarski, 1971). The empirical spectral model was modified in order to model this Reynolds number dependence by the addition of an exponential decay term (which is a function of Reynolds number) that approximates the high frequency roll-off observed in the experimentally measured wavefront spectra. The modified model was shown to agree well with spectra obtained from experiments spanning an order of magnitude in Reynolds number, from $Re_\theta = 1,700 - 20,000$.

The presented method for extracting wavefront statistics TBLs from heated wall wavefront data provides a novel and promising method for studying the aero-optic characteristics of TBLs that would otherwise be difficult to measure due to the problem of aero-optic ‘invisibility’ that occurs when Mach and/or Reynolds numbers in the TBL are low. This approach for obtaining low Reynolds/Mach number TBL wavefront data is especially useful for studying low-Reynolds number TBLs using non-intrusive aero-optic wavefront sensors. This technique, along with the modification proposed to the spectral model for Reynolds number dependence, are important developments in obtaining experimentally measured low Reynolds number TBL wavefront statistics for comparison to computational results, which are limited to low Reynolds numbers by limitations of practical parameters for simulations.

5. Simultaneous Optical/Velocity Measurements

5.1 Motivation

Large-scale structures, located in the outer part of the subsonic boundary layer carry an important role in boundary layer dynamics, responsible for entrainment process and, via a link with small-scale structures near the wall, for instantaneous drag near the wall, to mention a few (Marusic et al., 2010). While there exists a large body of experimental research about the large-scale structures (Smits et al, 2011), there are open questions about their topology, dynamics and the interaction with the near-wall structures.

Traditionally, large-scale structures are characterized by the velocity field, which is measured using hot-wires or a PIV technique. These techniques give either detailed temporal information in a few spatial points (hot-wires) or potentially time-resolved spatial velocity field information in a plane (particle image velocimetry, PIV). In order to get instantaneous three-dimensional information about the structure, one has to resort to rather complex techniques, like tomographic-PIV (Elsinga et al., 2006) or plenoptic (Farbinger and Thurow, 2012) techniques, for example. An alternative way to non-intrusively study the characteristics of large-scale structures in boundary layers is to measure related density distortions using various wavefront sensors.

5.2 Approach

In this work, we leverage both velocimetry and optical techniques to characterize large scale structure in incompressible and compressible turbulent boundary layers. .

As stated before, in incompressible, wall-heated boundary layers density fluctuations occur due to total temperature variations. Above $M = 0.3$, compressibility effects can also change the density. If the total temperature is assumed to be a constant, which is equivalent to zero pressure fluctuations, the density fluctuations, ρ' , in boundary layers are due to the static temperature fluctuations, T' , (adiabatic cooling/heating). which is the base for the Strong Reynolds Analogy, discussed earlier in Section 3.2.

The time-averaged version of SRA was shown to correctly estimate the time-averaged levels of BL aero-optical distortions (Gordeyev et al. 2014). If instantaneous wavefronts and velocity fields are known, it is possible to estimate the validity of the instantaneous version of SRA,

$$C_p T'(\bar{x}, t) = -\bar{U} u'(\bar{x}, t) \quad (5.1)$$

by comparing measured wavefronts and estimated wavefronts from instantaneous velocity field using equations (1.1) and (5.1).

In Chapter 3 it was shown that if the boundary layer wall is moderately-heated relative to the freestream density, it will not modify the underlying velocity structure. Instead, moderate heating will simply introduce passive temperature markers in the boundary layer and effectively amplify aero-optical levels. In other words, by introducing moderate-temperature mismatch between the wall and the boundary layer, it is possible to *thermally tag* and measure three-dimensional large-scale structures in *incompressible* boundary layers.

The similarities between compressible and incompressible aero-optical distortion statistics have two implications. First, they suggest that aero-optical distortion studies can be carried out in incompressible tunnels, opening up more avenues for measurement. Secondly, and arguably more importantly, they suggest that inherent features of turbulence, rather than specific compressibility effects, underlie the patterns of aero-optical distortion seen in compressible and heated,

incompressible flow. With these ideas in mind, this study examines aero-optical distortion in a heated, incompressible flow while simultaneously measuring flow features to examine how turbulent structures affect laser distortion.

Two simultaneous wavefront-velocity experiments were conducted at a low subsonic speed at California Institute of Technology (Caltech), using the moderately-heated approach and at a compressible subsonic speed at University of Notre Dame. A Malley probe was used in the Caltech experiments to characterize optical distortions and obtain an appropriate mean convection velocity. A Shack-Hartmann sensor was used to obtain more detailed, two-dimensional aero-optical information in the Notre Dame experiments, specifically, the two-dimensional, time-resolved *OPD*.

5.3 Experimental Setup: Caltech

Experiments are conducted in the Merrill wind tunnel at Caltech, a recirculating facility with a 2ft x 2ft test section. A turbulent boundary layer is developed over a partially heated flat plate at a Reynolds number of 3300. The plate is heated to between 15 and 20 C above the free stream temperature. A Malley probe is used to measure aero-optical distortion and Particle image velocimetry (PIV) is used to measure the velocity field in a wall-normal, streamwise plane. The PIV laser sheet is aligned to be coincident with the Malley probe beams in the spanwise and streamwise directions. PIV images are taken at 1500 Hz, double pulsed with a 35 μ s separation between pulses. The field of view is 60 mm x 60 mm ($1.7\delta \times 1.7\delta$). A schematic of the experimental setup showing the thermal boundary layer the passage of the Malley probe beams through the flow, and the location of the PIV light sheet in the flow is presented in Figure 5.1.

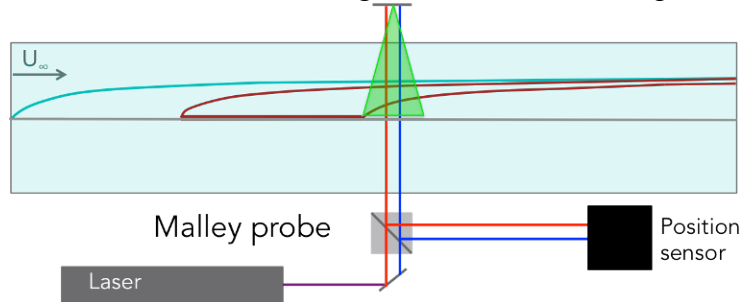


Figure 5.1. Schematic of the experimental setup. A turbulent boundary layer is shown developing over a partially heated flat plate. A thermal boundary layer develops with an inner and outer edge. The Malley probe beams are passed up and back through the flow. The red line indicates the upstream beam while the blue indicates the downstream beam. The green triangle indicates the location of the PIV light sheet in the flow.

The heated plate that seeds density variation into the flow ends upstream of the measurement location creating an inner thermal boundary layer. The temperature was measured with a cold wire as a function of height over a fully heated wall and over the measurement location. Figure 5.2 shows these temperature profiles and compares them to data from Antonia & Kawamura, 1977 of a heated turbulent boundary layer. The fully heated and partially heated profiles are seen to diverge at a $y^+ = 100$ or $y/\delta = 0.13$. The partial heating allows for a focus in the outer boundary layer, which highlights the regions of interest in the flow for this study. It also does not seem to impact the comparison to the compressible case, as the average convection

velocities and spectra look the same between the partially heated, incompressible case and the compressible case.

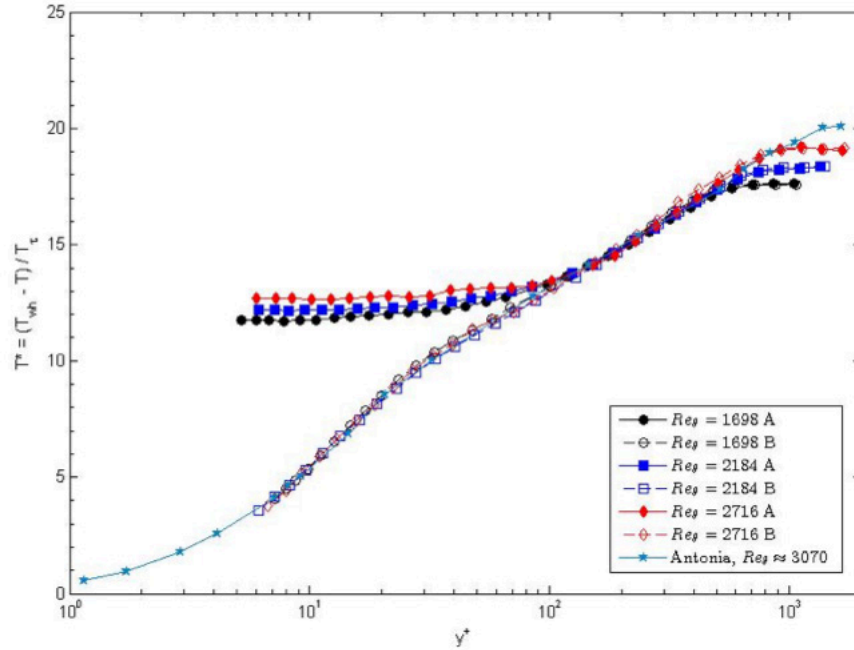


Figure 5.2. Normalized averaged temperature relative to the wall temperature as a function of distance from the wall. The temperature profiles that plateau are measured at the measurement location (A) while the temperature profiles that decay to zero are measured directly over the heated wall (B). The average temperature profile in the partially heated case diverges from the fully heated case at roughly $y^+ = 100$ or $y/\delta = 0.13$ (Rought 2013; Antonia et al 1977).

Sample data from the Malley probe and PIV measurements are shown in Figure 5.3. The streamwise deflection angles of the two Malley probe beams are shown as a function of time in Figure 5.3(a). The vertical black line indicates the time at which the PIV data shown in Figure 5.3(b) was taken. Figure 5.3(b) shows a vector plot of the velocity field with a convection velocity of $0.83U_\infty$ subtracted off to show the structure in the flow. The locations of the two Malley probe beams are indicated by the red (upstream beam) and blue (downstream beam) lines. The figure shows a smaller field of view than is available in order to more easily see the structure.

5.4 Results: Caltech

5.4.1 Statistics

The mean and RMS velocity statistics are found from the PIV data and compared to data from DeGraaff & Eaton, 2000 at similar Reynolds numbers. The data is found to agree well above a y^+ of about 40 or equivalently $y/\delta = 0.05$. Figures 5.4(a) and 5.4(b) show the mean and RMS compared to the DeGraaff & Eaton, 2000 data.

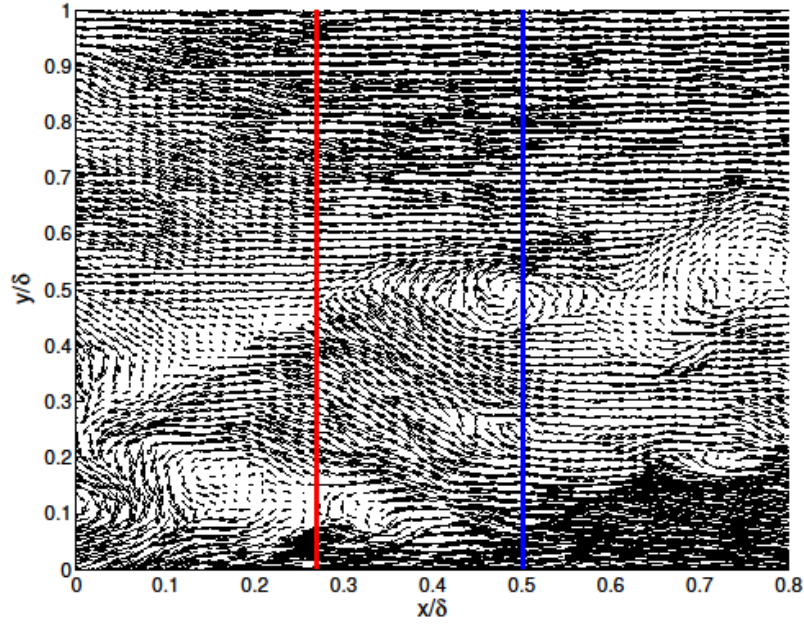
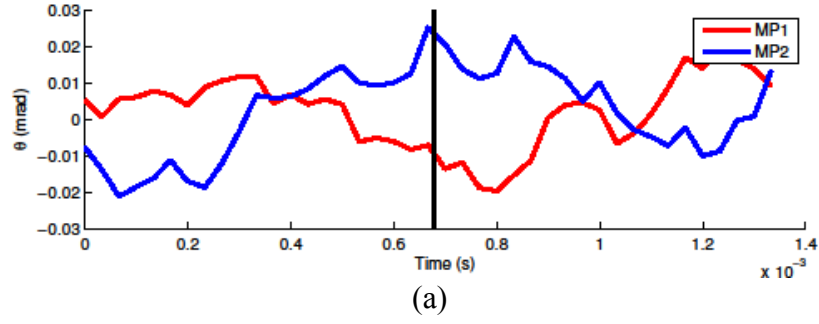


Figure 5.3. Sample Malley probe (a) and PIV (b) data. Red line indicates upstream Malley probe beam while blue line indicates downstream Malley probe beam. (a) shows the streamwise angle as a function of time for each beam. The black vertical line in (a) indicates the time at which the PIV data shown in (b) was taken. (b) shows the instantaneous velocity field with $0.83 U_\infty$ subtracted off to be able to see structure. The field of view shown is smaller than the available field of view to more easily see structure in the flow. Vertical red and blue lines are drawn in to indicate the locations of the upstream and downstream Malley probe beam paths.

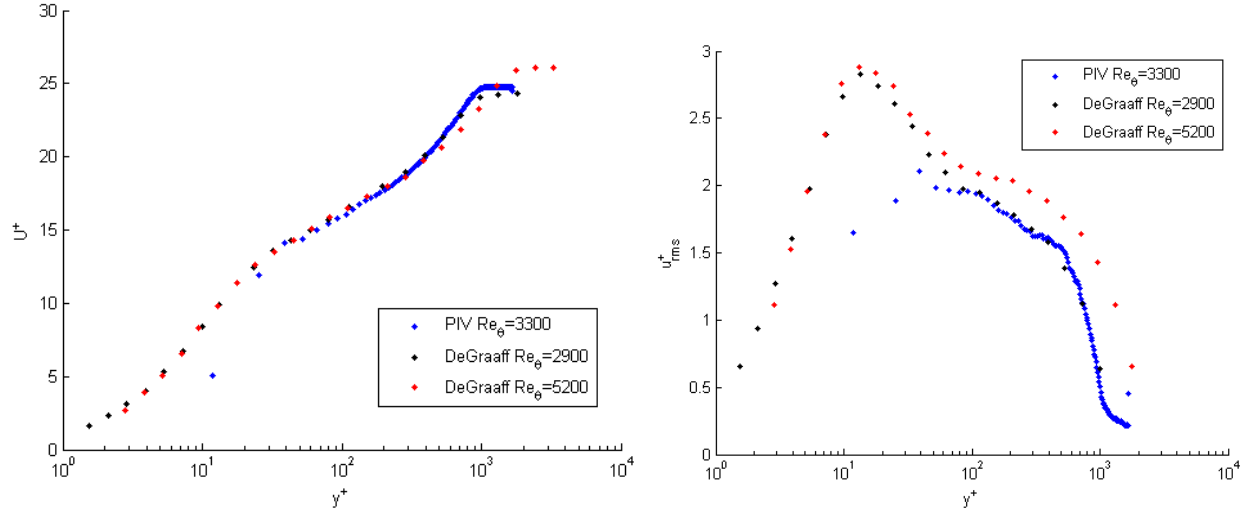


Figure 5.4. Mean profile (a) and RMS (b) as a function of distance from the wall. Blue points indicate data from PIV measurements in this study. Black and red points indicate data from DeGraaff & Eaton, 2000 at similar Reynolds numbers for comparison. Data is seen to agree above a y^+ of about 40 and agree very well above a y^+ of about 100 (DeGraaff & Eaton, 2000).

5.4.2 Convection Velocities

Convection velocity information is obtained from the aero-optical distortion measurement using a Pearson correlation, defined as:

$$R(\tau) = \frac{\sum_t \theta_1(t) \theta_2(t + \tau)}{\left(\sum_t \theta_1(t)^2 \sum_t \theta_2(t)^2 \right)^{1/2}} \quad (5.1)$$

where θ_1 is the upstream beam and θ_2 is the downstream beam. The value of τ that gives the largest value of R is taken as the convection time for a disturbance to travel from the upstream Malley probe beam to the downstream Malley probe beam.

The correlation can be done over small periods of time (in this study, local correlation is performed over 1.4 ms or 0.5 convective time units) to find a local convection velocity that ideally corresponds to a single structure, or can be done over the full length of the signal to find a global convection velocity of the structures. The average of all local convection velocities is found to be $0.85U_\infty$ with a standard deviation of $0.1U_\infty$. The global convection velocity is found to be $0.83U_\infty$. These convection velocities of about $0.8 U_\infty$ suggest that something in the outer boundary layer is most responsible for the deviations in the laser path. By comparing the convection velocity to the mean velocity profile, an average height of the relevant structures can be computed. Figure 5.5 shows the heights corresponding to $0.83U_\infty$ and $0.85U_\infty$ in an instantaneous velocity field (a) and the mean profile (b). An average height of $0.5U_\infty$ is observed.

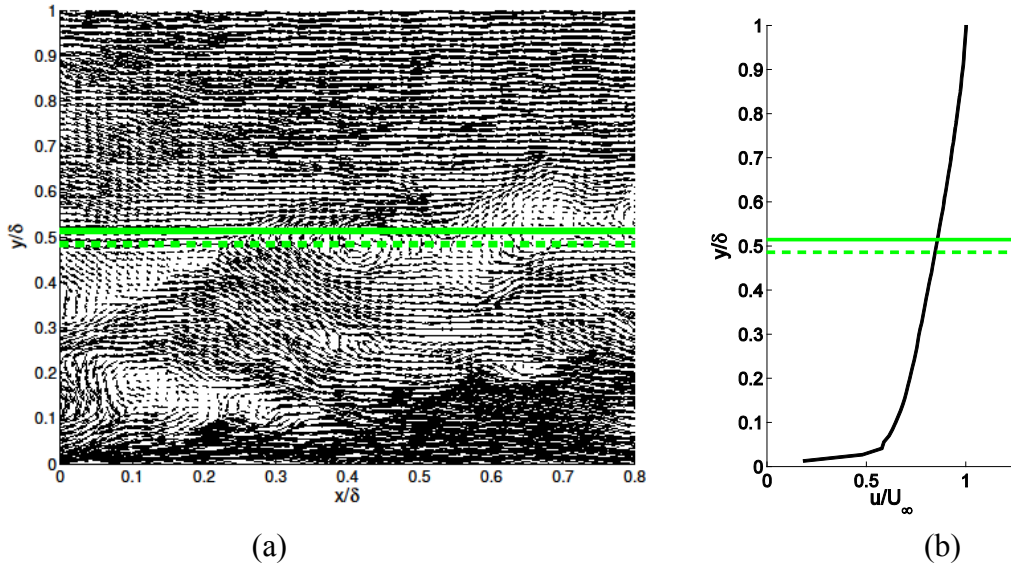


Figure 5.5. The height corresponding to the average convection velocity of angle deviations is indicated relative to an instantaneous vector plot (a) and the mean velocity profile (b). The solid green line indicates the height at which the mean velocity is $0.85 U_\infty$, the average value of the local convection velocities. The dashed green line indicates the height of at which the mean velocity is $0.83 U_\infty$, the global convection velocity found by correlating the full signal.

5.4.3 Conditional Averaging

Conditional averaging is next used to find patterns in the velocity field that consistently leads to large deflections in the laser path. The velocity field surrounding a Malley probe laser path is conditionally averaged on large positive (defined as downstream) deflections and large negative (upstream) deflections separately. Figure 5.6(a) shows the average velocity field given a condition of a positive deviation in the laser angle larger than half of the maximum deviation, while Figure 5.6(b) shows the average velocity field for a negative deviation in the laser angle less than a third of the minimum deviation. The condition on positive deviations is stronger than that on negative in order to have roughly 50 frames averaged per 1024 frame run for both positive and negative averages. The difference in the conditions is caused by a non-uniform distribution in laser deflections, reflected in the negative skewness of the deflection angle signal.

Each figure has a particular convection velocity subtracted from the full flow, which highlights a particular region of the flow. The average of the local convection velocities found for the large positive deflections is subtracted from the full velocity field in Figure 5.7. The equivalent procedure is done for the large negative deflection convection velocities for Figure 5.8. For large positive excursions in the laser deflection angle, a vortex pattern is observed in the conditionally averaged flow, while for large negative excursions, a stagnation point is observed. Both are observed to travel with the same approximate convection velocity of $0.85U_\infty$ and at a height 0.5δ .

However, if the subtracted convection velocity is changed, the same feature is visible at different heights in the flow. Figures 5.7 and 5.8 show the change in position of the vortex and stagnation point respectively as the subtracted convection velocity is changed. The conditionally averaged flow highlights a feature that occurs at many heights and convection velocities in the flow. This suggests that the laser deflection angle can be affected by structures in a relatively

large region of the flow, but the relationship between the laser deflection and shape of the structure is consistent. Vorticity along the beam path generates downstream deflection, while stagnation and shear along the beam path generates upstream deflection.

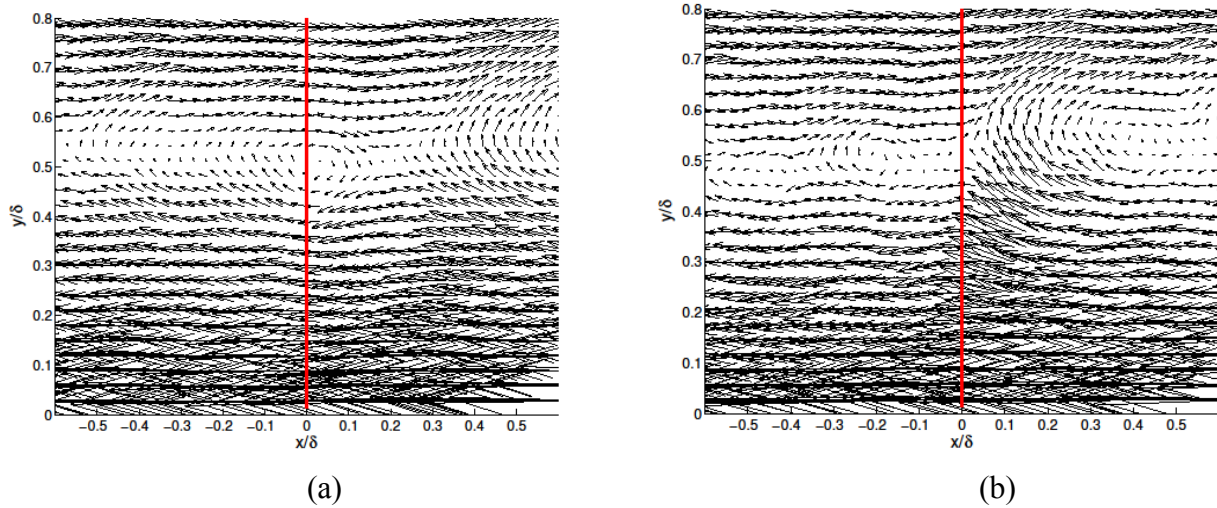


Figure 5.6. Average of the velocity field around the laser beam path during large excursions in the laser deflection angle, θ . Large positive excursions, defined as $\theta > 0.5 \max \theta$, produce a vortex structure in the velocity field (a). Large negative excursions, defined as $\theta < 1/3 \min \theta$, produce a stagnation point in the velocity field (b). Positive θ is defined as a downstream bend in the laser, while negative θ is defined as an upstream bend. The average convection velocity of the deflection events is subtracted from the velocity field, in this case $0.85 U_\infty$, allowing the structures to be visible. The red line indicates the position of the Malley probe beam in the velocity field. Both structures are observed to sit at a height of 0.5δ .

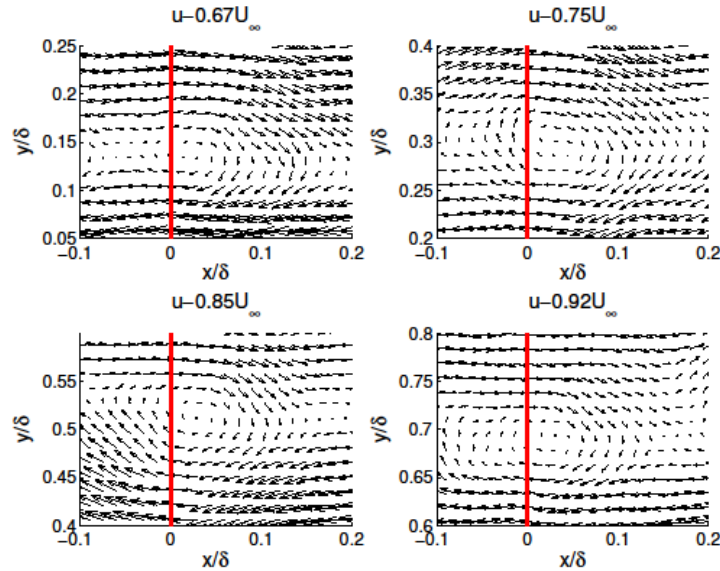


Figure 5.7. Vector plots show a close-in perspective on the conditionally averaged velocity data shown in Figure 5.6a with varying convection velocities subtracted off. Each velocity allows a vortex to be visible at a different height in the flow. The presence of vorticity along the beam path in a large region of the flow is consistent with strong downstream deflections in the beam path.

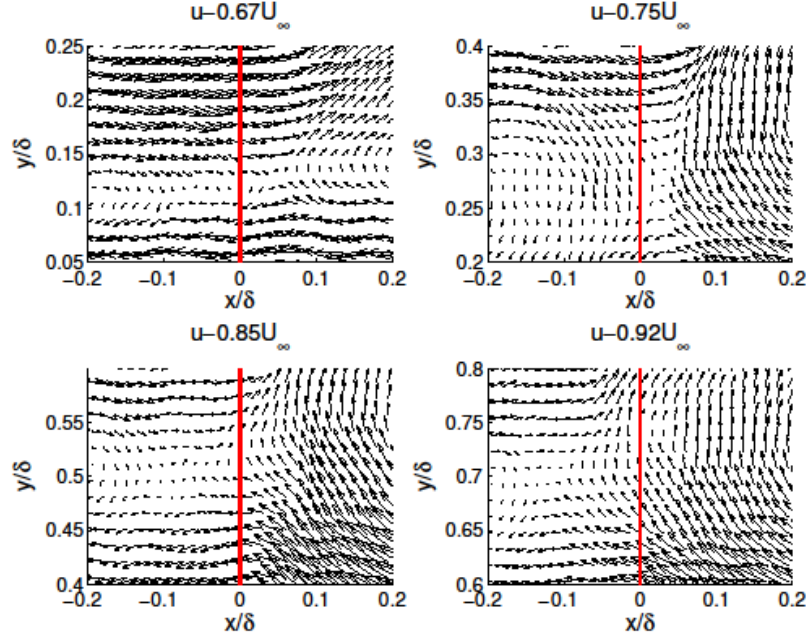


Figure 5.8. Vector plots show a close-in perspective on the conditionally averaged velocity data shown in Figure 5.6b with varying convection velocities subtracted off. Each velocity allows a stagnation point to be visible at a different height in the flow. The presence of a stagnation point along the beam path in a large region of the flow is consistent with strong upstream deflections in the beam path.

5.4.4 Correlation

To continue probing the relationship between the velocity field and the laser distortion, correlations are carried out between the laser probe deflection angle and the velocity at a specific point in space for each PIV frame. The vertical velocity is extracted from velocity field at the x -location of the Malley probe beam and a y -location y_c . y_c is chosen using convection velocity arguments demonstrated in Figure 5.5. The local convection velocity of the Malley probe signal is compared to the mean velocity profile. The height at which the mean profile matches the local convection velocity is taken as y_c .

The vertical velocity, $v(x_{MP}, y_c)$, is correlated to the laser deflection angle τ at each PIV time step. A Pearson correlation coefficient, defined as:

$$R(\tau) = \frac{\sum_t v(t)\theta(t+\tau)}{\left(\sum_t v(t)^2 \sum_t \theta(t)^2\right)^{1/2}} \quad (5.2)$$

of $R = -0.28$ is found with a time delay normalized by outer units of $\tau U_\infty / \delta = 0.12$. Figure 5.9 shows the correlation coefficient as a function of the time delay τ .

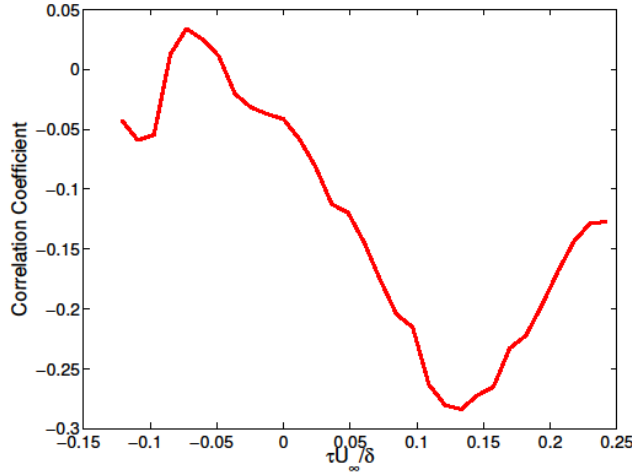


Figure 5.9. Correlation of the vertical velocity v with θ as a function of time delay. The maximum absolute value of the correlation coefficient is found at a normalized time delay of 0.13. The negative sign of the correlation indicates that opposite-signed deviations in v and θ are related. The time delay suggests that the part of the feature that has a strong velocity disturbance and the part that strongly affects the laser propagation angle are separated with some specific spacing in the flow.

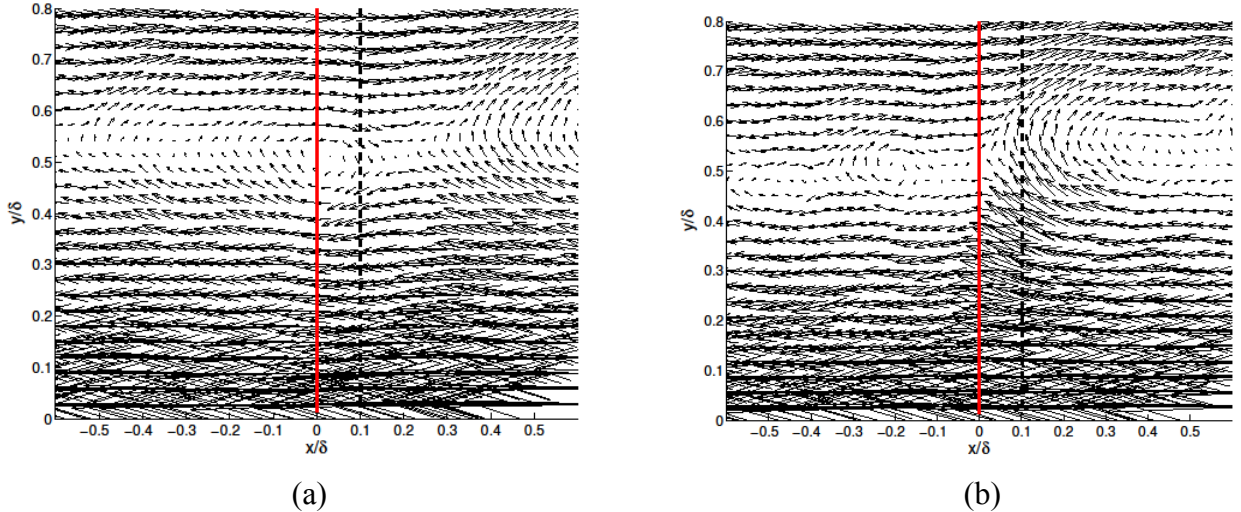


Figure 5.10. A comparison of conditional averaging and correlation results. The vector plots shown are the conditional averages on large positive (a) and negative (b) deviations in θ . The red line indicates the location of the θ event. The black dashed line shows the x -location where there should be a correlated negative (a) or positive (b) v event, given the time delay found in the correlation. At a height of 0.5δ the velocity fields show a strong $-v$ event (a) and strong $+v$ event (b) at the x -location where the correlation predicted these events, indicating that the conditional averaging and correlation results agree.

The negative correlation indicates that opposite-signed deviations in v and θ are related. The time delay suggests that the part of the flow that has a strong velocity disturbance occurs upstream of the part of the flow that causes a strong deflection in the laser path. In order to

investigate this aspect of the correlation, the time delay is translated to a spatial displacement using the local convection velocity. That spatial displacement is then compared to the results of the conditional averaging. The location of correlated events is overlaid with the conditional averaging results in Figures 5.10(a) and 5.10(b). The vector field in each plot is the conditional average shown previously. The red line indicates the location of a large deviation in laser angle, while the black line indicates the location of a correlated velocity event of the opposite sign. Good agreement is seen between the location of the black line and strong velocity signals of the appropriate sign in the conditionally averaged velocity fields.

5.5 Discussion

The presence of structure in the conditionally averaged velocity field and the correlation between the vertical velocity and the laser deflection both support the idea that structures in turbulence shape the laser deflection angle. However, the mechanism of how these structures create these laser deflections is perhaps not obvious from the data. A hypothesis is proposed that fits the patterns of the data, and opens room for more questions.

The vortex and stagnation point seen in the conditionally averaged velocity fields are hypothesized to be associated with hairpin vortices. Hairpins have been studied at great length by the turbulence community and have the features that are seen in the conditionally averaged flow field. They sit in the appropriate region of the flow to have an average convection velocity of $0.8U_\infty$ and the hairpin packets are of the right size to give a peak in the deflection spectrum at St_δ of order one (Adrian et al 2000).

Hairpins have previously been argued to lie along an interface between fast and slow moving 'momentum zones' and form hairpin packets (Adrian et al 2000). The fast and slow moving fluid may be associated with cold (free stream) and warm (near-wall) fluid respectively using passive scalar transport arguments. If hairpins lie along a boundary between warm and cold regions of air, they might shape that boundary in ways that consistently deflect the laser, giving the results shown. Figure 5.11 shows a model of the separation between warm and cold regions of flow. The specific gradient at the vortex head that causes a upstream leaning deviation requires further study.

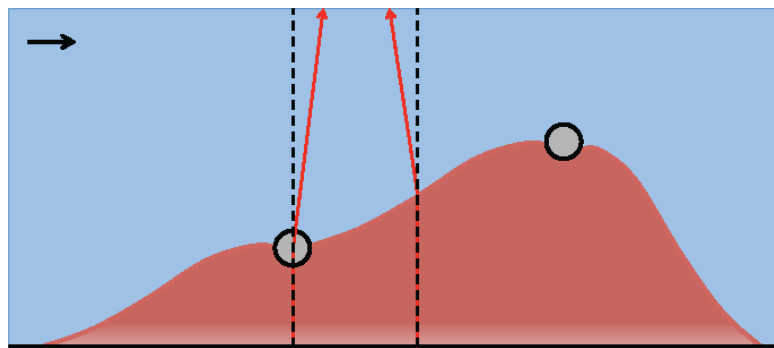


Figure 5.11. Model of warm (red) and cold (blue) regions of the flow. Grey circles represent hairpin heads, with the shear layers trailing down the backside of the temperature interface. Laser paths are drawn in to represent the types of deflections seen in the conditional averaging. The slight gradient in color at the bottom of the warm region indicates the height cold inner temperature region present due to the wall heating element ending before the measurement location.

The observation that structures in turbulence are tied directly to laser deflections opens many new questions. Future work will focus on how the structures shape the density field and therefore affect the laser deflections, as well as how the structures may be tied to the pickup of heat at the wall. Additionally, future work will explore the range of sizes and convection velocities associated with optically aberrating structures to better quantify the scales that are optically important in turbulent boundary layers.

5.6 Conclusions: Caltech

This study aims to understand the connection between aero-optical distortion in turbulent flows and turbulent velocity structure. Aero-optical distortion and the fluid velocity field are simultaneously measured in a heated turbulent boundary layer. Conditional averages are used to determine the velocity structure that yields large deflections in the laser propagation angle. Large downstream deflections in the laser are found to be consistent with the presence of a vortex passing through the laser path. Large upstream deflections in the laser are found to be consistent with the presence of a stagnation point or shear layer passing through the beam path. A Pearson correlation is performed between the vertical velocity, v , and the laser deflection angle, yielding a correlation coefficient of $R = -0.28$. A specific separation in space between the velocity and deflection angle events is found to maximize their correlation, suggesting a specific size of the turbulent structure. A hypothesis is put forward that the beam is distorted by the passage of hairpin vortices, which are characterized by both vortex heads and trailing shear layers. The hairpins are proposed to lie along the interface between warm and cool regions in the flow, much as they have been shown to lie along the interface between regions of low and high streamwise momentum. Hairpin vortices are thought to affect the beam deflection angle by shaping a sharp gradient in density in the flow.

5.7 Experiments: Notre Dame

Measurements were obtained in the Hessert Transonic Wind Tunnel (TWT) at the University of Notre Dame. Freestream velocity was held constant at $M = 0.4$ for the duration of the measurements.

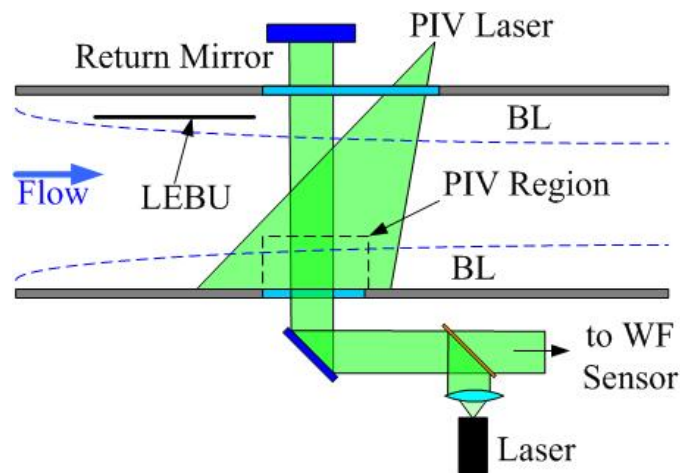


Figure 5.12. Schematic of of the simultaneous Velocity-Wavefront measurements using Shack-Hartmann 2-D wavefront sensor at Notre Dame.

The experimental set-up at Notre Dame, shown in Figure 5.12, was similar to the one at Caltech with two major differences. Unlike the 1-D wavefronts, measured with the Malley probe at Caltech, full circular 2-D wavefronts, resolved in both the streamwise (x) and the spanwise (z) directions, were collected using a high-speed Shack-Hartmann wavefront sensor. The wavefront aperture was 50 mm. The second difference was that both boundary layers on the opposite tunnel walls were optically-aberrating. In order to minimize the optical effect of the upper boundary layer, a Large Eddy Break Up (LEBU) device $l = 72$ mm, $h = 11$ mm device was mounted on the upper wall of the BL development section to reduce the level of optical aberrations caused by the upper BL. Its trailing edge was located 2.6 cm upstream of the start of the optical window. Estimations based on results from Chapter 2 showed that the LEBU device reduced the aero-optical distortions of the upper boundary layer by a factor of 1.7.

Velocity data were acquired at a rate of 2 kHz using a commercially available 2-D PIV LaVision system in double-pulse, double-frame mode. The laser sheet was aligned along the tunnel centerline, and the frame resolution of the camera was 768×768 , with a field of view of approximately 100 mm. The time interval between laser pulses for each measurement was 10 μ s. The PIV image pairs were cropped and processed in DaVis 8.2 in order to calculate the velocity vector field at intervals of 0.53 mm in the streamwise and wall-normal directions.

Wavefront measurements with the spatial resolution of 40×40 subapertures were simultaneously acquired using a Shack-Hartmann sensor, which consisted of a high-speed camera (Phantom v1611) with a mounted lenslet array, 3 μ s after the first laser pulse, so as to have wavefront data that closely corresponded to each image pair used to calculate the velocity field. The shutter duration for the Shack-Hartmann sensor was only 0.452 μ s, and the points at which wavefront measurements were obtained were distributed at 1.2 mm intervals in the streamwise and spanwise directions. The aperture diameter of the wavefront beam was approximately 5 cm, with its upstream edge passing through the optical window at $x = 133$ cm.

The boundary layer thickness, δ_{99} , at the measurements location was found to be approximately 15.6 mm. Integration of the velocity profiles, collected with PIV system gave δ^* to be 2.4 mm and $\theta = 1.74$ mm. Based on these values, $Re_\tau = 4,780$ and $Re_\theta = 15,500$.

Time-averaged levels of *OPD* from the velocity data were found approximately 25% less than the *OPDrms*, calculated from wavefronts. The difference was attributed to the presence of the optically-weakened upper boundary layer.

5.8 Results: Notre Dame

For each velocity field, the estimated 1-D slice of the wavefront was calculated using equations (1.1) and (5.1). The resulted wavefronts (not shown) were compared to the 1-D slices of the measured wavefronts along the centerline (Figures 5.13 and 5.14). Instances with significant local differences between the estimated and actual wavefronts were investigated. As the estimated wavefronts rely on SRA, these instances should correspond to the cases where the pressure/total temperature fluctuations are not negligible. Two events in the measured wavefront slices were considered, local *OPD* minima and maxima, and the velocity fields were inspected in attempt to identify the probable relation between the wavefront minima/maxima and a corresponding velocity features.

5.8.1 Local *OPD*-minima.

Several representative flow fields, when the local wavefront minimum was observed, are shown in Figure 5.13. The upper plot shows the actual 2-D *OPD* (in false color) and the 1-D *OPD*

slice (black line). The bottom plot shows the instantaneous U -velocity with the mean convection velocity of optical disturbance, $0.82U_\infty$, subtracted (velocity vectors), superimposed with the instantaneous fluctuating u -field (false color). It was observed that in most cases the local OPD minimum corresponds to the presence of the large-scale, order of d , structure, which is characterized by negative u -fluctuations near the wall and positive u -fluctuations away from the wall. Such large-scale structure has been observed to correspond to the signature of a packet of hairpin vortical structures by many other researchers (Adrian, 2007, Hutchins et al., 2005, for instance). There is some evidence of vortical motion reminiscent of hairpin heads in the PIV images.

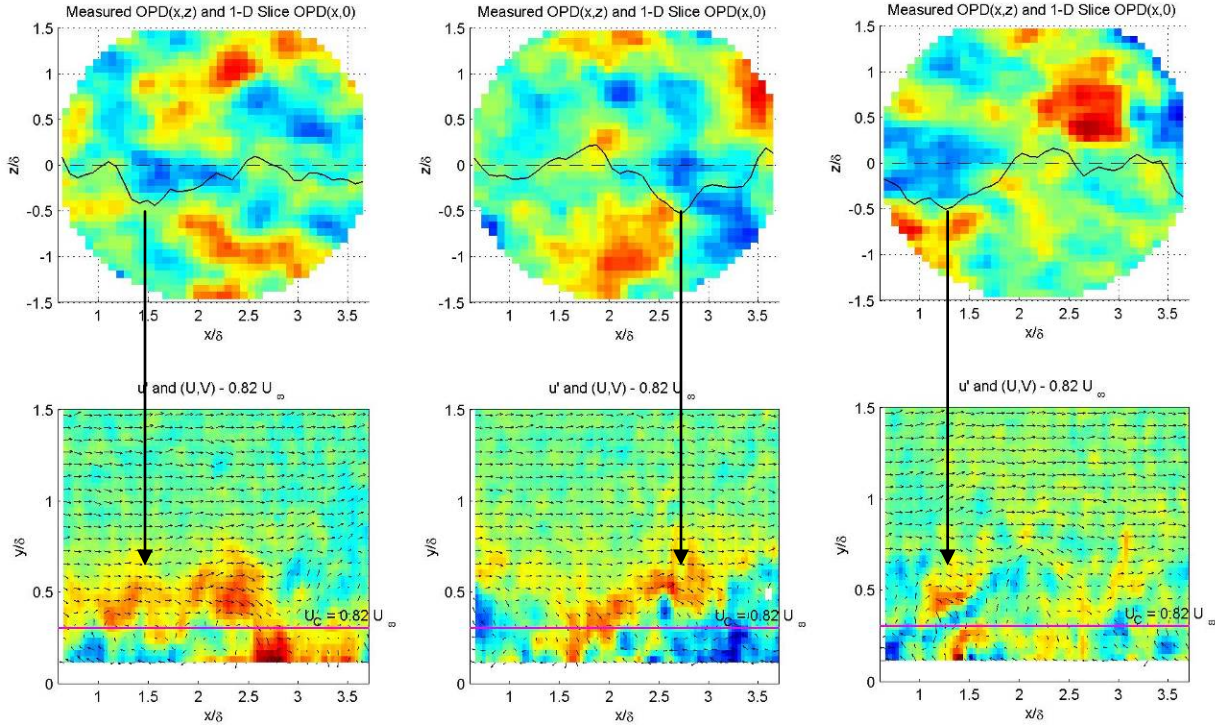


Figure 5.13. Top: Representative wavefronts with *local minima* near the PIV centerline (dashed line). Measured 2-D OPD are given by false color map, blue are negative values and red are positive values, and the measured 1-D $OPD(x,0)$ slices are shown as black lines. Bottom: the corresponding velocity fields. Velocity vectors are the instantaneous U -velocity with $0.82U_\infty$ subtracted, superimposed with the instantaneous fluctuating u -field (false color map, blue are negative values and red are positive values). Solid magenta line indicates a y -location, where the local mean U -velocity is 0.82 of the freestream speed.

The discrepancy between the measured and actual wavefronts inside these large-scale structures suggests that the pressure variations are not small inside these structures. It has been shown that the pressure fluctuations in shear layers with well-defined vortical structures significantly contribute to the overall aero-optical distortions (Fitzgerald and Jumper, 2004). So it is plausible to assume that a packet of vortical structures in the boundary layer might have an associated lower pressure region inside, leading to the observed discrepancy between the SRA and measured OPD .

As wavefronts are integrals of the density field, analysis of the spanwise extent of the local minima provides non-intrusive optical measurements of the instantaneous spanwise size of

the large-scale structures. For instance, from Figure 5.13, a typical spanwise extent is found to be approximately $0.5d$ with a typical streamwise extent of $\sim 1\delta$. Again, these observations of predominantly streamwise-elongated large-scale structures are consistent with findings in the literature (e.g. Hutchins et al, 2005).

5.8.2 Local *OPD*-Maxima.

A similar analysis was performed to find a flow structure that corresponds to the local *OPD*-maximum. Several examples of velocity fields with related *OPDs* are shown in Figure 5.14. The velocity field vectors are plotted the same way, as in Figure 5.13, but this time a false-color map shows the v -fluctuations. It was observed that the most local *OPD* maxima are related to compact regions of large positive v -fluctuations, residing mostly in the outer portion of the boundary layer. One plausible explanation of why these ejection-like, positive vertical-velocity regions corresponds to the local *OPD* maximum is that these vertical velocities will increase the local turbulent thickness of the boundary layer and form a “bulge” in the boundary layer interface; consequently, the upper limit of integration in equation (1.1) and therefore the *OPD*-value would increase. As no obvious large-scale vortical structure was observed in these representative velocity fields, local *OPD*-maxima are most probably related to the local increase of the boundary layer thickness.

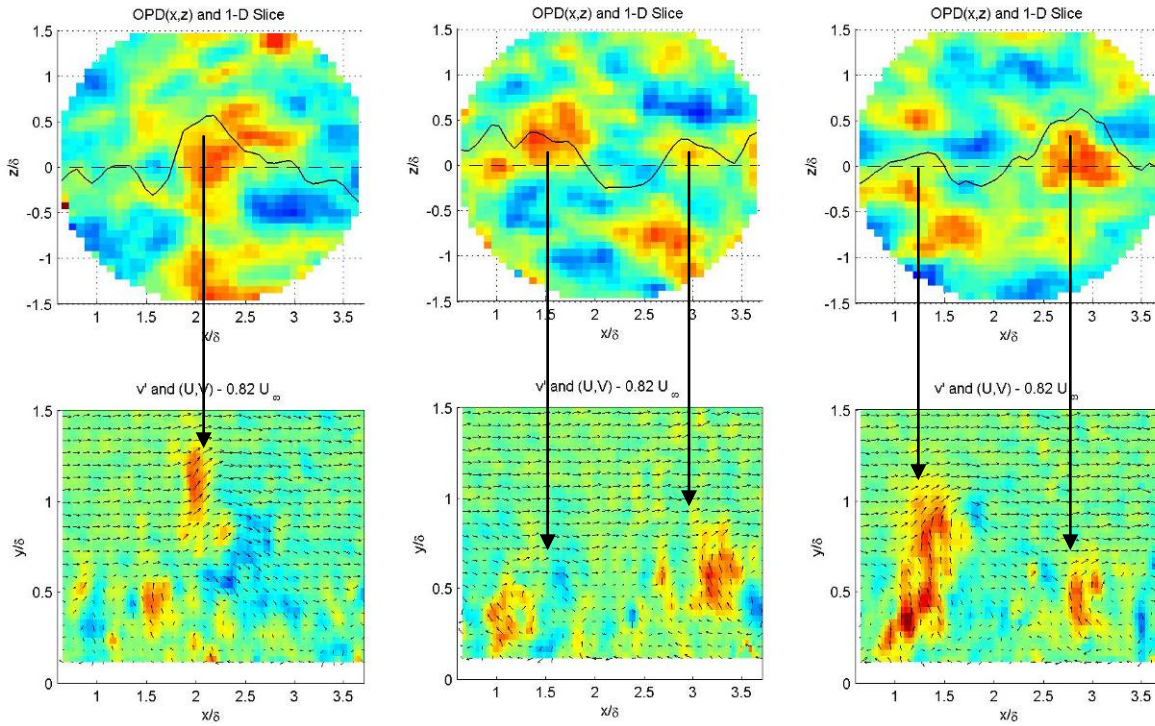


Figure 5.14. Top: Representative wavefronts with *local maxima* near the PIV centerline (dashed line). Measured 2-D *OPD* are given by false color map, blue are negative values and red are positive values, and the measured 1-D *OPD*($x,0$) slices are shown as black lines. Bottom: the corresponding velocity fields. Velocity vectors are the instantaneous U -velocity with $0.82U_\infty$ subtracted, superimposed with the instantaneous fluctuating v -field (false color map, blue are negative values and red are positive values).

Again, assuming that the streamwise and the spanwise size of the wavefronts at the local maxima are related to the size of these vertical-velocity regions, wavefronts in Figure 6 suggest that these interface “bulges” are approximately 0.7δ in both streamwise and spanwise directions.

Finally, instances where the measured and the actual wavefronts agree were investigated (not shown). For these instances, the instantaneous SRA appears to be valid (pressure/total fluctuations are small) and no significant vortical activity in the boundary layer was observed.

5.9 Conclusions: Notre Dame

A complimentary experimental technique, which uses simultaneous velocity-wavefront measurements, is proposed. Since wavefronts are proportional to the integrated density field, it was shown that the comparison between the velocity field and the wavefront provide additional information about the large-scale structures inside the boundary layer. Plausible relations between different structures in the boundary layer and the corresponding wavefronts were presented and discussed. The SRA was used to investigate the relationship between optical distortion and the velocity field, comparing the *OPD* implied by the velocity field with the one-dimensional *OPD* from the Shack-Hartmann sensor at the location of the PIV plane. 2-D wavefronts were shown to provide additional information about the streamwise/spanwise statistics of the large-scale BL structures. By comparing actual wavefronts with the estimated ones, using the Strong Reynolds Analogy, the effect of the local pressure field and the underlying vortical structure can be estimated and studied.

References

- Adrian, R.J. (2007) Hairpin vortex organization in wall turbulence. *Phys. Fluids*, **19**(4), pp. 1-16.
- Adrian, R.J. Meinhart, C.D. and Tomkins, C.D. (2000) Vortex organization in the outer region of the turbulent boundary layer. *Journal of Fluid Mechanics*, **422**, pp.1-54.
- Anders, J. (1985). Airfoil Large Eddy Breakup Devices for Turbulent Drag Reduction. In *S. Stack, Langley Symposium on Aerodynamics*, Volume 1 (pp. 573-858). Hampton, VA: NASA.
- Anders, J. B. (1990) Outer-Layer Manipulators for Turbulent Drag Reduction. In *D. M. Bushnell, & J. N. Hefner (Eds.), Viscous Drag Reduction in Boundary Layers* (pp. 263-284). Washington, DC: AIAA.
- Antonia, R. A., & Luxton, R. E. (1971) The response of a turbulent boundary layer to a step change in surface roughness. Part 1. Smooth to rough. *Journal of Fluid Mechanics*, **48**(4), 721-761.
- Antonia, R.A. Abe, H. and Kawamura, H. (1977) Response of a turbulent boundary layer to a step change in surface heat flux. *Journal of Fluid Mechanics*, **80**(1), pp.153-177.
- Cebeci, T. and Smith, A.M.O., (1974) *Analysis of Turbulent Boundary Layers*, Academic Press.
- Corke, T. (1981). A new View on Origin, Role, and Manipulation of Large Scales in Turbulent Boundary Layers. Chicago, IL: Ph.D. Thesis, Illinois Inst. of Technology.
- Corke, T. C., Guezennec, Y. G., & Nagib, H. M. (1979). Modification in drag of turbulent boundary layers resulting from manipulation of large-scale structures. In *Proc. Viscous Drag Reduction Symp.* (pp. 128-143). Dallas, TX: AIAA Prog. Astro. Aero. 72.
- Cress, J., Gordeyev, S. and Jumper, E. (2010) Aero-Optical Measurements in a Heated, Subsonic, Turbulent Boundary Layer. AIAA Paper No. 2010-0434.
- Cress, J. (2010). *Optical Distortions Caused by Coherent Structures in a Compressible, Turbulent Boundary Layer*. Notre Dame, IN: University of Notre Dame.
- Debiève, J. (1983) Etude d'une interaction turbulence onde de choc," PhD thesis, Thèse Université d'Aix Marseille II .
- Debieve, J.-F., Dupont, P., Smith, D., & Smits, A. (1997). Supersonic Turbulent Boundary Layer Subjected to Step Changes in Wall Temperature. *AIAA Journal*, **35** (1), 51-57.
- DeGraaff, D.B. & Eaton J.K. (2000) Reynolds-number scaling of the flat-plate turbulent boundary layer. *Journal of Fluid Mechanics*, **422**:319-346.
- Duan, L., Beekman, I. and Martin, M.P. (2010) Direct Numerical Simulation of Hypersonic Turbulent Boundary Layers. Part 2. Effect of Wall Temperature. *Journal of Fluid Mechanics*, **655**, 419-445.
- Duan, L. and Choudhari, M.M. (2013) Numerical Study of Pressure Fluctuations due to a Mach 6 Turbulent Boundary Layer. AIAA Paper No. 2013-0532.
- Elsinga, G.E., Scarano, F., Wieneke, B. and Van Oudheusden, BW. (2006) Tomographic particle image velocimetry *Exp. in Fluids*, **41**(6), 933-947.
- Fahringer, T., Thurow, B. (2012) Tomographic Reconstruction of a 3-D Flow Field Using a Plenoptic Camera. AIAA Paper 2012-2826.
- Fitzgerald, E.J. & Jumper, E.J. (2004) The optical distortion mechanism in a nearly incompressible free shear layer. *J. Fluid Mech*, **512**, 153–89.

- Fowles, G. (1975). *Introduction to Modern Optics, 2nd Ed.* New York: Dover Publications, Inc.
- Gao, Q., Yi, S., Jiang, Z., He, L. and Wang, X. (2013) Structure of the refractive index distribution of the supersonic turbulent boundary layer. *Optics and Lasers in Engineering* **51**, 1113-1119.
- Gatski, T. B., & Erlebacher, G. (2002) Numerical simulation of a spatially evolving supersonic turbulent boundary layer. *NASA Tech Memo. 2002-211934*.
- Gaviglio, J. (1987) Reynolds analogies and experimental study of heat transfer in the supersonic boundary layer, *Int. J. Heat Mass Transfer* **30**(5), 911-926.
- Gilbert, K. (2013). Challenges of high-brightness laser systems: a photon odyssey. *Optical Engineering*, **52** (7), 071412.
- Gilbert, K. G. (1982) KC-135 aero-optical boundary-layer/shear-layer experiments. In K. G. Gilbert, & L. J. Otten (Eds.), *Aero-Optical Phenomena (Progress in Astronautics and Aeronautics ed., Vol. 80, pp. 306-324)*. American Institute of Aeronautics and Astronautics.
- Gilbert, K. G., & Otten, L. J. (1982) *Aero-Optical Phenomena, Progress in astronautics and aeronautics series (Vol. 80)*. New York: American Institute of Aeronautics and Astronautics.
- Gladstone, J. H., & Dale, T. P. (1863). Researches on the Refraction, Dispersion, and Sensitiveness of Liquids. *Philosophical Transactions of the Royal Society of London*, **153**, 317-343.
- Gordeyev, S., & Jumper, E. J. (2010) Fluid Dynamics and Aero-Optics of Turrets. *Progress in Aerospace Sciences*, **46**, 388-400.
- Gordeyev, S., Cress, J. A., & Jumper, E. J. (2013) Far-Field Laser Intensity Drop-Outs Caused by Turbulent Boundary Layers. *Journal of Directed Energy*, **5** (1), 58-75.
- Gordeyev, S., Cress, J. A., Smith, A. E., & Jumper, E. J. (2015) Aero-Optical Measurements in a Subsonic, Turbulent Boundary Layer with Non-Adiabatic Walls. *Physics of Fluids*, **27**, 045110, 2015.
- Gordeyev, S., Jumper, E. J., & Hayden, T. (2012) Aero-Optics of Supersonic Boundary Layers. *AIAA Journal*, **50** (3), 682-690.
- Gordeyev, S., Smith, A. E., Cress, J. A., & Jumper, E. J. (2014) Experimental studies of aero-optical properties of subsonic turbulent boundary layers. *Journal of Fluid Mechanics*, **740**, 214-253.
- Gran, R. L., Lewis, J. E., & Kubota, T. (1974) The effect of wall cooling on a compressible turbulent boundary layer. *Journal of Fluid Mechanics*, **66** (3), 507-528.
- Guarini, S.E, Moser, R.D, Shariff, K and Wray, A. (2000) Direct Numerical simulations of a supersonic turbulent boundary layer at Mach 2.5. *Journal of Fluid Mechanics*, **414**, 1-33.
- Hefner, J. N., Weinstein, L. M., & Bushnell, D. M. (1979) Large-Eddy Break-Up Scheme for Turbulent Viscous Drag Reduction. In *Proc. Viscous Drag Reduction Symp.* (pp. 110-127). Dallas, Tx: AIAA Prog. Astro. Aero. 72.
- Hugo, R.J. and Jumper, E.J. (2000) Applicability of the Aero-Optic Linking Equation to a Highly Coherent, Transitional Shear Layer. *Applied Optics* **39**(24), 4392-4401.

- Hutchins, N., Hambleton, W.T. & Marusic I. (2005) Inclined Cross-Stream Stereo Particle Image Velocimetry Measurements in Turbulent Boundary Layers. *J. Fluid Mech.*, **541**, pp.21-34.
- Jumper, E. (1980) Aero-Optics Overview. Kirtland AFB, New Mexico: Proceedings of the Aero-Optics Workshop, Air Force Weapons Laboratory.
- Jumper, E. J., & Fitzgerald, E. J. (2001) Recent Advances in Aero-Optics. *Progress in Aerospace Sciences*, **37**, 299-339.
- Lemay, J. D., & Bonnet, J. (1990) Turbulent kinetic energy balance in a LEBU modified turbulent boundary layer. *Experiments in Fluids*, **9** (6), 301-308.
- Liepmann, H. W. (1952) Deflection and diffusion of a light ray passing through a boundary layer (Report SM-14397). Santa Monica, CA: Douglas Aircraft Company, Santa Monica Division.
- Liu, K. and Pletcher, R.H. (2007) Compressibility and Variable Density Effects in Turbulent Boundary Layers. *J of Heat Transfer*, **129**, 441-448.
- Marusic, I., McKeon, B. J., Monkewitz, P. A., Nagib, H. M., Smits, A. J. & Sreenivasan, K. R. (2000) Wall-bounded turbulent flows: recent advances and key issues. *Phys Fluids*, **22**, 65103.
- Moser, R. D., Rogers, M. M., & Ewing, D. W. (1998) Self-similarity of time-evolving plane wakes. *Journal of Fluid Mechanics*, **367**, 255-289.
- Morkovin, M.V. (1962) Effects of compressibility on turbulent flows. In *Mechanique de la Turbulence*, edited By A. Favre, (CNRS, Paris, France), pp. 367-380.
- Nagib, H. M., Chauhan, K. A., & Monkewitz, P. A. (2007) Approach to an asymptotic state for zero pressure gradient turbulent boundary layers. *Phil. Trans. R. Soc. A*, **365**, 755-770.
- Porter, C., Gordeyev, S. and Jumper, E. (2013) Large-Aperture Approximation for Not-So-Large Apertures, *Journal of Optical Engineering* **52**(7), 071417.
- Pirozzoli, S., Grasso, F., & Gatski, T. B. (2004) Direct numerical simulation and analysis of a spatially evolving supersonic turbulent boundary layer at $M=2.25$. *Physics of Fluids*, **16** (3), 530-545.
- Plesniak, M. (1984) *Optimized Manipulation of Turbulent Boundary Layers Aimed at Net Drag Reductions*. Chicago, IL: M.S. Thesis, Illinois Institute of Technology.
- Rose, W. C. (1979) Measurements of aerodynamic parameters affecting optical performance. *Final Report AFWL-TR-78-191*, Air Force Weapons Laboratory, Kirtland AFB, NM.
- Rose, W. C., & Johnson, E. A. (1982) Unsteady density and velocity measurements in the 6 x 6 ft wind tunnel. In K. G. Gilbert, & L. J. Otten (Eds.), *Aero-Optical Phenomena* (Progress in Astronautics and Aeronautics ed., Vol. 80, pp. 218-232). American Institute of Aeronautics and Astronautics.
- Ross, T. (2009) Limitations and applicability of the Marechal approximation. *Applied Optics*, **48** (10), 1812-1818.
- Rought, R. (2013) *Identification of thermally-tagged coherent structures in the zero pressure gradient turbulent boundary layer*. Engineering Thesis, Caltech.
- Savill, A. M., & Mumford, J. C. (1988) Manipulation of turbulent boundary layers by outer-layer devices; skin-friction and flow-visualization results. *Journal of Fluid Mechanics*, **191**, 389-418.

- Serati, S., & Stockley, J. (2003) Phased array of phased arrays for free space optical communications. IEEEAC Paper 1085 in *IEEE Aerospace Conference Proceedings*, (pp. 1085-1092).
- Smith, A. E., Gordeyev, S., & Jumper, E. J. (2012) Aperture effects on Aero-Optical distortions caused by subsonic boundary layers. AIAA-2012-2986.
- Smith, D.R. and Smits, A.J. (1993) Simultaneous Measurement of velocity and Temperature Fluctuations in the Boundary Layer of Supersonic Flow. *Experimental Thermal and Fluid Science* **7**, 221-229.
- Smits, A., & Dussauge, J. (1996) *Turbulent Shear Layers in Supersonic Flow* (Chapter 5 ed.). Woodbury, New York: American Institute of Physics.
- Smits, A. J., McKeon, B. J. and Marusic, I. (2011) High Reynolds number wall turbulence. *Annual Review of Fluid Mechanics*, **43**, 353-375.
- Spina, E.F., Smits, A.J., and Robinson, S.K. (1994) The Physics of Supersonic Turbulent Boundary Layers. *Annual Review of Fluid Mechanics* **26**, 87-319.
- Sutton, G. W. (1969) Effects of turbulent fluctuations in an optically active fluid medium. *AIAA Journal*, **7** (9), 1737-1743.
- Tatarski, V. I. (1971) The Effects of the Turbulent Atmosphere on Wave Propagation. Jerusalem: *Trans. for NOAA by Israel Program for Scientific Translations*.
- Tatarski, V. I. (1961) *Wave Propagation in a Turbulent Medium*. New York: McGraw-Hill.
- Walsh, M. J. (1990) Riblets. In D. M. Bushnell, & J. N. Heffner (Eds.), *Viscous Drag Reduction in Boundary Layers*. Washington, DC: AIAA .
- Walz, A. (1969) *Boundary Layers of Flow and Temperature*, MIT Press.
- Wang, K., & Wang, M. (2012) Aero-Optics of subsonic turbulent boundary layers. *Journal of Fluid Mechanics*, **696**, pp. 122-151.
- Wang, K. and Wang, M. (2013) On the accuracy of Malley probe measurements of aero-optical effects: a numerical investigation. *J. Opt. Eng.* **52**(7), 071407.
- Wang, M., Mani, A., and Gordeyev, S. (2012) “Physics and Computation of Aero-Optics”, *Annual Review of Fluid Mechanics*, Vol. **44**, pp. 299-321.
- White, M. D., & Visbal, M. R. (2011) Simulation of Aero-Optical interactions in Transonic Boundary Layers. AIAA-2011-3279.
- White, M.D., and Visbal, M.R. (2012) Aero-optics of compressible Boundary Layers in the Transonic Regime. AIAA Paper No. 2012-2984.
- Whiteley, M., & Gordeyev, S. (2013). Conformal phased array aero-optical modeling and compensation. *Optical Engineering*, **52** (7), 071409.
- Wyckham, C., & Smits, A. (2009) Aero-optic distortion in transonic and hypersonic turbulent boundary layers. *AIAA Journal* **47** (9), pp. 2158-2168.
- Yajnik, K., & Ancharya, M. (1977) Non-equilibrium Effects in a Turbulent Boundary Layer due to the Destruction of Large Eddies. National Aeronautical Lab., Bangalore, NAL-BL-7.
- Zaman, K., Hirt, S., & Bencic. (2012) Boundary Layer Flow Control by an Array of Ramp-Shaped Vortex Generators. Cleveland, Ohio: NASA/TM 2012-217437.

Appendix: List of Publications Based in Whole or in Part on Results from the Current Program

Journal Publications

1. S. Gordeyev, J.A. Cress, A Smith and E.J. Jumper, "Aero-optical measurements in a subsonic, turbulent boundary layer with non-adiabatic walls", *Physics of Fluids*, **27**, 045110, 2015.
2. S. Gordeyev, A. E. Smith, J.A. Cress and E.J. Jumper, "Experimental studies of aero-optical properties of subsonic turbulent boundary layers", *Journal of Fluid Mechanics*, **740**, pp. 214-253, 2014.

4 more manuscripts are currently been prepared to be submitted to Journal of Fluid Mechanics, Physics of Fluids, Experiments in Fluids and AIAA Journal.

Conference Papers

1. S. Gordeyev, A.E. Smith, T Saxton-Fox and B. McKeon, "Studies of the large-scale structure in adiabatic and moderately-wall-heated subsonic boundary layers," Paper 283, 9th International Symposium on Turbulence and Shear Flow Phenomena (TSFP-9), June 30 - July 3, 2015, The University of Melbourne, Australia.
2. A.E. Smith, S, Gordeyev, T. Saxton-Fox and B. McKeon, "Subsonic Boundary-Layer Wavefront Spectra for a Range of Reynolds Numbers," AIAA Paper 2014-2491, 2014.
3. A. Smith and S. Gordeyev, "Aero-Optical Mitigation of Turbulent Boundary Layers Using Large-Eddy Break-Up Devices," AIAA Paper 2014-0321, 2014.
4. A. Smith and S. Gordeyev, "The Effects of Wall Cooling on Aero-Optical Aberrations Caused by Subsonic Turbulent Boundary Layers," AIAA Paper 2013-3133, 2013.
5. A. Smith and S. Gordeyev, "Evaluation of Passive Boundary Layer Flow Control Methods for Aero-Optic Mitigation," AIAA Paper 2013-0718, 2013.

Appendix: List of the students supported on the grant

University of Notre Dame

1. Adam Smith, PhD student, title of PhD thesis: “Evaluation of Passive Boundary Layer Flow Control Techniques For Aero-Optic Mitigation”, graduation date: May 16, 2015.
2. Arman Mirhashemi, PhD student, title of PhD thesis is to be determined, expected year of graduation: 2017.
3. Matthew Kenmetz, PhD student, title of PhD thesis is to be determined, expected year of graduation: 2018.

California Institute of Technology

1. Rebecca Rought, Engineers Degree, thesis title: “Identification of thermally-tagged coherent structures in the zero pressure gradient turbulent boundary layer” (2013).
2. Theresa Saxton-Fox, PhD student, title of PhD thesis is to be determined, expected year of graduation: 2017.
3. Jonathan Morgan, PhD student, title of PhD thesis is to be determined, expected year of graduation: 2018.
4. Subrahmanyam Duvvuri, PhD student, title of PhD thesis is to be determined, expected year of graduation: 2016.
5. Ryan McMullen, M.S. student (2014).

1.

1. Report Type

Final Report

Primary Contact E-mail**Contact email if there is a problem with the report.**

sgordeye@nd.edu

Primary Contact Phone Number**Contact phone number if there is a problem with the report**

574-631-4338

Organization / Institution name

University of Notre Dame

Grant/Contract Title**The full title of the funded effort.**

Characterization, Manipulation and Control of The Turbulent Boundary Layer For Aero-Optical Applications

Grant/Contract Number**AFOSR assigned control number. It must begin with "FA9550" or "F49620" or "FA2386".**

FA9550-12-1-0060

Principal Investigator Name**The full name of the principal investigator on the grant or contract.**

Stanislav Gordeyev

Program Manager**The AFOSR Program Manager currently assigned to the award**

Dr. Douglas Smith

Reporting Period Start Date

03/15/2012

Reporting Period End Date

03/14/2015

Abstract

This report presents results of systematic experimental studies of various passive mitigation techniques to reduce aero-optical effects caused by turbulent boundary layers. Parametric studies of Large-Eddy Break-Up devices showed that aero-optical distortions can be suppressed by 45% for several boundary layer thicknesses. It was shown that moderate cooling of the wall also reduces aero-optical distortions by 60%. A model to predict effects of non-adiabatic walls, both full and partial, over a range of subsonic and supersonic Mach numbers was developed and shown to correctly predict experimentally-observed reductions. Heating the wall allows extending the use of wavefront sensors into low subsonic speeds. Using this technique, aero-optical effects of boundary layers at low (1,700-8,000) Reynolds numbers, were investigated. Simultaneous velocity-optical measurements revealed that large-scale vortical structures are mostly responsible for aero-optical distortions and also indicated that the pressure fluctuations inside these vortical structures might be significant.

Distribution Statement**This is block 12 on the SF298 form.**

Distribution A - Approved for Public Release

Explanation for Distribution Statement

If this is not approved for public release, please provide a short explanation. E.g., contains proprietary information.

SF298 Form

Please attach your [SF298](#) form. A blank SF298 can be found [here](#). Please do not password protect or secure the PDF
The maximum file size for an SF298 is 50MB.

[SF298.pdf](#)

Upload the Report Document. File must be a PDF. Please do not password protect or secure the PDF . The maximum file size for the Report Document is 50MB.

[Final Report AFSOR Gordeyev.pdf](#)

Upload a Report Document, if any. The maximum file size for the Report Document is 50MB.

Archival Publications (published) during reporting period:

Journal Publications

1. S. Gordeyev, J.A. Cress, A Smith and E.J. Jumper, "Aero-optical measurements in a subsonic, turbulent boundary layer with non-adiabatic walls", Physics of Fluids, 27, 045110, 2015.
2. S. Gordeyev, A. E. Smith, J.A. Cress and E.J. Jumper, "Experimental studies of aero-optical properties of subsonic turbulent boundary layers", Journal of Fluid Mechanics, 740, pp. 214-253, 2014.

Conference Papers

1. S. Gordeyev, A.E. Smith, T Saxton-Fox and B. McKeon, "Studies of the large-scale structure in adiabatic and moderately-wall-heated subsonic boundary layers," Paper 283, 9th International Symposium on Turbulence and Shear Flow Phenomena (TSFP-9), June 30 - July 3, 2015, The University of Melbourne, Australia.
2. A.E. Smith, S. Gordeyev, T. Saxton-Fox and B. McKeon, "Subsonic Boundary-Layer Wavefront Spectra for a Range of Reynolds Numbers," AIAA Paper 2014-2491, 2014.
3. A. Smith and S. Gordeyev, "Aero-Optical Mitigation of Turbulent Boundary Layers Using Large-Eddy Break-Up Devices," AIAA Paper 2014-0321, 2014.
4. A. Smith and S. Gordeyev, "The Effects of Wall Cooling on Aero-Optical Aberrations Caused by Subsonic Turbulent Boundary Layers," AIAA Paper 2013-3133, 2013.
5. A. Smith and S. Gordeyev, "Evaluation of Passive Boundary Layer Flow Control Methods for Aero-Optic Mitigation," AIAA Paper 2013-0718, 2013.

Changes in research objectives (if any):

Change in AFOSR Program Manager, if any:

Extensions granted or milestones slipped, if any:

AFOSR LRIR Number

LRIR Title

Reporting Period

Laboratory Task Manager

Program Officer

Research Objectives

Technical Summary

Funding Summary by Cost Category (by FY, \$K)

	Starting FY	FY+1	FY+2
Salary			
Equipment/Facilities			
Supplies			
Total			

Report Document

Report Document - Text Analysis

Report Document - Text Analysis

Appendix Documents

2. Thank You

E-mail user

Jun 12, 2015 15:43:58 Success: Email Sent to: sgordeye@nd.edu